ABSTRACT

Title of Dissertation: COMPREHENSIVE STUDY AND FUNDAMENTAL UNDERSTANDING OF LITHIUM SULFUR BATTERIES FOR EVTOL

Emily Fisler
Doctor of Philosophy, 2022

Dissertation Directed by: Professor Anubhav Datta
Department of Aerospace Engineering

This dissertation is an attempt to bridge the traditional isolation of electrochemistry and aeronautics, particularly rotary-wing aeronautics, where integration of power and platform is vital for the development of a viable aircraft. The dissertation topic addresses the principal barriers of electric-VTOL aircraft: energy and power. It explores a promising alternative to traditional lithium-ion technology; advanced lithium sulfur batteries are projected to supply double the energy of lithium-ion. The principal conclusions are: 1. lithium sulfur can indeed achieve double the energy of lithium-ion but only at low power settings, 2. lithium sulfur exhibits high internal resistance compared to lithium-ion which explains the loss of energy at high power, and 3. discharging lithium sulfur only halfway stabilizes the batteries.

A conceptual sizing analysis was developed and verified with NASA. Key battery performance targets were determined for electric VTOL aircraft. Lithium sulfur and lithium-ion coin cells were fabricated with identical overhead for a clear and consistent comparison of specific energy and power. The characteristics measured were discharge cycles, cycle life, impedance under conditions unique to electric vertical takeoff and landing aircraft namely high C-Rates, half cycles, and high transients. Equivalent circuit models were developed and validated to predict the steady-state and transient behavior of these cells. Results show that lithium sulfur provides

more than twice the specific energy of lithium-ion up to currents of almost C/2. At 1C, it is comparable. Above 1C it drops drastically and by 4C the energy vanishes almost entirely. This is traced to an order of magnitude higher impedance of these cells. The price to pay for high energy is low cycle life. However, it appears this problem can be eliminated by half cycles. The dynamic behavior of lithium sulfur is richer in comparison to lithium-ion. The response is still capacitative, hence first order, but the complex Warburg and constant phase elements have far greater influence. The behavior is harder to model as it does not fit neatly into linear equivalent circuits. The key conclusion is that lithium sulfur appears to be an attractive alternative to lithium-ion with characteristics that have significant ramifications on future electric VTOL aircraft design and infrastructure.

COMPREHENSIVE STUDY AND FUNDAMENTAL UNDERSTANDING OF LITHIUM SULFUR BATTERIES FOR EVTOL

by

Emily Fisler

Dissertation submitted to the Faculty of the Graduate School of the
University of Maryland, College Park in partial fulfillment
of the requirements for the degree of
Doctor of Philosophy
2022

Advisory Committee:
Professor Anubhav Datta, Chair and Advisor
Professor James Baeder
Professor Inderjit Chopra
Professor Alison Flautau
Professor Chungseng Wang

To my family for their unending support and encouragement

Acknowledgments

Completing this dissertation would not have been possible without the support of various people. First I would like to thank my advisor Dr. Anubhav Datta for all of his guidance, advice, and support during my PhD career. My transition from chemical engineering to aerospace engineering was daunting, and Dr. Datta was able to smooth this transition and helped me become a true aerospace engineer. His dedication to his students is unparalleled. I would also like to thank the other members of my committee, Dr. Inderjit Chopra, Dr. James Baeder, Dr. Alison Flatau, and Dr. Chungseng Wang, for their contributions and feedback.

This work was made possible with the Army/Navy/NASA Vertical Lift Research Center of Excellence funding. Technical guidance and feedback from Dr. Mahendra Bhagwat and Dr. William Lewis were especially appreciated.

Developing a new battery lab in an aerospace engineering department took time and was a group effort. The experimental portion of this work would not have been possible without the collaboration with the US Army Research Lab Adelphi. Many thanks to Dr. Jeffrey Read and Dr. Shengshui Zhang for the technical advice, laboratory access, and troubleshooting assistance.

I'd like to acknowledge the other graduate students in Dr. Datta's lab. They fostered a welcoming, friendly, collaborative environment, and I am always impressed by their creativity and intellect. To Ravi, James, Seyhan, Shashank, Abhishek, and Mrinal - it has been a pleasure going through the PhD program with you, and to me we will always be the First Years.

I'd like to say thank you to one person in particular. Katie, you were always there to support me, listen to my troubles, celebrate my achievements, and encourage me when I most needed it.

Thank you for your companionship, and you'll always be part of my family.

My mom, dad, and sister have been with me every step of this journey. I cannot fully express the effect their support and encouragement has had on me. When I faltered, they were there to help me, and I wouldn't have made it through graduate school without them. Thank you for being there for me and supporting me in every way possible.

Table of Contents

List of Tables

List of Figures

List of Abbreviations

AFDD	Army Aeroflightdynamics Directorate
AHS	American Helicopter Society (re-named as VFS)
AIAA	American Institute of Aeronautics and Astronautics
ARL	Army Research Lab
CPE	Constant Phase Element
DL	Disk Loading
DOD	Depth of Discharge
DOL	Dioxolane
DME	Dimethoxyethane
EC	Ethylene Carbonate
ECM	Equivalent Circuit Model
EIS	Electrochemical Impedance Spectroscopy
EMC	Ethyl Methyl Carbonate
EOF	End of Flight
eVTOL	Electric Vertical Take-Off and Landing
FM	Figure of Merit
GTOW	Gross takeoff weight
L/D	Lift to Drag ratio
LCO	Lithium Cobalt Oxide, $LiCoO_2$
LFP	Lithium Iron Phosphate, $LiFePO_4$
LMO	Lithium Manganese Oxide, $LiMO_2$
Li-ion	Lithium-ion
$LiNO_3$	Lithium Nitrate
$LiPF_6$	Lithium Hexafluorophosphate
Li-S	Lithium Sulfur
$LiSO_2$	Lithium Sulfur Dioxide
M	Molar
n-mile	Nautical mile
NASA	National Aeronautics and Space Administration
NCA	Lithium Nickel Cobalt Aluminum Oxide
NMC	Lithium Nickel Manganese Cobalt Oxide, $LiNiMnCoO_2$
PAN	Polyacrylonitrile
PANS	Polyacrylonitrile-Sulfur
PS	Polysulfide

R-C	Resistor-Capacitor
RPM	Revolutions per Minute
SE	Specific Energy
SEI	Solid Electrolyte Interface
SFC	Specific Fuel Consumption
SOC	State of Charge
SOE	State of Energy
SQ	Specific Charge
UMD	University of Maryland
VFS	Vertical Flight Society (previously AHS)
VTOL	Vertical Take-Off and Landing

Chapter 1: Introduction

This dissertation is an attempt to bridge the traditional isolation of electrochemistry and aeronautics, particularly rotary-wing aeronautics, where integration of power and platform is vital for the development of a viable aircraft. This dissertation addresses the major barriers of electric Vertical Take Off and Landing (VTOL) aircraft: energy and power. It explores a promising alternative to traditional Lithium-ion (Li-ion) technology, as advanced Lithium Sulfur (Li-S) batteries are projected to supply double the energy of Li-ion. The principal conclusions are: 1. Li-S can indeed achieve double the energy of Li-ion but only at low power settings, 2. Li-S exhibits high internal resistance compared to Li-ion which results in the loss of energy at high power, and 3. discharging Li-S only halfway stabilizes the batteries.

Findings presented in this dissertation show that Li-S can be a promising and feasible alternative to Li-ion at a basic electrochemical level with the potential to double the range and payload of electric VTOL aircraft. The realization of that potential will require careful scale-up with thermal, mechanical, and electrical considerations and use in conjunction with high power alternatives for hover and maneuvers.

Since the first electric manned coaxial helicopter flight of Pascal Chretien in August 2011 [1] and the first electric multirotor helicopter flight of e-VOLO in October 2011 [2] there has been an explosion of interest in the development of such aircraft. They are inspired by the desire

for clean and quiet vertical flight, enabled by light-weight batteries and motors as replacements for polluting and loud combustion engines, and driven by the growth of digital design and manufacturing, access to cheap consumer electronics, and maturation of drone technologies such as autonomy and mobile computing.

The American Helicopter Society (AHS), which in 2018 was re-named the Vertical Flight Society (VFS), has called these aircraft by various names — Electric-VTOL, electric-VTOL, or in short just eVTOL. The short nomenclature has stuck and we use that term throughout this thesis. Formally, per [3] we define eVTOL as a VTOL aircraft that is propelled by electric power and capable of carrying people. Note that eVTOL need not be battery powered, as fuel cell electric or engine-hybrid electric also fall within this category as long as the drive is electric. The focus of this dissertation is on battery powered eVTOL.

Passenger aircraft are more complex than small drones and require more than a clever combination of scaled-up components from consumer electronics or electric automobiles. Maturation of eVTOL into a safe, sensible, and commercially viable aircraft requires a clear understanding of rotary-wing fundamentals, the unique barriers they pose, and ultimately their timely resolution. The objective of this dissertation is to address the most pressing of these barriers: insufficient specific energy and power.

This introductory chapter begins with specific energy and power, then covers motivation, background, introduction to the batteries that are the subject of this dissertation, and ends with specific objectives and outline of the thesis.

1.1 Specific Energy and Power

Specific energy and power are the energy and power normalized by the weight of the fuel and the power-plant respectively.

In aviation, the specific energy is characterized indirectly by the Specific Fuel Consumption (SFC). The SFC is defined as the fuel flow per power in units of kg/kWh. Thus, it is equivalent to specific energy inverted. This inverted metric is used with the kilo dropped in favor of just Wh/kg. This is the familiar metric for electrochemists and battery engineers.

The definition of specific power with electrical power and battery weight alone allows a direct connection to the C-Rate. C-Rate is a familiar metric for electrochemists and battery engineers.

1.2 C-Rate

C-Rate can be calculated using Eq. (1.1) and has units of hr^{-1}. C-Rate is a measure of the current at which a battery is discharged relative to its maximum capacity. A C-Rate of x hr^{-1} is also written as xC. A C-Rate of 1C means that the battery will fully discharge in 1 hour, 2C means it will fully discharge in 0.5 hrs, C/20 means it will fully discharge in 20 hrs, and so on.

$$\text{C-Rate} = \frac{\text{Power}}{\text{Energy}} = \frac{1}{\text{Time}} \tag{1.1}$$

High C-Rate is analogous with high current and therefore high power. A fully charged, 1 Ah battery with a C-Rate of 1C should provide 1 Ampere (A) for one hour. The same battery discharging at C/2 should provide 500 mA for two hours, and at 2C it should supply 2 A for

30 minutes. However, this is not the case. Internal losses due to battery internal resistances and heat loss at high C-Rates shorten the discharge time. This also decreases the energy supplied as energy is dependent on the time of discharge.

1.3 Motivation

Hybrid-electric and all-electric vertical takeoff and landing aircraft are being researched by various organizations. There are over 600 eVTOL concepts in the Vertical Flight Society's (VFS) World eVTOL directory, with over 160 eVTOL aircraft having been tested in flight or a wind tunnel [4]. Most, if not all eVTOL aircraft rely on Li-ion chemistries for batteries. A commercially viable aircraft has not yet been realized, although some are in an advanced phase of flight testing. Key barriers to practical aircraft include poor range, endurance, and payload, all of which stem from a lack of sufficient specific power and energy. Powerful batteries can extend the range for eVTOL in both civilian and military applications, and secure them as part of commercially viable on-demand aircraft.

Studies on eVTOL aircraft have shown the urgent need for a high-power and high-energy battery. In 2014, Datta and Johnson [5] stated that for practical all-electric manned VTOL flight, the battery technology level should reach a specific energy of 200-300 Wh/kg pack level (usable on-board) by the year 2020 and 500 Wh/kg by 2030 with C-Rate capabilities up to 5C. Today, even 300 Wh/kg at a rate of 1C remains hard to achieve. Johnson *et al.* [6] states,

"*The most important factor in the feasibility of electrical propulsion systems is the requirement for light-weight, high-power batteries.*"

There is a large step from electrochemical energy and power to pack level energy and power

that is available and installed. Recent battery system fabrication has shown from cell to pack a reduction factor of 1.6 is the best state-of-the-art [7]. The packing factor stems from cooling systems, fusing, battery management systems, and other electrical and mechanical overhead. It is clear that higher specific energy cells are needed to avoid such impractical packing factors. For example, a battery with a pack level, usable on-board specific energy of 300 Wh/kg would currently decrease by a factor of 1.6 to a usable specific energy of 188 Wh/kg. To have an available, usable on-board specific energy of 300 Wh/kg, a battery of 480 Wh/kg is needed. This is far beyond current Li-ion capabilities.

This packing factor is measured relative to cells of around 1 Ah charge capacity, not laboratory research cells that are typically tiny with 1-2 mAh charge capacity. These tiny cells suffer from worse overhead by the nature of construction. For these tiny cells it is more appropriate to measure specific energy and power using electrode mass alone and then apply a factor of around 2 to assess the corresponding values that might be achieved for a scaled up 1 Ah cell. For example, for the 480 Wh/kg cell discussed above, the electrochemistry at the coin cell level should indicate a specific energy of 960 Wh/kg. Only then a 300 Wh/kg battery might be aspired to at the pack level.

Li-S batteries are an emerging technology with the potential to surpass the performance of current Li-ion batteries. The high theoretical charge capacity of sulfur leads to a high projected specific energy, making Li-S a promising alternative to conventional Li-ion technology. The high projected specific energy of Li-S batteries makes them desirable for light-weight applications, specifically eVTOL. However, a consistent comparison is hard to find between Li-S and Li-ion chemistries with identical overhead weight. This is an essential and immediate need for reliable technology forecast.

1.4 eVTOL Background

eVTOL aircraft are an emerging technology with the promise of electric passenger flights. Pre-existing companies such as Airbus, Boeing, and Bell started working on eVTOL technology, and new companies such as Joby Aviation and Lilium emerged to create their own vision of an eVTOL aircraft.

In 2018, Johnson *et al.* [6] presented three conceptual eVTOL aircraft designs for various ranges and number of passengers. The research areas for eVTOL were focused for future research guidance. Later the same year, Johnson *et al.* [8] developed a specific mission and determined performance targets for the three conceptual eVTOL aircraft. The work also compared aircraft characteristics when using conventional turboshaft propulsion versus electric propulsion. Also in 2018, Ng and Datta [3] developed steady state and transient models of fuel cells and batteries and validated the models experimentally. Weight models needed for eVTOL sizing were also presented.

In 2020, Bills *et al.* [9] demonstrated the development of a battery performance and degradation model specifically for electric aircraft operations. Yang *et al.* [10] published in 2021 on the challenges and key requirements of batteries for eVTOL. Findings included the importance of fast charging to downsize aircraft and batteries.

The ongoing research of eVTOL aircraft design and performance has advanced the field and allowed for the realization of physical aircraft that have been flown. There is still much to be done, and battery technology remains a key barrier to eVTOL operations.

1.5 Lithium-ion Background

From mobile phones to electric vehicles, Li-ion batteries are widely used for rechargeable energy storage. Goodenough is credited with the initial development of Li-ion batteries with his 1980 paper on a novel cathode material [11]. This finding was crucial for achieving modern rechargeable Li-ion batteries. A simple diagram of a Li-ion cell can be seen in Figure 1.1. The cell consists of a positive electrode, a negative electrode, and an electrolyte. In this case, graphite is the negative electrode and Lithium Cobalt Oxide ($LiCoO_2$, LCO) is the positive electrode. These electrodes are the anode and cathode of the cell. The anode is defined as the electrode that is oxidized (loses electrons), and the cathode is defined as the electrode that is reduced (gains electrons). Based on these definitions, the anode and cathode are different when charging versus discharging the cell.

When charging or discharging a Li-ion cell, the lithium ions undergo an intercalation reaction with the graphite. Intercalation is a reversible reaction and is when an ionic, atomic, or molecular element is inserted into empty spaces in a host lattice structure [12]. For Li-ion batteries, the graphite acts as the host structure, and the lithium ions are inserted into the graphite lattice.

Consider the Li-ion cell with an LCO positive electrode in Figure 1.1. A newly built Li-ion cell begins in the discharged state, so the cell must begin with charging. During charging, the lithium ions move from the positive electrode to the negative electrode as seen in Figure 1.2a. The reactions at the cathode and anode, as well as the overall reaction of the cell, are as seen in Eq. 1.2.

LCO is a unique cathode in that it is capable of charging up to 4.4 V. However, operation

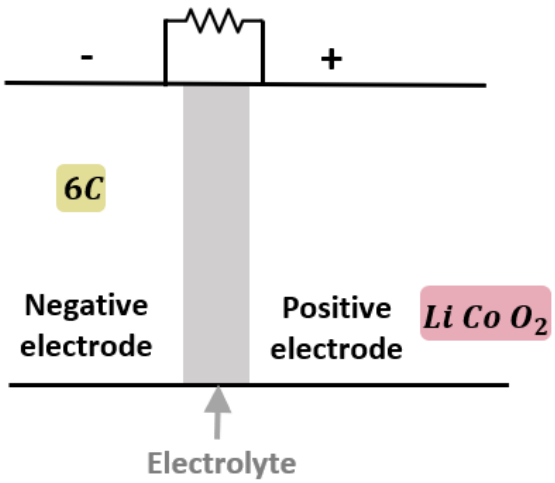

Figure 1.1: Simple diagram of Li-ion cell, electrodes are graphite (6C) and LCO.

above 4.2 V changes the cathode material structure and decreases the stability and performance [13]. So, charging must stop at 4.2 V. This means that only about half of the lithium in LCO is extracted and used in the cell reactions. This is represented in Eqs. 1.2 and 1.3 by the factor x. The maximum value of x is typically 0.5. So, one mole of LCO and one mole of graphite produces half a mole of electrons.

When discharging, the lithium ion moves from the negative electrode to the positive electrode as seen in Figure 1.2b. The reactions at the anode and cathode, and the overall cell reaction, are as seen in Eq. 1.3.

Charging:

$$\begin{aligned} \text{Cathode:} \quad & 6C + xLi^+ + xe^- \rightarrow C_6Li_x \\ \text{Anode:} \quad & LiCoO_2 \rightarrow Li_{1-x}CoO_2 + xLi^+ + xe^- \\ \text{Overall:} \quad & 6C + LiCoO_2 \rightarrow C_6Li_x + Li_{1-x}CoO_2 \end{aligned} \tag{1.2}$$

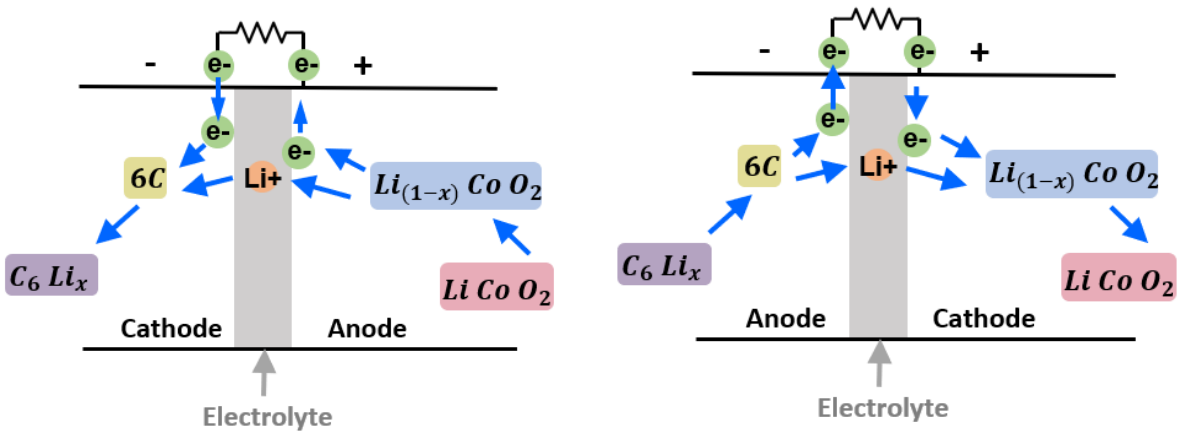

(a) Charging.

(b) Discharging.

Figure 1.2: Charge and discharge reactions in a Li-ion cell with graphite and LCO electrodes.

Discharging:

$$\begin{aligned} \text{Anode:} \quad & C_6Li && \rightarrow \quad 6C + xLi^+ + xe^- \\ \text{Cathode:} \quad & Li_{1-x}CoO_2 + xLi^+ + xe^- && \rightarrow \quad LiCoO_2 \\ \text{Overall:} \quad & C_6Li + Li_{1-x}CoO_2 && \rightarrow \quad 6C + LiCoO_2 \end{aligned} \tag{1.3}$$

Conventionally, the positive electrode is denoted the cathode and the negative electrode is denoted the anode regardless of whether the cell is charging of discharging. The typical anode for Li-ion cells is graphite. Graphite contains layers of graphene, which is a two-dimensional hexagonal carbon lattice. Graphite is both electronically and ionically conductive.

There are several cathodes that are used in Li-ion cells, such as LCO, Lithium Manganese Oxide ($LiMnO_4$, LMO), Lithium Nickel Manganese Cobalt Oxide ($LiNiMnCoO_2$, NMC), Lithium Iron Phosphate ($LiFePO_4$, LFP), and Lithium Nickel Cobalt Aluminum Oxide ($LiNi_{0.8}Co_{0.15}Al_{0.05}O_2$, NCA). The specific charge and energy capacity, $Q_{specific}$ and $E_{specific}$ respectively, of these cathodes are seen in Table 1.1. The operating voltage range and the average voltage are also shown. The

energy capacity shown in the table is higher than what is usually reported for Li-ion batteries. This is because the specific energy capacity shown is only for the cathode material and does not account for the weight of other battery components.

Each type of cathode has its benefits and drawbacks. LCO cannot charge above 4.2 V so has low energy. LMO supplies high power and does not use cobalt, but has a short lifespan. NMC is high power and high energy, but is dependent on cobalt. LFP is low power, but is safe. NCA is high energy but relies on cobalt. Any electrode that contains cobalt is inherently more expensive, as cobalt is costly and difficult to obtain. The majority of cobalt is mined in the Congo [14]. The fact that cobalt is not produced in the USA, along with ethical issues concerning the mining practices in the Congo, means that battery design would benefit from losing dependence on cobalt.

Table 1.1: Cathodes used in Li-ion cells.

Parameter	Units	LCO	LMO	NMC	LFP	NCA
Molecular Mass	g/mole	97.9	126	212	158	189
Voltage Range	V	3.0 - 4.2	3.0 - 4.2	3.0 - 4.2	2.5 – 3.65	3.0 - 4.2
Average Voltage	V	3.6	3.7	3.7	3.3	3.6
$\mathbf{Q_{specific}}$	Ah/kg	137	213	126	170	141
$\mathbf{E_{specific}}$	Wh/kg	493	786	468	560	510

LMO Cathode:

Consider a Li-ion cell with a LMO cathode. During charge, the reactions at the cathode and anode, as well as the overall reaction of the cell, are as seen in Eq. 1.4. During discharge, the reactions at the anode and cathode, and the overall cell reaction, are as seen in Eq. 1.5. One mole of LMO and one mole of graphite produce one mole of electrons.

Charging:

$$\begin{aligned} \text{Cathode:} \quad & 6C + Li^+ + e^- \rightarrow C_6Li \\ \text{Anode:} \quad & LiMnO_4 \rightarrow MnO_4 + Li^+ + e^- \\ \text{Overall:} \quad & 6C + LiMnO_4 \rightarrow C_6Li + MnO_4 \end{aligned} \tag{1.4}$$

Discharging:

$$\begin{aligned} \text{Anode:} \quad & C_6Li \rightarrow 6C + Li^+ + e^- \\ \text{Cathode:} \quad & MnO_4 + Li^+ + e^- \rightarrow LiMnO_4 \\ \text{Overall:} \quad & C_6Li + MnO_4 \rightarrow 6C + LiMnO_4 \end{aligned} \tag{1.5}$$

LFP Cathode:

Now consider a Li-ion cell with a LFP cathode. During charge, the reactions at the cathode and anode, as well as the overall reaction of the cell, are as seen in Eq. 1.6. During discharge, the reactions at the anode and cathode, and the overall cell reaction, are as seen in Eq. 1.7. One mole of LFP and one mole of graphite produce one mole of electrons.

Charging:

$$\begin{aligned} \text{Cathode:} \quad & 6C + Li^+ + e^- \rightarrow C_6Li \\ \text{Anode:} \quad & LiFePO_4 \rightarrow FePO_4 + Li^+ + e^- \\ \text{Overall:} \quad & 6C + LiFePO_4 \rightarrow C_6Li + FePO_4 \end{aligned} \tag{1.6}$$

Discharging:

$$\begin{aligned} \text{Anode:} \quad & C_6Li \rightarrow 6C + Li^+ + e^- \\ \text{Cathode:} \quad & FePO_4 + Li^+ + e^- \rightarrow LiFePO_4 \\ \text{Overall:} \quad & C_6Li + FePO_4 \rightarrow 6C + LiFePO_4 \end{aligned} \tag{1.7}$$

NMC Cathode:

Now consider a Li-ion cell with a NMC cathode. During charge, the reactions at the cathode and anode, as well as the overall reaction of the cell, are as seen in Eq. 1.8. During discharge, the reactions at the anode and cathode, and the overall cell reaction, are as seen in Eq. 1.9. One mole of NMC and one mole of graphite produce one mole of electrons.

Charging:

$$\begin{aligned} \text{Cathode:} \quad & 6C + Li^+ + e^- \rightarrow C_6Li \\ \text{Anode:} \quad & LiNiMnCoO_2 \rightarrow NiMnCoO_2 + Li^+ + e^- \\ \text{Overall:} \quad & 6C + LiNiMnCoO_2 \rightarrow C_6Li + NiMnCoO_2 \end{aligned} \tag{1.8}$$

Discharging:

$$\begin{aligned} \text{Anode:} \quad & C_6Li \rightarrow 6C + Li^+ + e^- \\ \text{Cathode:} \quad & NiMnCoO_2 + Li^+ + e^- \rightarrow LiNiMnCoO_2 \\ \text{Overall:} \quad & C_6Li + NiMnCoO_2 \rightarrow 6C + LiNiMnCoO_2 \end{aligned} \tag{1.9}$$

NCA Cathode:

Now consider a Li-ion cell with a NCA cathode. During charge, the reactions at the cathode and anode, as well as the overall reaction of the cell, are as seen in Eq. 1.10. During discharge, the reactions at the anode and cathode, and the overall cell reaction, are as seen in Eq. 1.11. One mole of NCA and one mole of graphite produce one mole of electrons.

Charging:

$$\begin{aligned} \text{Cathode:} \quad & 6C + Li^+ + e^- && \rightarrow \quad C_6Li \\ \text{Anode:} \quad & LiNi_{0.8}Al_{0.05}Co_{0.15}O_2 && \rightarrow \quad Ni_{0.8}Al_{0.05}Co_{0.15}O_2 + Li^+ + e^- \\ \text{Overall:} \quad & 6C + LiNi_{0.8}Al_{0.05}Co_{0.15}O_2 && \rightarrow \quad C_6Li + Ni_{0.8}Al_{0.05}Co_{0.15}O_2 \end{aligned} \tag{1.10}$$

Discharging:

$$\begin{aligned} \text{Anode:} \quad & C_6Li && \rightarrow \quad 6C + Li^+ + e^- \\ \text{Cathode:} \quad & Ni_{0.8}Al_{0.05}Co_{0.15}O_2 + Li^+ + e^- && \rightarrow \quad LiNi_{0.8}Al_{0.05}Co_{0.15}O_2 \\ \text{Overall:} \quad & C_6Li + Ni_{0.8}Al_{0.05}Co_{0.15}O_2 && \rightarrow \quad 6C + LiNi_{0.8}Al_{0.05}Co_{0.15}O_2 \end{aligned} \tag{1.11}$$

1.6 Lithium Sulfur Background

Li-S batteries have a lithium anode and sulfur cathode. The physical and chemical properties of lithium and sulfur are found in Table 1.2 [15, 16]. Sulfur is part of the Earth's crust, so is abundant and is produced worldwide, including USA [17]. Lithium is also abundant, and the majority of lithium production is in Australia, Chile, and China [18].

Table 1.2: Physical and chemical properties of lithium and sulfur.

Parameter	Units	Lithium	Sulfur
Molecular Mass	g/mole	7.0	32
Boiling Point	°C	1,342	445
Melting Point	°C	180	118-120
Density	g/mL	0.534	2.07
Appearance		Solid	Solid powder
Enthalpy, H°	kJ/mole	4.632	4.412
Entropy, S°	J/mole-K	29.12	32.05

A simple diagram of a Li-S cell can be seen in Figure 1.3. The cell consists of a positive electrode, a negative electrode, and an electrolyte. Lithium is the negative electrode and sulfur (S_8) is the positive electrode. These electrodes are the anode and cathode of the cell.

A newly built Li-ion cell begins in the charged state, so the cell must begin with discharging. Unlike Li-ion, the charge and discharge reactions are not intercalation. When discharging, the lithium ions move from the negative electrode to the positive electrode as seen in Figure 1.4a. The positive cathode, sulfur, begins as S_8 but breaks down into sulfur atoms that then react with the electrons and lithium ions to form Li_2S. The reactions at the anode and cathode, and the overall cell reaction, are seen in Eq. 1.12. The overall reaction shows that one mole of sulfur and two moles of lithium produce two moles of electrons. This is double that of the Li-ion cells discussed in the previous section. The charge reactions for a Li-S cell at the anode, cathode, and overall cell reaction are seen in Eq. (1.13). During charging, the lithium ions move from the positive electrode to the negative electrode as seen in Figure 1.4b.

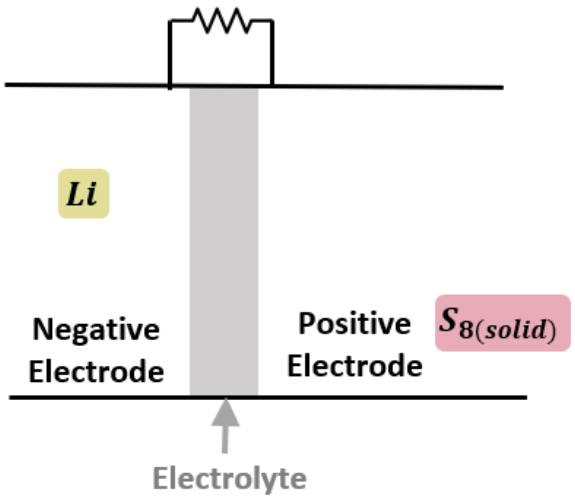

Figure 1.3: Simple diagram of Li-S cell, electrodes are lithium (Li) and sulfur S_8.

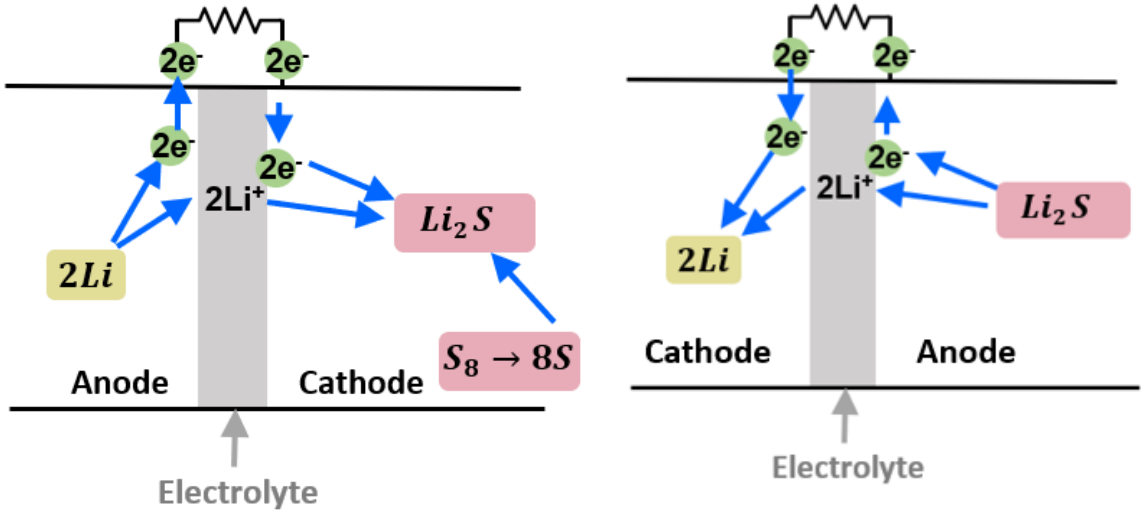

(a) Discharging.

(b) Charging.

Figure 1.4: Charge and discharge reactions in a Li-S cell with sulfur and lithium electrodes.

Discharging:

$$\begin{aligned} \text{Anode:} \quad & 2Li & \rightarrow \quad & 2Li^+ + 2e^- \\ \text{Cathode:} \quad & S + 2Li^+ + 2e^- & \rightarrow \quad & Li_2S \\ \text{Overall:} \quad & S + 2Li & \rightarrow \quad & Li_2S \end{aligned} \tag{1.12}$$

Charging:

$$\begin{aligned} \text{Cathode:} \quad & 2Li^+ + 2e^- & \rightarrow \quad & 2Li \\ \text{Anode:} \quad & Li_2S & \rightarrow \quad & S + 2Li^+ + 2e^- \\ \text{Overall:} \quad & Li_2S & \rightarrow \quad & S + 2Li \end{aligned} \tag{1.13}$$

The release of two electrons per sulfur atom contributes to the high theoretical specific charge capacity of Li-S. Due to the low atomic mass of sulfur, and the two electrons released from the reaction between sulfur and lithium, the Li-S cell promises a high specific charge capacity. This high capacity is the main reason why Li-S primary (non-rechargeable) cells have been studied since the 1960s. However for secondary (rechargeable) cells, complications arise

due to side reactions which can diminish cell performance.

Figure 1.5 shows the flow of ions and electrons through a Li-S cell during the discharge process. The ions can be transported through the electrolyte as it is ionically conducting. The electrons can move through the anode and cathode, but not through the electrolyte as it is electronically insulating. The external wire connecting the anode to the cathode through a load provides a path of transport for the electrons to move from the anode to the cathode. The solid electrolyte interface (SEI) layer forms on the anode due to reactions between the electrolyte and the anode materials and serves as an ionically conducting and electronically insulating layer. Some electrons are also caught up in cyclic side reactions called the polysulfide (PS) shuttle effect, a complication that arises in rechargeable conventional Li-S cells.

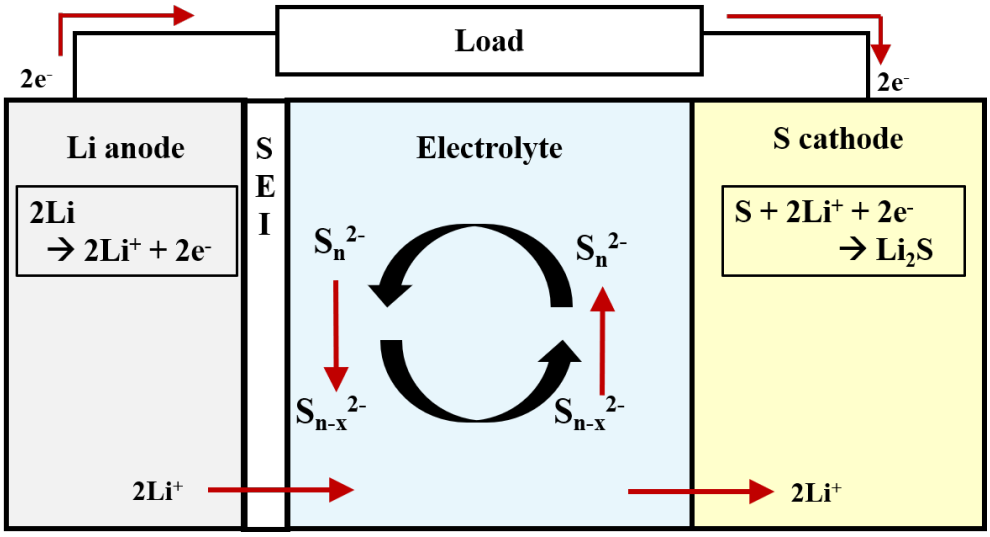

Figure 1.5: Discharge mechanisms and polysulfide shuttle effect in a Li-S cell.

1.7 Lithium Sulfur Benefits and Complications

The PS shuttle effect contributes to both a low cycle life and a self-discharge of the battery. The reaction at the cathode actually proceeds in a number of steps, with various PS as side

products. Barchasz *et al.* [19] detailed the PS species resulting from this multi-step process. As seen in Figure 1.5, the high-order PS migrate toward the anode, react with the lithium metal, reduce to low-order PS, migrate back to the cathode, form high-order PS again, and continue. The electrons are being caught up in this shuttle instead of traveling through the external wire and powering the load. This shuttle results in a loss of sulfur and lower efficiency [20]. The conventional Li-S cathode uses elemental sulfur as the active material and is highly susceptible to this shuttle effect, but state-of-the-art cathodes have been developed to inhibit this PS shuttle effect [21–23].

There are other complications that could be critical for eVTOL. Firstly, the cycle count (one cycle = one charge and one discharge) is poor compared to Li-ion. Secondly, these batteries self-discharge. However this is not an issue for eVTOL because unlike cars, the charge need not be retained for weeks or months but only a few hours at a time or a the most one day. The principal concern is high C-Rates, i.e. high power, as this behavior is unknown and typically less studied due to the lack of aviation focus in battery research. Fundamentally it translates to high current per unit area of the electrodes. High C-Rates of 20C or more are available for drones, but this is misleading as it pertains to low energy, so a small current or low specific power will still show a high C-Rate.

1.8 Primary Lithium Sulfur Batteries

Primary (non-rechargeable) Li-S batteries have been researched since the 1960s. Danuta and Juliusz [24] submitted a patent in 1962 detailing the possibility of a battery using a lithium anode and sulfur cathode. Four years later, Rao [25] patented high specific energy metal-sulfur

cells that use organic electrolytes. Rao also gave the theoretical specific energy for Li-S cells as 1,136 Wh/lbs (2,502 Wh/kg). The first patent for specifically Li-S cells, that is, a lithium anode and sulfur cathode, was in 1968 by Nole and Moss [26]. In 1980, Linden and McDonald [27] published results of a lithium sulfur dioxide ($LiSO_2$) battery that achieved a specific energy of 330 Wh/kg. A study in 1991 by Pitre [28] collected constant current discharge data on Honeywell $LiSO_2$ batteries at various temperatures. Pitre found that these cells performed best at 40°C. Three years later in 1994, Levy and Bro [29] published a book titled "Battery Hazards and Accident Prevention" including a chapter on $LiSO_2$ batteries. The chapter discusses the dangers of sulfur dioxide gas exposure, thermal runaway, and fast charging. In 2007, Ratnakumar *et al.* [30] researched the $LiSO_2$ batteries deployed on NASA's 2003 Mars Spirit and Opportunity rovers. While the rovers are powered by Li-ion batteries and solar cell arrays, the entry, descent, and landing were supported by $LiSO_2$ batteries. Based on the voltage data collected from the rovers, Ratnakumar *et al.* developed a model for the depassivation of $LiSO_2$ cells and were able to accurately predict the voltage when compared to the experimental data. Depassivation is the removal of a surface oxide layer from the battery electrodes that would otherwise hinder the battery performance. More recently in 2015, Ma *et al.* [31] developed a primary Li-S battery with a novel cathode design that achieved a specific energy of 504 Wh/kg_{Sulfur}. While this is an impressive achievement, for eVTOL applications a secondary (rechargeable) battery is required.

Primary batteries do have some advantages that are utilized today. Primary batteries can immediately provide power and have a long shelf life. This makes Li-S primary batteries desirable for defense and military uses. Another modern application of primary Li-S batteries is in cardiac defibrillators, such as the battery pack shown in Figure 1.6a. Figure 1.6b shows another primary Li-S battery manufactured by the French company SAFT.

(a) Primary $LiSO_2$ battery for defibrillators.

(b) Saft primary $LiSO_2$ battery.

Figure 1.6: Commercial primary Li-S batteries.

1.9 Secondary Lithium Sulfur Batteries

The PS shuttle effect that occurs in secondary (rechargeable) Li-S cells decreases the life of the batteries due to the loss of lithium and sulfur to PS formation. In the past two decades, researchers have studied utilizing modern, state-of-the-art materials and methods to suppress the PS shuttle effect and make secondary Li-S batteries viable.

There are various companies researching Li-S technology, such as Sion Power, Lyten, Polyplus, and Theion. These companies are working towards unlocking the full potential of Li-S technology and applying it to aviation, but publications are rare. As of yet, no Li-S battery powerful enough for passenger eVTOL has been realized. Sion Power's Licerion Li-S battery can be seen in Figure 1.7a, and Lyten's LytCel Li-S batteries can be seen in Figure 1.7b. In 2008, Li-S batteries were proven capable of flight but only for low/drip power on Airbus's Zephyr 6 aircraft powered by Sion Power's Li-S technology.

Research on secondary Li-S chemistries grew in the 2000s with focus on cell degradation,

(a) Sion Power's secondary Li-S battery.

(b) Lyten's secondary Li-S battery.

Figure 1.7: Commercial secondary Li-S batteries.

failure mechanisms, and extending the cycle life [20]. There is a vast literature on rechargeable Li-S with many reviews focusing on research trends and advances [20, 32–34].

As of 2009, studies showed that secondary Li-S batteries could achieve high specific energy and power, but had poor cycle life, low rate capabilities, and a high self-discharge behavior [20]. Part of this is due to the insulating nature of sulfur. This leads to low electronic conductivity in the cathode. This was shown to be resolved by Shim *et al.* [35] by adding conductive carbon black to the sulfur cathode, which reduces the electrical resistance of the cathode. While this addition decreases the overall specific energy of the cell, it is a necessary additive.

These issues also stem from the PS formation and resulting shuttle effect, as shown by Mikhaylik and Akridge [36]. The self-discharge occurs when the cell is not in use; the sulfur dissolves into the solvent and is converted to PS. With the dissolution of sulfur in the solvent, the amount of sulfur available for the cell reaction in Eq. (1.12) decreases and leads to capacity decrease and poor cycle life. Furthermore, the PS then enter the shuttle effect which consumes electrons that would otherwise be involved with this reaction, decreasing the efficiency of the

cell.

There has been a significant effort to improve the performance of secondary Li-S batteries. Composite sulfur cathodes are widely considered to be a viable solution to the PS formation and low cycle life of Li-S batteries. In 2002, Wang *et al.* [21] developed a conductive polymer-sulfur composite by heating a mixture of polyacrylonitrile (PAN) powder and sulfur at 280°C-300°C for six hours. This is the first published use of this composite, denoted here as polyacrylonitrile-sulfur (PANS). Their results showed that this composite PANS material had a high specific capacity and had potential as a cathode material for advanced rechargeable batteries. Further research by Wang *et al.* [22] determined that Li-S cells utilizing this PANS cathode operate in a lower voltage range of 1.0-3.0 V compared to that of conventional Li-ion cells, 3.0-4.2 V.

In 2005, Yu *et al.* [37] fabricated PANS at various temperatures and measured the performance. Results showed that PANS formation at 450°C produced the best stability and performance. An in-depth comparison of PAN powders was performed by Pu *et al.* in 2007 [38]. Findings showed the importance of homogenous molecular structure on cell performance. He *et al.* in 2009 [39] reported an average voltage of 1.9 V. The overcharge characteristics of PANS Li-S cells were also investigated and after overcharging to 4.0 V the cells were not able to be discharged again.

Expanding on Wang *et al.*'s research, in 2015 Wei *et al.* [23] performed a study on the stability and efficiency of PANS Li-S cells. Results showed complete elimination of the PS formation and therefore the shuttle effect, thereby stabilizing the cells over numerous charge and discharge cycles of the cells and increasing the lifetime of the cells. There was also no self-discharge observed when using the PANS cathode.

In-depth reviews have provided insight into the electrolytes for Li-S cells. For Li-S cells utilizing a conventional sulfur cathode, there are various electrolytes that have been shown to

produce relatively high charge capacity [40]. The typical electrolyte for Li-S uses a dioxolane / dimethoxyethane (DOL/DME) solvent. Mikhaylik [41] proposed the addition of lithium nitrate ($LiNO_3$) to the electrolyte, as a way to suppress the PS shuttle effect. This additive is now widely used in conventional Li-S cells [40]. However for Li-S cells using composite sulfur-carbon cathodes such as PANS, the PS formation is already inhibited and different electrolytes could be researched. Wei *et al.* [23] found that Li-S cells with a PANS cathode are more stable when using a carbonate-based electrolyte, rather than the DOL/DME-based electrolyte found in conventional Li-S cells.

There have been numerous studies on the various aspects of a Li-S cell and countless attempts to optimize the performance. A variety of claims are made concerning the specific capacity and energy of Li-S cells, but a consistent comparison is hard to find between Li-S and Li-ion chemistries as the overhead weight is not identical. Furthermore, the research on Li-S has not yet been focused on eVTOL applications.

1.10 Technical Approach

The technical approach is a systematic comparison of Li-S and Li-ion electrochemistries.

A comprehensive sizing analysis was developed and verified with NASA. The sizing analysis was performed for an intracity mission and demonstrated the need for a high specific energy battery. The analysis set key battery performance targets for eVTOL applications.

Li-S and Li-ion coin cells were fabricated with identical overhead weight using established, and easily reproducible and verifiable techniques. For the Li-S cells, a PANS cathode was fabricated to avoid the PS shuttle effect. Cells were fabricated in batch to verify the repeatability

of the results. Consistency is a key contribution of this work. For Li-ion, in-house fabrication was avoided in favor of state-of-the-art materials in order to maximize their performance. This was important as Li-ion was the baseline relative to which any Li-S was being evaluated, so any benefits of Li-S discovered were genuine and not simply a result of a poor baseline. The measured capacities of the Li-S and Li-ion cells were always compared with theory for veracity. This established not only the accuracy of the fabrication but also the proper basis for theoretical limits, without ad hoc claims based on pure chemistry that can never be realized.

Testing began with steady-state discharge characteristics at low and high C-Rates. The charge capacity was measured and verified with theory, then converted to energy and power and compiled into a Ragone plot of specific power versus specific energy that can be used for design. The Ragone plot established the higher specific energy of Li-S compared to Li-ion at low C-Rates while also showing its rapid decrease above 1C.

In the next step, full cycles (fully discharging the cell) were compared to half cycles (discharging only halfway). Half cycles stabilized the Li-S cells, with no decrease in the specific energy for the first 100 cycles at least. This has an impact for eVTOL aircraft, as intracity eVTOL missions can be designed to operate at half cycles to optimize the battery performance.

Transient behavior was then measured. Frequency data were collected using electrochemical impedance spectroscopy (EIS), where a sinusoidal current was applied to the cells at varying frequencies from 1 Hz to 100,000 Hz, and the voltage response was determined. The response revealed the reason behind the low C-Rate behavior. The variation of impedance with cycle life was also examined.

The frequency data were used to identify internal electrical properties, construct an equivalent circuit model (ECM), and then extract model parameters. The model was transformed to the time

domain and step and pulse testing were performed on the cells. The ECM was applied to the collected time domain data and parameters were extracted.

1.11 Objectives

The overarching objective is to break the traditional isolation of electrochemistry and aeronautics, in particular rotary-wing aeronautics. The principal barrier to eVTOL is lack of sufficient power and energy. A comprehensive and consistent comparison of Li-S and Li-ion batteries is needed to evaluate any potential benefits of Li-S for eVTOL. This is accomplished by the following steps.

1. Develop a comprehensive sizing analysis and verify with NASA. Demonstrate the need for a high specific energy battery and set key battery performance targets for eVTOL applications.

2. Fabricate Li-S and Li-ion coin cells with identical overhead weight and utilize state-of-the-art materials.

3. Establish steady state discharge characteristics for high and low C-Rates. Compare the measured specific energy and power of Li-S and Li-ion cells as C-Rate increases.

4. Collect transient data and develop a model in the time domain.

5. Investigate the potential impact of Li-S batteries on eVTOL sizing.

1.12 Organization

This thesis is organized into seven chapters. Following this introduction, Chapter 2 discusses the conceptual sizing analysis developed for eVTOL quadrotors, the verification with NASA, and the determination of key battery performance targets. Chapter 3 details the fabrication of Li-S and Li-ion coin cells and the calculation of theoretical capacity for both types of cells. Chapter 4 analyzes the steady state characteristics of the Li-S and Li-ion cells and models the steady state discharge characteristics. Chapter 5 collects and models transient data in both the frequency and time domain. Chapter 6 discusses the potential impact of the discovered advances on eVTOL sizing. Chapter 7 lists key conclusions. Throughout the dissertation, fundamental understanding is a main focus along with implications on eVTOL, where appropriate.

Chapter 2: Conceptual eVTOL Sizing

This chapter details the development and verification of the sizing analysis for an eVTOL quadrotor. Verification is performed with NASA for a specified mission with payload of 150 lbs (1 person), designated as Mission 1. After verification, a second mission, designated as Mission 2, is evaluated with a more practical payload of 400 lbs, similar to the Robinson R-22 helicopter. Various battery specific energies are evaluated, and the results demonstrate the need for a high specific energy battery. Key battery performance targets for eVTOL are determined.

2.1 Development of Sizing Analysis

To determine the impact of a high energy battery, a conceptual sizing method for an eVTOL quadrotor has been developed. The method is iterative and utilizes momentum theory which uses the disk loading and thrust to calculate the minimum power required for flight.

The power required includes the induced, profile, and parasitic power. The induced power C_{Pi} is calculated using Eq. (2.1), where λ_i is the induced inflow and C_T is the coefficient of thrust. The profile power C_{P0} is calculated using Eq. (2.2), where the advance ratio μ is the cruise speed over the rotor tip speed and σ is the solidity factor. The drag coefficient C_d was calculated using Eq. (2.3), where $C_{d0} = 0.0087$, $C_{d1} = 0.02$, and $C_{d2} = 0.8$. Angle of attack α

is found using Eq. (2.4).

$$C_{Pi} = \lambda_i C_T \tag{2.1}$$

$$C_{P0} = \frac{1}{8}\sigma C_d(1 + 4.6\mu^2) \tag{2.2}$$

$$C_d = C_{d0} + C_{d1}\alpha + C_{d2}\alpha^2 \tag{2.3}$$

$$\alpha = \frac{6\frac{C_T}{\sigma}}{5.73} \tag{2.4}$$

The parasitic power C_{Pp} was calculated using Eq. (2.5), where the aircraft drag area F in ft^2 must be determined. This was found by using Harris's proposed relation in Eq. (2.6), where k is the flat plate coefficient and $GTOW$ is the gross takeoff weight in lbs [42].

$$C_{Pp} = \frac{1}{2}\frac{F}{N_{rotor}A}\mu^3 \tag{2.5}$$

$$F = k\left(\frac{GTOW}{1000}\right)^{2/3} \tag{2.6}$$

The aircraft empty weight must be determined. This is the weight of the various aircraft components, and does not include payload weight. Empty weight was determined using Army Aeroflightdynamics Directorate (AFDD) models [43], as well as equipment weight data presented in Johnson *et al.*'s sizing results [6]. Each AFDD weight group model is determined using historical data from numerous rotorcraft. There are various weight groups included in the AFDD

models. Table 2.1 shows weight groups for a conventional rotorcraft on the left. These are modified with eVTOL groups on the right. For eVTOL, the Empennage and Wing Groups are not necessary. The Air Induction Group is not needed as there is no conventional turboshaft engine. The Anti-Icing Group is also not necessary as the aircraft will not fly long enough or high enough for icing to be an issue. The Fuel System Group is now the Battery Group, and the Engine Group is now the Electric Drive Group. The other groups are common to both. Technology factors used in the weight models can be found in Table 2.2, and all other necessary factors and constants in Table 2.3.

Table 2.1: AFDD weight groups.

Conventional Groups	**eVTOL Groups**
Wing	-
Rotor	Rotor
Fuselage	Fuselage
Empennage	-
Alighting Gear	Alighting Gear
Engine	Electric Drive
Air Induction	-
Fuel System	Battery
Hydraulic	Hydraulic
Anti-Icing	-
Other Equipment	Other Equipment

The rotor group uses the AFDD82 model. The weight of the rotor blades is determined using Eq. (2.7), which is based on 37 aircraft with an error of 7.7%. The weight of the rotor hub is found using Eq. (2.8), which is based on 35 aircraft with an error of 10.2%. N_{rotor} is the number of rotors, for a quadrotor $N_{rotor} = 4$. N_{blades} is the number of blades per rotor, R_{rotor} is the rotor radius in ft, c is the blade chord in ft, and V_{tip} is the hover tip speed in ft/s. The blade and hub flap frequencies, ν_{blade} and ν_{hub} respectively, are in per rev. The total weight of the rotor

group is found using Eq. (2.9).

$$W_{blades} = x_{blade}[0.02606 N_{rotor} N_{blades}^{0.6592} R_{rotor}^{1.3371} c^{0.9959} V_{tip}^{0.6682} \nu_{blade}^{2.5279}] \tag{2.7}$$

$$W_{hub} = x_{hub}\left[0.003722 N_{rotor} N_{blades}^{0.2807} R_{rotor}^{1.5377} V_{tip}^{0.4290} \nu_{hub}^{2.1414} \left(\frac{W_{blades}}{N_{rotor}}\right)^{0.5505}\right] \tag{2.8}$$

$$W_{Rotor} = W_{blades} + W_{hub} \tag{2.9}$$

The fuselage group uses the AFDD82 model and includes the basic fuselage structure weight and the crashworthiness weight, calculated using Eqs. (2.10) and (2.11), respectively. These are based on 35 aircraft with an error of 6.5%. The factor f_{ramp} is used to include the additional weight of a cargo ramp if applicable. The design flight load factor n_Z was set to Johnson *et al.*'s value [6]. The wetted area of the fuselage, S_{body}, is determined using the assumed radius and length of the fuselage ($r_{fuselage}$ and $l_{fuselage}$, respectively) and assuming a cylindrical shape. The factor f_{cw} is the crashworthiness weight factor. The total weight of the fuselage is found using Eq. (2.12).

$$W_{basic} = x_{basic}[5.896 f_{ramp}\left(\frac{GTOW}{1000}\right)^{0.4908} n_z^{0.1323} S_{body}^{0.2544} l_{fuselage}^{0.6100}] \tag{2.10}$$

$$W_{cw} = x_{cw}[f_{cw} W_{basic}] \tag{2.11}$$

$$W_{Fuselage} = W_{basic} + W_{cw} \tag{2.12}$$

The alighting gear group uses a fractional method defined in the AFDD documentation, seen in Eq. (2.13) as a fraction of gross weight. The factor f_{LG} is the landing gear weight fraction.

$$W_{LG} = f_{LG} GTOW \tag{2.13}$$

The electric drive consists of gearboxes, electric motors, a power conditioner, and cooling system. The gearbox weights are determined using the AFDD83 model as seen in Eq. (2.14), which is based on 30 aircraft with an error of 7.7%. P_{DS} is the required driveshaft power in horsepower, N_{gb} is the number of gearboxes on the aircraft, and Ω_{motor} and Ω_{rotor} are the motor and rotor speeds respectively in RPM. The factors f_{rs} and f_Q are the rotor shaft weight factor and the torque factor, respectively. The electric motor weights are determined using Eq. (2.15) from Ng and Datta [3]. This weight model is based on 17 aeronautical motors and has a maximum 30% error. In this model, W_{motor} is the motor mass in kg and Q is the maximum required torque in Nm. The maximum required torque in Nm is determined by Eq. (2.16), where P_{max} is the maximum power required in ft-lb/s, Ω is the rotor speed in Hz, k_{GR} is the gearbox reduction factor, and η_{GB} is the gearbox efficiency. The factor 1.356 is used to convert from ft-lb to Nm, as needed in Eq. (2.15). The power conditioner and cooling system weights are simply fractions of the motor weight, seen in Eqs. (2.17) and (2.18) respectively. The total weight of the electric drive system is found using Eq. (2.19).

$$W_{gb} = x_{gb}\left[(1 - f_{rs})57.72 P_{DS}^{0.8195} f_Q^{0.068} N_{gb}^{0.0663} \frac{\left(\frac{\Omega_{motor}}{1000}\right)^{0.0369}}{\Omega_{rotor}^{0.638}}\right] \tag{2.14}$$

$$W_{motors} = 0.4025Q^{0.17} \tag{2.15}$$

$$Q = 1.356\frac{\frac{P_{max}}{N_{rotor}}}{\Omega k_{GR}\eta_{GB}} \tag{2.16}$$

$$W_{pc} = f_{pc}W_{motors} \tag{2.17}$$

$$W_{mc} = f_{mc}W_{motors} \tag{2.18}$$

$$W_{EDrive} = W_{gb} + W_{motors} + W_{pc} + W_{mc} \tag{2.19}$$

The weight of the battery is dependent on the required energy for the mission and the specific energy of the battery, usable on-board the aircraft. The required energy for the mission is found using Eq. (2.20), where the energy is calculated using the required power for hover and cruise, P_h and P_{cr} respectively, and the hover and cruise flight times, t_h and t_{cr} respectively. The fuel cruise reserves, t_{res}, are included in the required energy. The weight of the battery is then determined using this required energy and the specific energy of the battery, available on-board the aircraft, as in Eq. (2.21).

$$E_{req} = (P_h t_h + P_{cr}(t_{cr} + t_{res})) \tag{2.20}$$

$$W_{battery} = \frac{E_{req}}{E_{battery,specific}} \tag{2.21}$$

The flight controls consist of non-boosted flight controls, control boost mechanisms, and boosted flight controls. The weights of these groups are calculated using AFDD82 models, seen in Eqs. (2.22) - (2.24) respectively, where f_{nb}, f_{hyd}, and f_{bsv} are the non-boosted weight, hydraulic weight, and ballistically survivable factors, respectively. Equation (2.22) is based on 20 aircraft with a 10.4% error, Eq. (2.23) is based on 21 aircraft with a 6.5% error, and Eq. (2.24) is based on 20 aircraft with a 9.7% error. The expression to determine w_{fc} is Eq. (2.25), where f_{mbsv} is another ballistically survivable factor and f_{red} is a redundancy factor. The total weight of the flight controls is found by Eq. (2.26).

$$W_{nb} = x_{nb}[f_{nb}(1 - f_{hyd})w_{fc}] \tag{2.22}$$

$$W_{mb} = x_{mb}[(1 - f_{hyd})w_{fc}] \tag{2.23}$$

$$W_b = x_b[0.02324 f_{bsv}(N_{rotor}N_{blades})^{1.0042} N_{rotor}^{0.1155} c^{2.2296} (0.01V_{tip})^{3.1877}] \tag{2.24}$$

$$w_{fc} = 0.2873 f_{mbsv}(N_{rotor}N_{blades})^{0.6257} c^{1.3286} (0.01V_{tip})^{2.1129} f_{red}^{0.8942} \tag{2.25}$$

$$W_{FC} = W_{nb} + W_{mb} + W_b \tag{2.26}$$

The hydraulic group weight depends on the flight control group weight. The weight of hydraulics for the flight controls and equipment is determined using Eq. (2.27), where f_{hyd} is the same hydraulic weight factor used in Eqs. (2.22) and (2.23). This weight model does not directly translate to quadrotors, as the quadrotor will not have a swashplate with full cyclics. Collective control is all that is needed to trim the rotors. The control angles for one rotor on a quadrotor are the collective control, θ_{75}, and the shaft tilt angles α_s and ϕ. Cyclic controls, and hence a swashplate, are not necessary. This can be accounted for by using a technology factor x_{hyd} less than 1.0. In this case, $x_{hyd} = 1$ for a conservative estimate.

$$W_{hyd} = x_{hyd}[f_{hyd} w_{fc}] \tag{2.27}$$

The weight of other equipment, W_{other}, was set to 161 lbs, based on Johnson *et al.*'s system weights [6]. This includes the weight of unusable fluids, automatic flight controls, instruments, mission equipment, electrical systems, environmental controls, and furnishings.

The empty weight of the aircraft can be found using Eq. (2.28).

$$W_{empty} = W_{Rotor} + W_{Fuselage} + W_{LG} + W_{EDrive} + W_{Battery} + W_{FC} + W_{hyd} + W_{other} \tag{2.28}$$

Table 2.2: Technology factors used in empty weight calculations.

Group	Technology Factor	Value
Rotor	x_{Blade}	0.92
	x_{Hub}	0.76
Fuselage	x_{basic}	0.76
	x_{cw}	0.90
Electric Drive	x_{gb}	0.74
Flight Controls	x_{nb}	1.0
	x_{mb}	1.0
	x_{b}	1.0
Hydraulics	x_{hyd}	1.0

Table 2.3: Parameters used in empty weight calculations.

Group	Parameter	Value
Rotor	ν_{Blade}	0.125/rev
	ν_{Hub}	0.125/rev
Fuselage	f_{ramp}	1.0
	n_Z	4.0
	l_{fuselage}	23 ft
	r_{fuselage}	6 ft
	f_{cw}	0.06
Alighting Gear	f_{LG}	0.0325
Electric Drive	f_{rs}	0.13
	f_{Q}	0.60
	k_{GR}	11.83
	η_{GB}	0.88
	η_{Motor}	0.85
	f_{pc}	0.5
	f_{mc}	0.5
Flight Controls	f_{nb}	0.60
	f_{hyd}	0.40
	f_{bsv}	1.0
	f_{mbsv}	1.0
	f_{red}	1.0
Hydraulics	f_{hyd}	0.40

2.2 Verification of Results

The in-house sizing analysis was verified with NASA's sizing results for a similar eVTOL quadrotor and mission detailed by Johnson *et al.* [6]. The details of this mission, designated here as Mission 1, are seen in Figure 2.1, with a payload of 250 lbs, disk loading of 2.5 lbs/ft^2, fuel cruise reserves of 20 minutes, and hover time of 4 minutes. The aircraft and system parameters are seen in Table 2.4. Figure 2.2 shows the present, in-house results and NASA's results for GTOW over varying range in n-miles and with four different battery specific energy values. Cruise speed is 70 knots, as the calculated best range speed exceeded this maximum cruise speed. The results shown are with various battery usable specific energy of 150, 200, 300, and 400 Wh/kg. The results match closely at higher specific energy values, but the present sizing code underpredicts the GTOW at lower specific energies. The error is due to the various assumptions and uncertainties present in the calculations. The major difference is that the present sizing analysis utilizes momentum theory as previously described, while NASA's analysis uses more refined methods. Given that the data are close and follow the same trends, the in-house present results are considered verified.

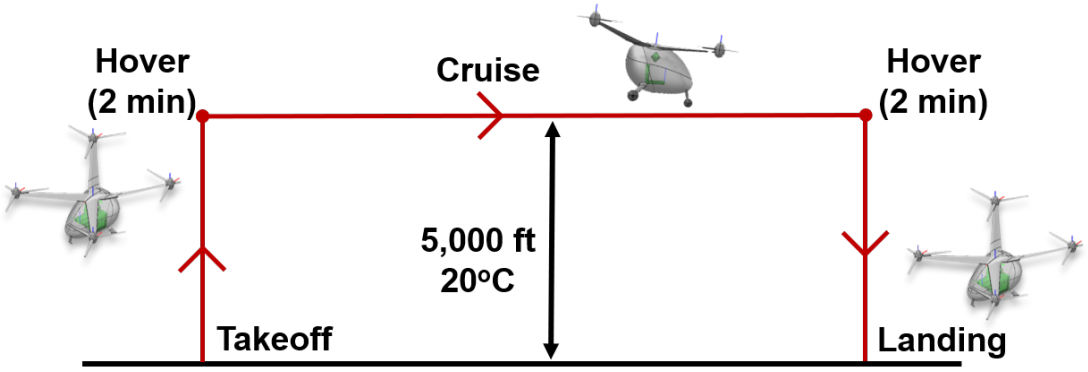

Figure 2.1: Mission 1, used for sizing analysis verification.

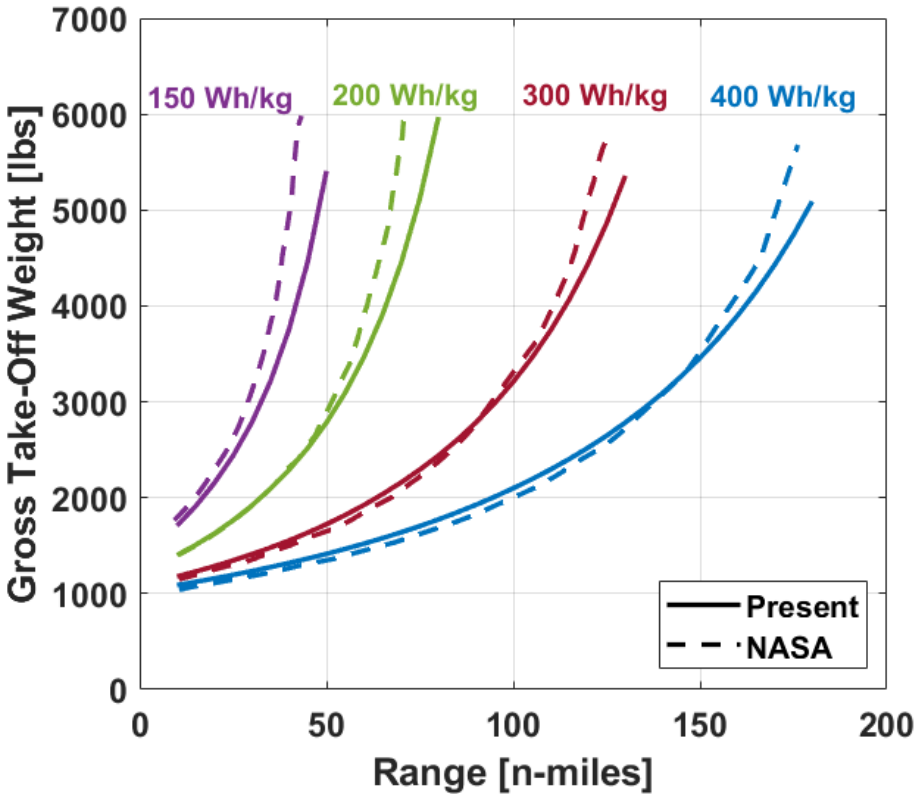

Figure 2.2: Present and NASA sizing results for an all-electric quadrotor; GTOW vs range for various battery specific energies; payload 250 lbs and disk loading 2.5 lbs/ft^2.

Table 2.4: Aircraft and system parameters used in sizing analysis verification.

Parameter	**Value**
Disk Loading	2.5 lbs/ft^2
Number of Rotors	4
Number of Blades per Rotor	4
Cruise Speed	118 ft/s (70 kts)
Tip Speed	450 ft/s
Fuel Cruise Reserves	20 min
Solidity σ	0.0646
Flat Plate Coefficient k	7.375
Installed Power Factor	1.5
Electric Motor Speed	4000 RPM
Induced Power Factor κ	1.15

2.3 Impact of Higher Specific Energy

With the analysis method verified, a second mission was evaluated using various battery specific energies. This new mission, Mission 2, is focused on intracity travel with a range of 50 n-miles, so 25 n-miles and back. The hover time is set at 5 minutes and cruise occurs at best range speed (or at maximum cruise speed if best range speed exceeds maximum cruise speed). The payload is increased to 400 lbs, which is equivalent to that of an R-22 helicopter. The fuel cruise reserves is decreased to 5 minutes. This allows the design to be closed for a large range of parameters even when the battery energy is very low.

Figure 2.3 shows the change in gross weight over a range of disk loadings for Mission 2, with an increasing specific energy of 150, 200, 300, and 400 Wh/kg. Note that current Li-ion technology can achieve a specific energy of approximately 150 Wh/kg and Li-S is projected to double that value for 300 Wh/kg. It is clear that a low disk loading generally results in the lowest GTOW, and that a higher energy battery results in a much lower GTOW. Additionally, implementing an optimal disk loading is critical for the quadrotor, as the GTOW quickly increases as the disk loading varies from the optimal value of 2.5 lbs/ft^2. The optimal disk loading does not drastically change with varying specific energies, so the aircraft design can remain the same if using a new, improved battery.

The empty weight breakdown of the aircraft, using either a 150 Wh/kg or 300 Wh/kg battery, can be found in Table 2.5. In both cases, the battery group is the heaviest. It is noteworthy that the battery accounts for more than half of the empty weight when using a 150 Wh/kg battery and only a third of the empty weight when using a 300 Wh/kg battery.

Figure 2.4 shows the change in rotor radius as the disk loading varies. For a battery specific

Table 2.5: Empty weight of aircraft for battery specific energies of 150 and 300 Wh/kg.

	Weight [lbs]	
	150 Wh/kg	**300 Wh/kg**
Rotor Group	372	153
Fuselage Group	434	306
Alighting Gear Group	121	59.1
Electric Drive Group	369	211
Battery Group	1,752	461
Flight Controls Group	31.3	17.0
Hydraulics Group	7.11	4.42
Other Equipment	161	161
Total Empty Weight	**3,247**	**1,373**

energy of 150 Wh/kg, the rotor radius at the optimal disk loading of 2.5 lbs/ft^2 is approximately 11 ft. This decreases to 7.6 ft for a specific energy of 300 Wh/kg. A smaller rotor radius is better suited for urban air mobility applications.

Figure 2.5 shows the required hover power as disk loading varies. Although the lowest power required does not occur at the optimal disk loading of 2.5 lbs/ft^2, the increase in required power at this optimal disk loading is only 2.8% - 4.3% depending on the specific energy. Minimizing the GTOW still allows for a disk loading with a relatively low power requirement.

Figure 2.6 shows the required hover C-Rate, i.e. the maximum C-Rate, required for the mission. High C-Rate is analogous with high current. Lower C-Rates (1-2C) are typically better for battery performance and extending the battery life. Increasing the specific energy from 150 Wh/kg to 300 Wh/kg decreases the required C-Rate from 1.6C to 1.48C.

In Figures 2.3 to 2.6, it is obvious that an increase in specific energy improves the aircraft design parameters. The results quantify the anticipated improvement. The increase from 150 Wh/kg to 200 Wh/kg, and then to 300 Wh/kg, causes dramatic improvements in all areas shown here. However, increasing the specific energy further to 400 Wh/kg only slightly improves

parameters. This shows that there is a diminishing return with regards to specific energy; an increase to 300 Wh/kg is desirable but improving the specific energy further will not produce a drastically improved aircraft.

Table 2.6 shows the conceptual quadrotor parameters for Mission 2 at a 50 n-mile range. The results for this mission for current battery technology (150 Wh/kg) and projected future battery technology (300 Wh/kg) can be seen. As expected, overall the mission using the highest specific energy battery is preferred over those using the lower specific energy batteries. Due to the diminishing return in regards to specific energy, a 300 Wh/kg battery is preferred.

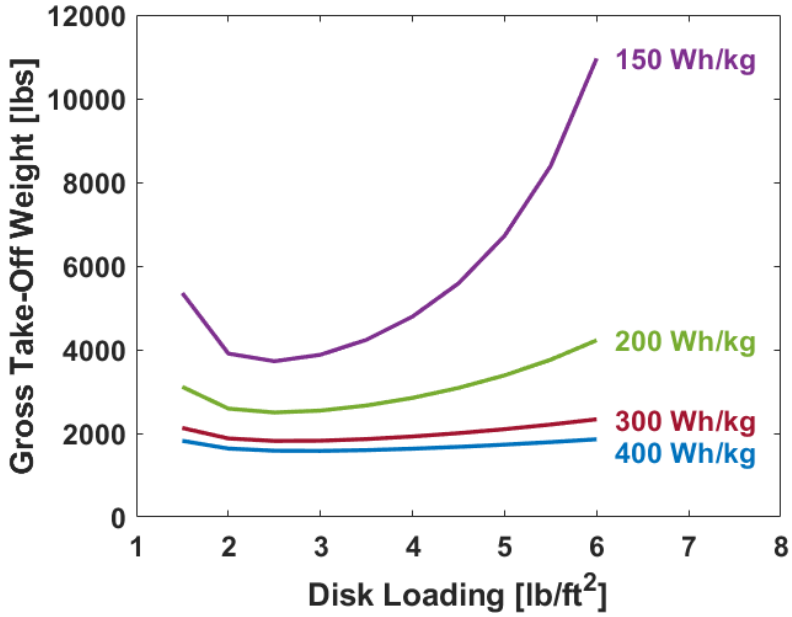

Figure 2.3: Effect of battery specific energy on GTOW as disk loading varies, payload 400 lbs and range 50 n-miles.

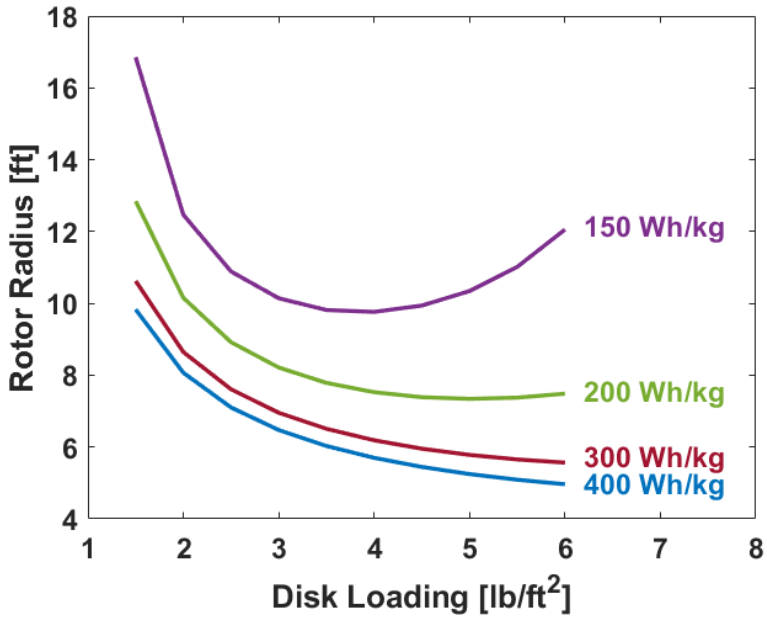

Figure 2.4: Effect of battery specific energy on rotor radius as disk loading varies, payload 400 lbs and range 50 n-miles.

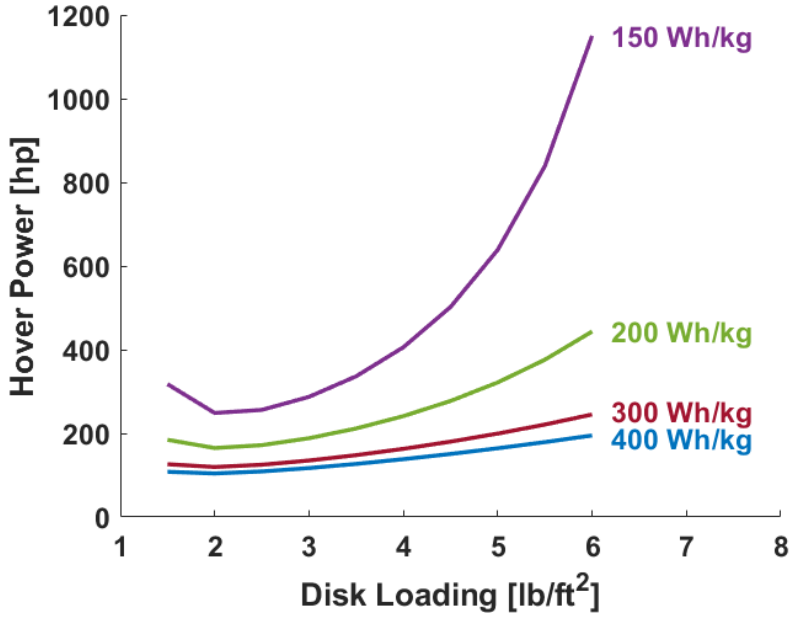

Figure 2.5: Effect of battery specific energy on hover power required as disk loading varies, payload 400 lbs and range 50 n-miles.

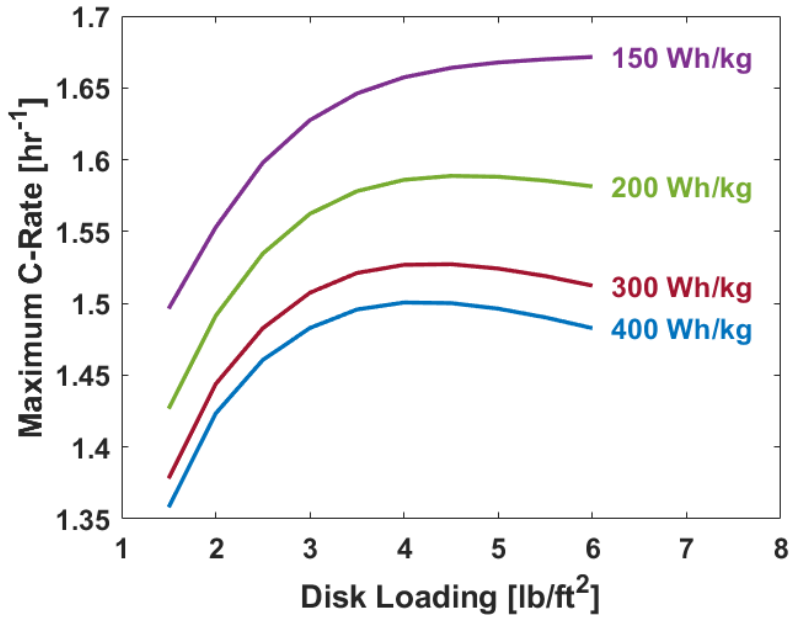

Figure 2.6: Effect of battery specific energy on maximum (hover) C-Rate as disk loading varies, payload 400 lbs and range 50 n-miles.

Table 2.6: All-electric quadrotor sizing results for Mission 2.

Parameter	**Units**		
Specific Energy	Wh/kg	150	300
$W_{Payload}$	lbs	400	400
Disk Loading	lbs/ft^2	2.5	2.5
Range	n-miles	50	50
Hover Time	min	5	5
Fuel Cruise Reserves	min	5	5
GTOW	lbs	3,724	1,818
Rotor Radius	ft	10.9	7.6
Hover Power	hp	256	125
V_{cr}	kts	70	70
L/D	-	4.59	4.20
FM	-	0.671	0.671
Total Energy	kWh	119	62.8
Battery Weight	lbs	1,753	461
C-Rate in Hover	hr^{-1}	1.60	1.48

Figure 2.7 shows the GTOW and C-Rate versus range for an eVTOL quadrotor, for Mission 2. Four lines are shown corresponding to varying battery specific energies in Wh/kg. In Figure 2.7a, the gross weights of the R-44 and R-22 helicopters are shown as references. A feasible eVTOL quadrotor with 50 n-mile range requires at least a 300 Wh/kg battery for an equivalent R-22 gross weight. In Figure 2.7b, the required cruise and hover C-Rates are shown for the

varying specific energies. At the optimal disk loading of 2.5 lbs/ft^2, the required maximum C-Rate is approximately 1.5C. The required C-Rate decreases as range increases, and is not affected by an increase in battery specific energy.

2.4 Summary

A conceptual sizing analysis was developed for eVTOL aircraft. The method was verified with results from NASA Ames Research Center. The analysis sized an electric quadrotor for 2-3 passengers for an intracity mission. The following key conclusions were found.

1. An increase in battery specific energy from 150 Wh/kg (achievable by current Li-ion technology) up to 300 Wh/kg improves the aircraft design. Specifically, it decreases the gross weight and rotor radius, making the aircraft more optimal for city travel.

2. There is a diminishing return when increasing the specific energy, as the increase from 150 Wh/kg to 300 Wh/kg causes dramatic improvements in all areas. Specifically, the GTOW decreased by 52%. However, increasing the specific energy further to 400 Wh/kg only slightly improves aircraft parameters - the GTOW only decreased by an additional 6%. Hence, an increase in specific energy to 300 Wh/kg is desirable.

3. Key battery performance targets were determined for eVTOL: a specific energy of 300 Wh/kg and a C-Rate of 1-2C.

With the key eVTOL targets set, design and fabrication of Li-S and Li-ion cells could begin.

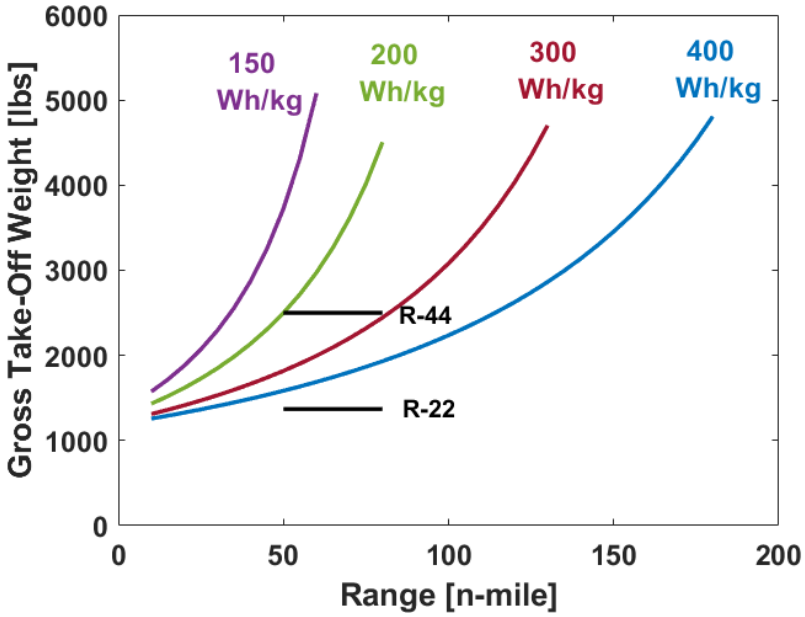

(a) Gross takeoff weight vs range.

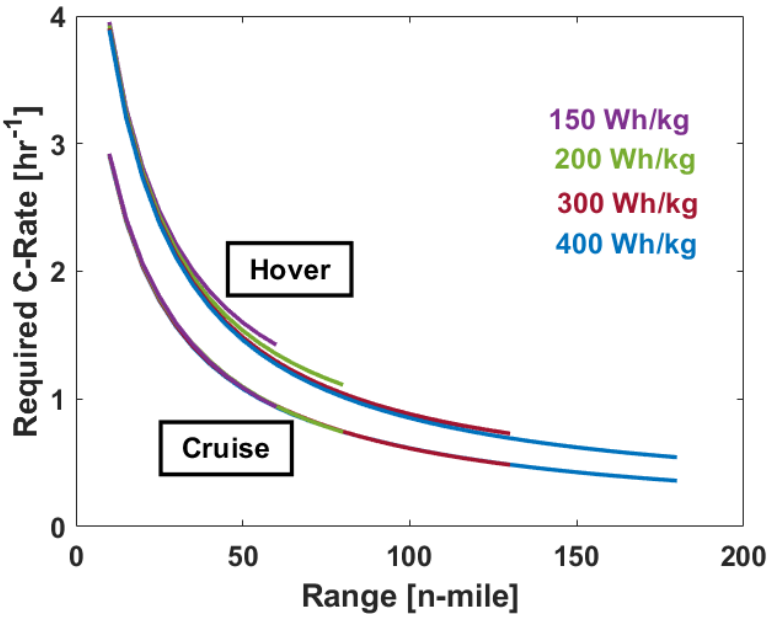

(b) C-Rate vs range.

Figure 2.7: Predicted gross takeoff weight and C-Rate vs range of an eVTOL quadrotor.

Chapter 3: Lithium Sulfur and Lithium-ion Cell Fabrication

This chapter details the design and fabrication of Li-S and Li-ion coin cells. A coin cell, also called a button cell, is a small single-cell battery shaped as a short cylinder. The Li-S and Li-ion cell designs have an identical overhead weight, which allows for a clear and consistent comparison. State-of-the-art materials are used to achieve an accurate representation of Li-S and Li-ion performance. Sulfur content in the Li-S cells is maximized as much as possible. Li-S and Li-ion theoretical charge capacities are calculated based on the cell designs.

3.1 Lithium Sulfur Coin Cell Fabrication

Li-S coin cells were fabricated using state-of-the-art facilities at the US Army Research Lab Adelphi. The main equipment used were an argon-filled glovebox, seen in Figure 3.1, and a Maccor battery cycler, seen in Figure 3.2, for cell fabrication and steady state testing, respectively. A ThermoScientific tube furnace, seen in Figure 3.3, was used to fabricate PANS active material. An Electric Aviation lab was also established at the University of Maryland, Alfred Gessow Rotorcraft Center. A Solartron Analytical Parstat Electrochemical Impedance Spectrometer (EIS), seen in Figure 3.4, was used to collect both steady state and transient data. A Tenney temperature chamber, seen in Figure 3.5, was utilized to ensure the steady state and transient tests were run at a fixed temperature (15^{o}C) when possible.

Figure 3.1: Argon-filled glovebox.

Figure 3.2: Maccor battery cycler.

Figure 3.3: ThermoScientific tube furnace.

The coin cells fabricated were type 2032. The first two digits represent the diameter in cm, which here is 2.0 cm. The last two digits represent the height in mm, which here is 3.2 mm. Over 40 Li-S type 2032 coin cells were fabricated and tested to characterize and analyze their

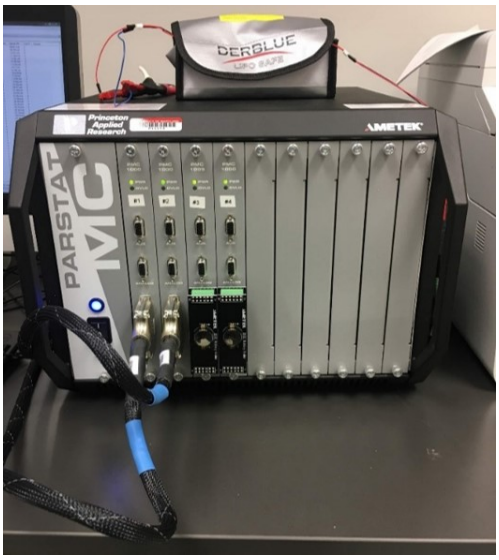

Figure 3.4: Solartron Analytical Parstat Electrochemical Impedance Spectrometer.

Figure 3.5: Tenney temperature chamber.

behavior. The cell components can be seen in Figure 3.6a. The casings, spring, and spacers are stainless steel and obtained from MTI Corp. The gasket is a polypropylene O-ring also obtained from MTI Corp. The separator is Celgard's 2325 trilayer membrane.

The cathode is fabricated in-house with a PANS active material, a carbon additive, and a binder. The fabricated cathode has a PANS weight fraction of 0.80. The PANS active material is fabricated following a process described by Wei *et al.* [23]. The electrolyte is 1.0 Molar (M) Lithium hexafluorophosphate ($LiPF_6$) in ethylene carbonate / ethyl methyl carbonate (EC/EMC),

obtained from Sigma Aldrich. A fabricated coin cell can be seen in Figure 3.6b. A weight breakdown of the cell can be found in Table 3.1. Note that the scale was not sensitive enough to capture the mass of the separator. The total Li-S cell mass is 3.445 g.

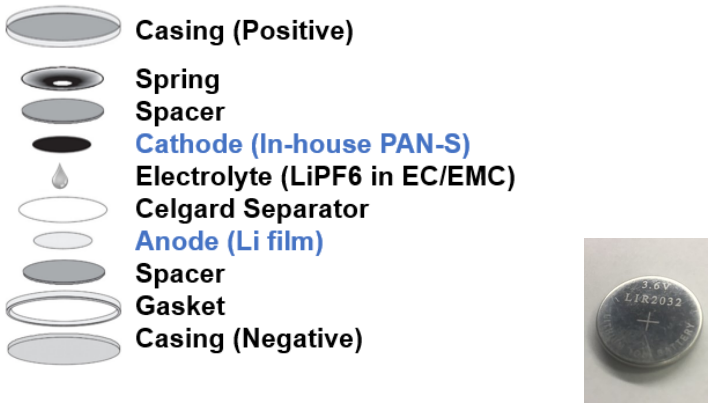

(a) (b)

Figure 3.6: a) Li-S cell components; b) Fabricated Li-S cell.

Table 3.1: Weight breakdown of Li-S coin cell.

Component	Weight [g]
Positive and Negative Casings + Gasket	2.8
Spring and Spacers	0.56
Separator	¡0.0001
Electrolyte	0.0762
Electrodes	$3.9 \cdot 10^{-3}$

The cathode for the Li-S cells uses in-house fabricated PANS active material. To make the PANS active material, the raw materials, PAN powder (obtained from Sigma Aldrich) and sulfur powder (obtained from Sigma Aldrich), are mixed as seen in Figure 3.7a to make what is called the cathode starter. This cathode starter is then put into a glass vial and heated in a tube furnace as seen in Figure 3.7b. The furnace is heated to 350°C for 1 hour, held at 350°C for 3 hours, heated to 450°C for 30 minutes, then held at 450°C for 20 minutes. The furnace is then allowed to cool to room temperature. After this step, the PANS active material is synthesized and is ready

to use. During synthesis, some sulfur is lost through side reactions such as gaseous hydrogen sulfide formation. Since sulfur is the contributor of capacity, the amount of sulfur present in the PANS active material must be determined. To determine the weight fraction of sulfur (X_S) in the PANS, the masses of the sulfur (S), the input cathode starter mass (Starter), and the output PANS mass (PANS) are recorded and the change in mass (ΔS) is calculated, assuming the mass lost must be only sulfur.

$$\Delta S = \text{Starter} - \text{PANS}$$

$$X_S = \frac{\text{S} - \Delta\text{S}}{\text{PANS}}$$

The ratio of PAN powder to sulfur powder determines the amount of sulfur ultimately present in the PANS output. For the baseline tests, an initial ratio of 1:3 PAN:S by weight was used, so the weight fraction of sulfur in the cathode starter was 0.75. The resulting weight fraction of sulfur in the PANS output was 0.54.

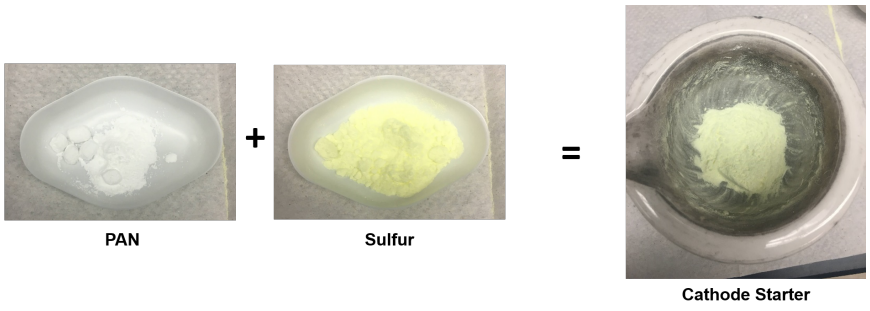

(a)

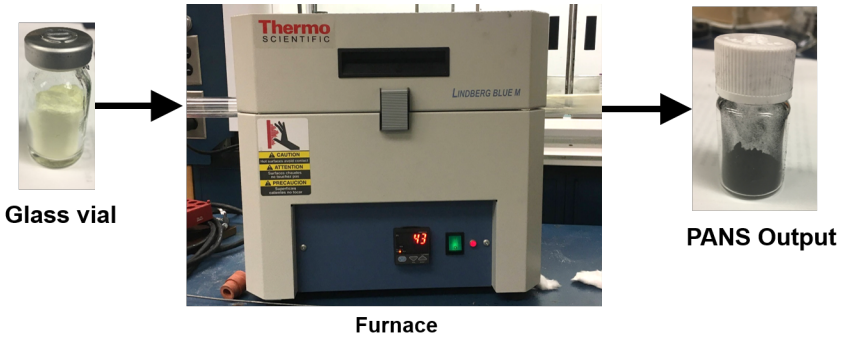

(b)

Figure 3.7: a) Raw materials PAN powder and sulfur powder, mixed to create the cathode starter, b) Glass vial with cathode starter, tube furnace used to synthesize the PANS active material, and glass vial with PANS output.

3.2 Sulfur Content

The sulfur content of the PANS output was investigated systematically. The cathode active material is the source of energy, and the active material is the PANS, which has a weight fraction of 0.80 in the cathode. The capacity is dependent on the amount of sulfur present in the PANS. An increase in sulfur would increase the energy and charge capacity. Towards this end, the initial ratio of PAN:S by weight was varied. Figure 3.8 shows the percentage of sulfur in the PANS output for various initial ratios. The results show that the 1:3 ratio ultimately retained the highest amount of sulfur in the output. Therefore, this ratio was selected in our fabrication.

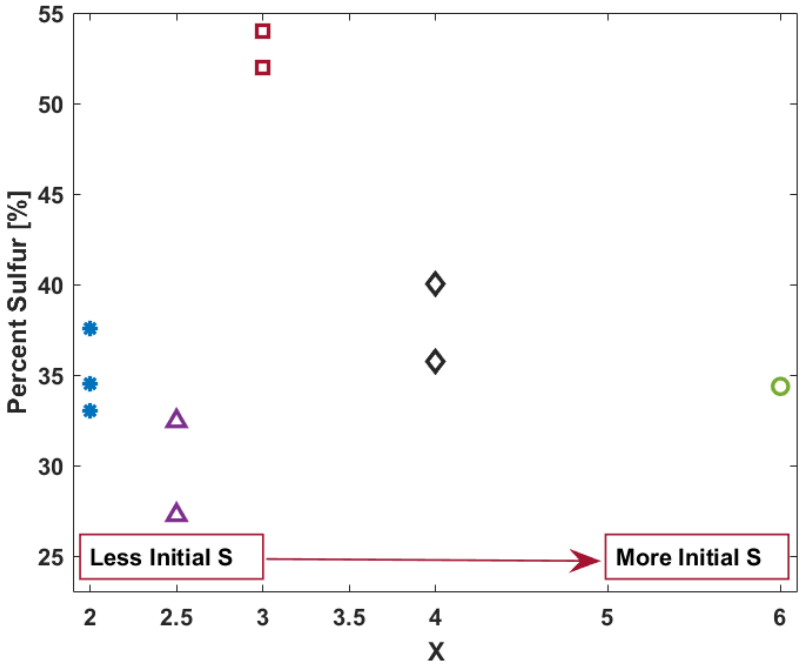

Figure 3.8: Percentage of sulfur present in the PANS output for various initial mass ratios 1:X of PAN:S.

3.3 Lithium Sulfur Theoretical Capacity

Once the cell is fabricated, the first task is to estimate its theoretical capacity to later validate the fabrication process. There are charge capacity and energy capacity. The charge capacity is calculated here; the energy capacity is calculated later using the precise voltage measurements. The charge capacity reported here is specific charge capacity Q in mAh/g, which is charge capacity divided by the mass of the electrodes, both anode and cathode. Equation (3.1) is used to calculate Q, where n is the number of electrons transferred in the cell reaction from Eq. (1.12), F is Faraday's constant as $F = 26,800 \frac{\text{mAh}}{\text{mole}}$, and W is the electrode mass in $\frac{\text{g}}{\text{mole}}$.

$$Q = \frac{nF}{W} \tag{3.1}$$

To calculate the mass of the cathode, all the components - PANS, carbon additive, and binder - must be included, not just the mass of the sulfur. First, the mass of sulfur W_S must be divided by the mass fraction of sulfur in the PANS material, X_S, to calculate the mass of PANS. This accounts for the non-sulfur components of the PANS. Next, the mass of PANS must be divided by the mass fraction of PANS, X_{PANS}, to calculate the mass of the cathode. This accounts for the carbon additive and binder. For this cell design, $X_{PANS} = 0.80$ and $X_S = 0.54$. W_S is the molecular mass of sulfur, 32 g/mole. The mass of the anode is $2W_{Li}$ where W_{Li} is the molecular mass of lithium, 7 g/mole. Thus the electrode mass becomes $W = 88.5 \frac{\text{g}}{\text{mole}}$.

$$W = 2W_{Li} + \frac{W_S}{X_{PANS} X_S}$$

With $n = 2$, the Li-S cell specific charge capacity Q was then 605 $\frac{\text{mAh}}{\text{g}}$ or $\frac{\text{Ah}}{\text{kg}}$.

3.4 Lithium-ion Coin Cell Fabrication

Fabrication facilities for the Li-ion type 2032 coin cells were identical to those for the Li-S coin cells. Over 40 Li-ion coin cells were fabricated and tested to characterize and analyze their behavior. The components of the Li-ion cells can be seen in Figure 3.9, where only the cathode and anode materials are changed from the Li-S design. Everything else is kept the same. The cathode active material for Li-ion is a state-of-the-art lithium nickel cobalt aluminum oxide (NCA, $LiNi_{0.8}Co_{0.15}Al_{0.05}O_2$). The cathode is fabricated with the NCA active material, a carbon additive, and a binder. The weight fraction of NCA in the cathode, X_{NCA}, is 0.80. The electrolyte is 1.0M $LiPF_6$ in EC/EMC. Unlike the Li-S cells, the cathode is not fabricated in-house, but purchased to ensure that our baseline was indeed state-of-the-art. The anode was graphite, a typical Li-ion anode. The cathode and anode were purchased from SAFT. All components other than the electrodes remain unchanged, giving the Li-ion and Li-S cells the same overhead weight and allowing for a direct comparison between the two types of cells.

A weight breakdown of the cell can be found in Table 3.2. All components expect for the electrodes are identical to the Li-S weight breakdown shown in Table 3.1. The total Li-ion cell mass is 3.451 g, slightly higher than that of Li-S.

Table 3.2: Weight breakdown of Li-ion coin cell.

Component	**Weight [g]**
Positive and Negative Casings + Gasket	2.7
Spring and Spacers	0.56
Separator	¡0.0001
Electrolyte	0.0762
Electrodes	$9.4 \cdot 10^{-3}$

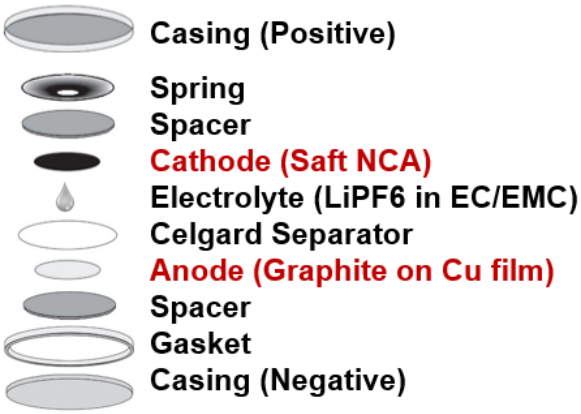

Figure 3.9: Li-ion cell components.

3.5 Lithium-ion Theoretical Capacity

The same equations can be used to calculate the specific capacity and energy of the Li-ion cell from the discharge reaction Eq. 3.2. The discharge reaction for a Li-ion cell at the anode and cathode are simple. A mole of NCA and a mole of graphite produce a mole of electrons.

To calculate the mass of the cathode, all the components - NCA, carbon additive, and binder - must be included, which is accomplished by dividing the mass of NCA by the mass fraction of NCA in the cathode, X_{NCA}. For this cell design, $X_{NCA} = 0.80$. W_{NCA} is the molecular mass of NCA, calculated using Eq. (3.2). The molecular masses of the elements present in NCA are seen in Table 3.3. Note that the mass of lithium is included in W_{NCA}. The mass of the anode is $6W_C$ where W_C is the molecular mass of carbon, 12 g/mole. Thus, the electrode mass becomes $W = 189\frac{\text{g}}{\text{mole}}$.

$$W_{NCA} = W_{Li} + 0.8W_{Ni} + 0.15W_{Co} + 0.05W_{Al} + 2W_O \tag{3.2}$$

Table 3.3: Masses of elements present in NCA.

Element	Molecular Mass [g/mole]
Lithium (Li)	7.0
Nickel (Ni)	58.0
Cobalt (Co)	59.0
Aluminum (Al)	27.0
Oxygen (O)	16.0

$$W = 6W_C + \frac{W_{NCA}}{X_{NCA}}$$

With $n = 1$, the Li-ion cell specific charge capacity Q was calculated to be 141 $\frac{\text{mAh}}{\text{g}}$ or $\frac{\text{Ah}}{\text{kg}}$. This is much lower than that of Li-S.

3.6 Summary

Li-S and Li-ion coin cells were fabricated with identical overhead, allowing for a clear and consistent comparison. Fabrication utilized state-of-the-art facilities at the US Army Research Lab Adelphi and the University of Maryland Alfred Gessow Rotorcraft Center. The Li-S cells were free of the polysulfide shuttle effect, as the PANS cathode does not allow the formation of polysulfides. The Li-ion cells used a state-of-the-art, modern cathode. The key conclusions are as follows.

1. Theoretical specific charge capacity of the Li-ion cells was calculated to be 141 Ah/kg and that of the Li-S cells to be 605 Ah/kg. The charge capacity was normalized by the mass of the electrodes, including the added carbon and binder. This is the proper normalization, as the cathodes must have the carbon and binder to operate.

2. A 1:3 ratio of PAN:S by weight maximized sulfur content in a Li-S cell and hence maximized specific charge capacity and energy capacity. This ratio retained the highest amount of sulfur in the PANS active material at 0.54 weight fraction of sulfur.

With the Li-S and Li-ion cells fabricated, testing began with steady state discharge analysis.

Chapter 4: Steady State Analysis and Modeling

This chapter discusses the steady state, i.e. constant current, testing and analysis of Li-S and Li-ion coin cells. Testing began with discharge of the cells at a very low current - a C-Rate of C/25. The data from the slow discharge allowed for a comparison of the measured charge capacity to the theoretical. The discharge characteristics were then collected for higher C-Rates, which allowed for the construction of a Ragone Plot of specific power versus specific energy. The cycle life of the Li-S and Li-ion cells was investigated, and the impact of half cycles on the cycle life was determined. Modeling of the steady state behavior was performed using the Shepherd model [44].

4.1 Discharge Curves

Testing begins with discharge curves. The first step is to have a slow discharge to measure specific charge capacity and then verify with the theoretical capacity. For discharge curves, constant current is drawn and the voltage is recorded. The current was set to a value that would discharge the cells in 25 hours, which corresponds to a C-Rate of $1/25\,\text{hr} = 0.04\text{hr}^{-1}$. The Li-S and Li-ion data of voltage over time for this 25 hour discharge can be found in Table 4.1. The discharge curve of voltage versus time for the Li-S and Li-ion cells, cycled at a constant current, can be seen in Figure 4.1. Because the capacity of the Li-S and Li-ion cells were

different, although the C-Rate was identical, the magnitude of the current was different. The current magnitude was found by multiplying the specific charge capacity Q by the active material mass m and the desired C-Rate as in Eq. (4.1). The active material is PANS for Li-S and NCA for Li-ion. The specific charge capacity was as calculated in Chapter 3 and the active material mass was measured.

$$i = mQCRate \tag{4.1}$$

The Li-S cells are discharged from 3.0 V to 1.0 V. The Li-ion cells are discharged from 4.2 V to 3.0 V. Over-discharging would cause corrosion of the internal cell materials as well as electrolyte decomposition, both of which can lead to cell failure. Hence the discharge stopped at 1.0 V and 3.0 V respectively for the Li-S and Li-ion cells. This state is considered a fully discharged state.

From this fundamental data, the charge capacity and energy capacity follow. Charge supplied, Q, is calculated by multiplying the current by time of discharge as seen in Eq. (4.2), where Q(t) is charge supplied until time t. Energy is calculated by multiplying the charge capacity by the voltage as in Eq. (4.3), where E(t) is energy supplied until time t. The instantaneous power can be determined with Eq. (4.4). The average power is calculated using Eq. (4.5), where E(T) is the energy capacity when fully discharged and T is the time of full discharge.

$$Q(t) = \int_0^t I d\tau \tag{4.2}$$

Table 4.1: Time and voltage data for C/25 discharge of Li-S and Li-ion cells.

Time [hr]	Li-S Voltage [V]	Li-ion Voltage [V]
0	2.935	4.173
0.5	2.224	4.110
1	2.188	4.087
2	2.140	4.045
3	2.110	4.001
4	2.085	3.957
5	2.055	3.919
6	2.023	3.884
7	1.995	3.850
8	1.967	3.811
9	1.944	3.770
10	1.921	3.732
11	1.900	3.698
12	1.880	3.668
13	1.861	3.642
14	1.841	3.618
15	1.823	3.597
16	1.804	3.576
17	1.786	3.550
18	1.765	3.521
19	1.741	3.487
20	1.706	3.446
21	1.650	3.399
22	1.554	3.359
23	1.382	3.317
23.4	1.312	3.281
24	1.180	3.226
25	1.053	3.031

$$E(t) = \int_0^t IV(\tau)d\tau \tag{4.3}$$

$$P(t) = IV(t) \tag{4.4}$$

$$P_{average} = \frac{E(T)}{T} \tag{4.5}$$

Figure 4.2 shows the voltage plotted against charge supplied Q(t). The charge capacity Q is the charge supplied at full discharge. The charge capacity divided by the electrode mass gives the measured specific capacity. This is compared with the theoretical value in Table 4.2. The measured specific capacities of the Li-S and Li-ion cells are in the general vicinity of the theoretical specific capacities. Furthermore, the Li-S has a significantly higher specific capacity compared to the Li-ion, as the Li-S electrode mass is less than half that of Li-ion.

Table 4.2: Measured charge capacity of Li-S and Li-ion cells compared to theoretical charge capacity.

	Units	**Li-S**	**Li-ion**
Q Measured	mAh	1.98	1.25
Electrode Mass	mg	3.9	9.4
Measured Q Specific	mAh/g	507	132
Theoretical Q Specific	mAh/g	605	141

The state of charge (SOC) is a measurement of how much charge is remaining on a battery. SOC can be calculated using Eq. (4.6), where Q(t) is the amount of charge supplied at time t, and Q(T) is the amount of charge supplied at the end of discharge - the charge capacity. Similarly, the depth of discharge (DOD) is a measurement of how much of the available charge capacity has been used, and can be calculated using Eq. (4.7). Figure 4.3 shows the Li-S and Li-ion data of voltage over SOC for the C/25 discharge, and the corresponding data can be found in Table 4.3.

$$\text{SOC} = 1 - \frac{Q(t)}{Q(T)} \tag{4.6}$$

$$\text{DOD} = 1 - \text{SOC} = \frac{Q(t)}{Q(T)} \tag{4.7}$$

Figure 4.4 shows the voltage plotted against energy capacity E(t). The Li-ion cells have a

Table 4.3: SOC and voltage data for C/25 discharge of Li-S and Li-ion cells.

SOC [%]	Li-S Voltage [V]	Li-ion Voltage [V]
100	2.935	4.173
97	2.293	4.127
94	2.188	4.086
91	2.150	4.054
88	2.125	4.021
85	2.101	3.988
82	2.082	3.955
79	2.060	3.926
76	2.037	3.900
73	2.013	3.874
70	1.989	3.848
67	1.969	3.820
64	1.951	3.789
61	1.934	3.758
58	1.918	3.730
55	1.900	3.700
52	1.885	3.681
49	1.870	3.66
46	1.855	3.640
43	1.841	3.623
40	1.826	3.606
37	1.812	3.591
34	1.798	3.575
31	1.784	3.557
28	1.769	3.535
25	1.749	3.511
22	1.727	3.485
19	1.699	3.454
16	1.656	3.421
13	1.593	3.384
10	1.483	3.356
7	1.342	3.327
4	1.191	3.271
1	1.080	3.189
0	1.006	3.004

higher energy than Li-S, as the operating voltage is higher. Figure 4.5 shows the instantaneous power versus the energy capacity. The average power is also shown. The Li-ion cells show a

higher power and energy compared to the Li-S cells. The discharge plots here are for the lowest C-Rate, hence are expected to show the highest energy and lowest power compared to higher C-Rates.

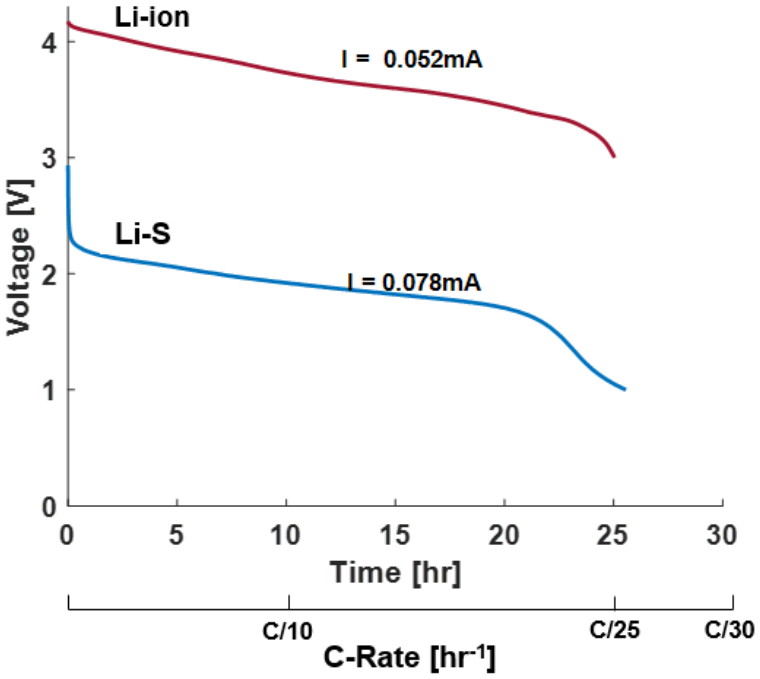

Figure 4.1: Voltage versus time of a Li-S cell and a Li-ion cell for constant currents.

4.2 High C-Rates of Lithium Sulfur

To test high power capabilities, Li-S cells were cycled at high C-Rates. High C-Rate is analogous with high current. Energy capacity decreases with an increasing C-Rate due to the reduction in the amount of transferred ions. Figure 4.6 shows the high C-Rate behavior of the Li-S cell, specifically how increasing the current diminishes the voltage drastically.

$$\text{C-Rate} = \frac{P_{ave}}{E} = \frac{1}{T}$$

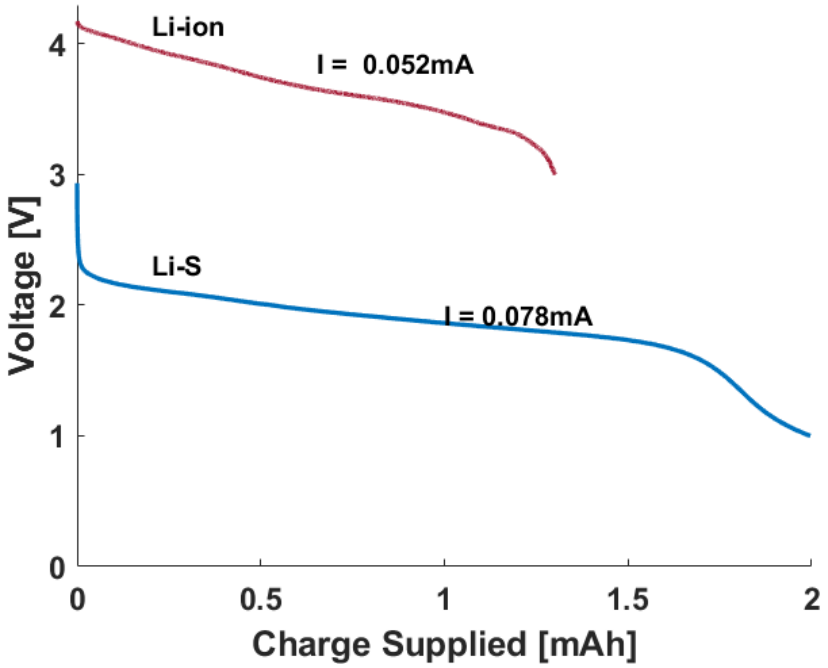

Figure 4.2: Voltage versus charge supplied for a Li-S and a Li-ion cell for constant currents. Maximum charge supplied is the charge capacity.

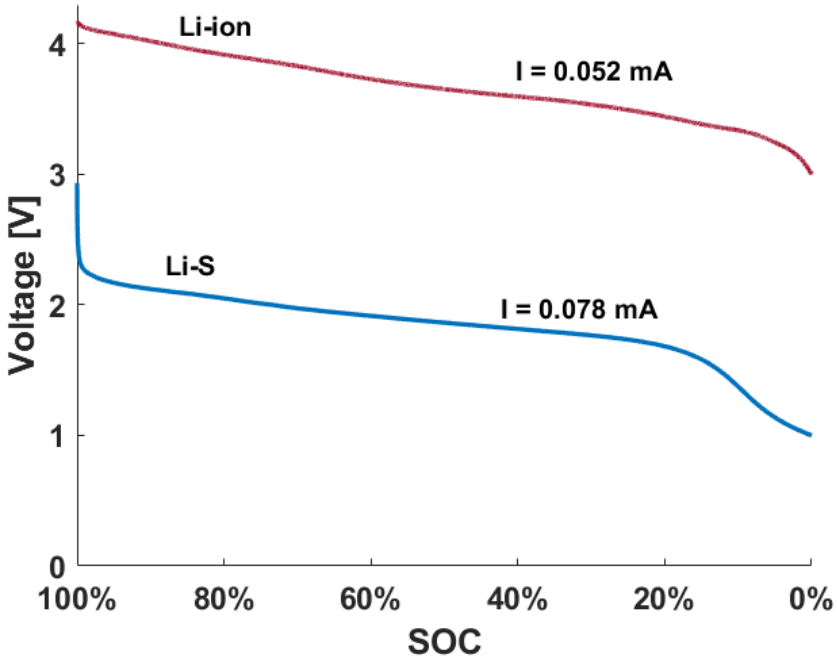

Figure 4.3: Voltage versus state of charge of a Li-S cell and a Li-ion cell for constant currents.

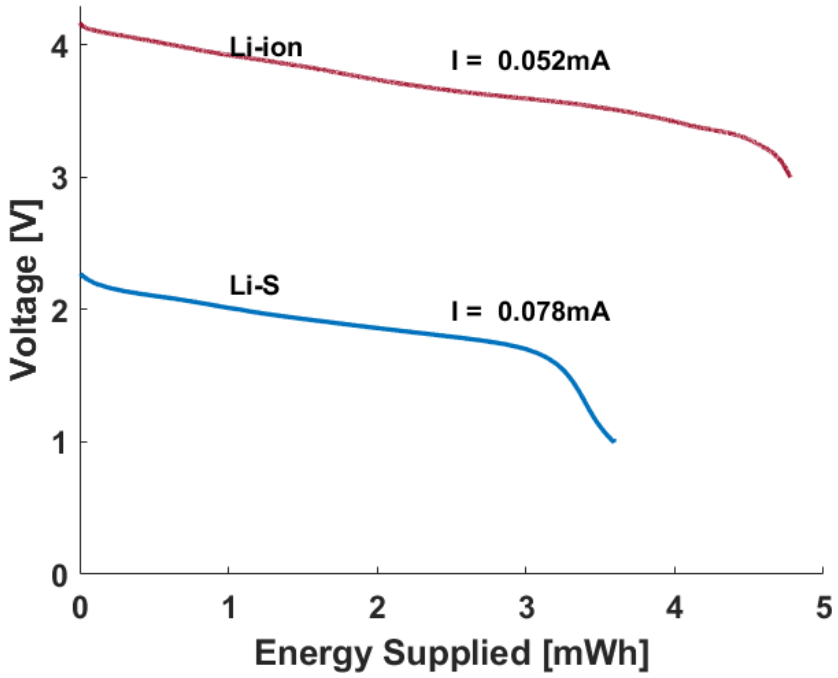

Figure 4.4: Voltage versus energy supplied by a Li-S and a Li-ion cell for constant currents. Maximum energy supplied is the energy capacity.

Figure 4.7 shows the voltage versus charge supplied of the Li-S cell at various constant currents. As expected, the lowest current has the highest charge capacity. Figure 4.8 shows the voltage versus SOC for the constant currents, and the corresponding data can be found in Table 4.4.

Figures 4.9 and 4.10 show the energy and power for these constant currents. The lowest C-Rate supplies the most energy, but the highest C-Rate supplies the most power. Table 4.5 shows the charge capacity, energy capacity, and power calculations for the operating currents of the Li-S cell, including the low current discussed in the previous section. Table 4.6 shows the specific charge capacity, specific energy capacity, and specific power for the same cell, obtained by dividing the values by the electrode mass of 3.9 mg. As the operating current increases, the discharge time decreases and so does the energy. However, the power increases. High C-Rates

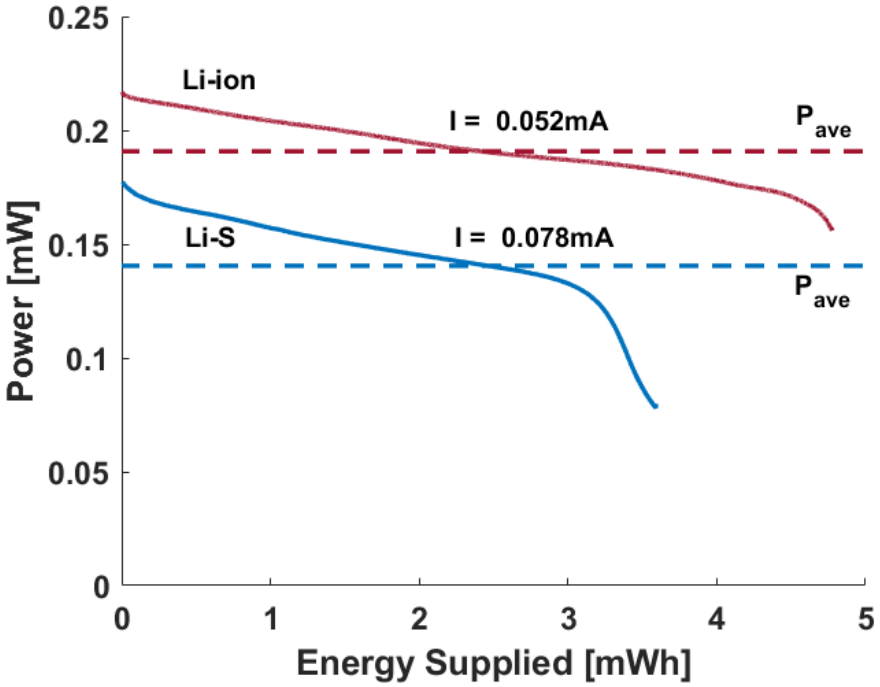

Figure 4.5: Instantaneous and average power versus energy supplied by a Li-S and a Li-ion cell for constant currents. Maximum energy supplied is the energy capacity.

correspond to high power. The charge capacity and energy capacity increase with a smaller current, while the power increases with a larger current.

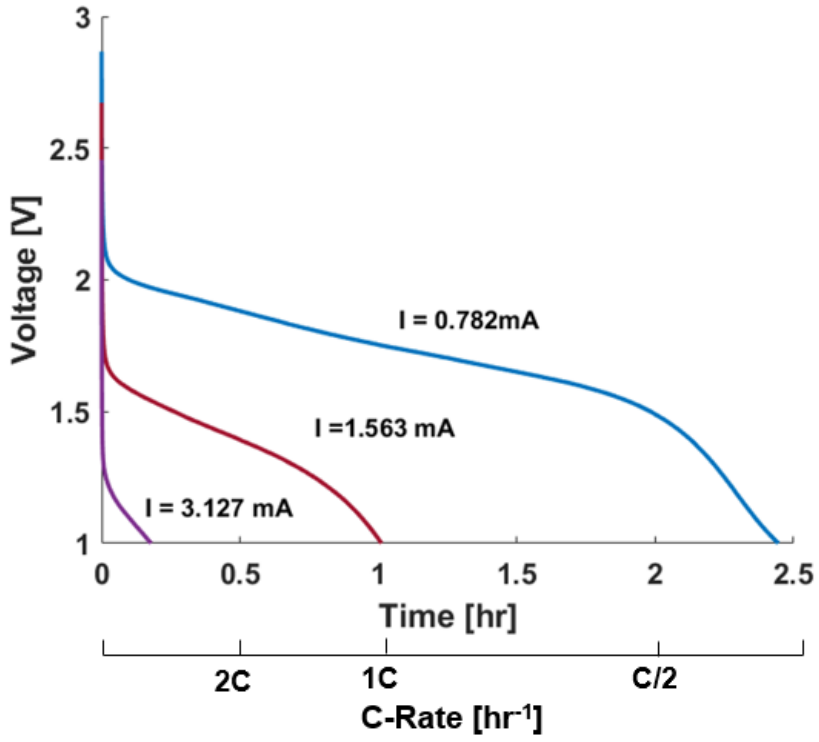

Figure 4.6: Voltage versus time of a Li-S cell for three constant currents: 3.127, 1.563, and 0.782 mA.

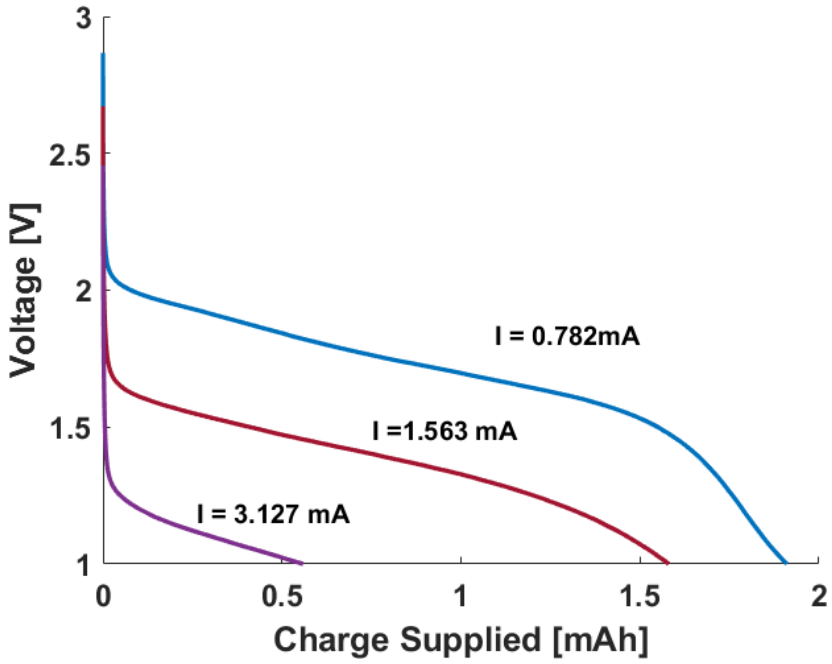

Figure 4.7: Voltage versus charge supplied of a Li-S cell for three constant currents: 3.127, 1.563, and 0.782 mA.

Table 4.4: SOC and voltage data for discharge of Li-S cell at various constant currents.

	Voltage [V]			
SOC [%]	**C/25**	**C/2**	**1C**	**2C**
100	2.923	2.872	2.567	2.456
97	2.821	2.595	2.418	2.267
95	2.745	2.493	2.345	2.198
92	2.599	2.366	2.284	2.15
90	2.497	2.308	2.247	2.146
87	2.354	2.241	2.196	2.111
85	2.293	2.197	2.164	2.100
82	2.206	2.165	2.113	2.061
79	2.160	2.123	2.089	2.042
77	2.140	2.113	2.075	2.033
74	2.115	2.082	2.048	2.025
72	2.101	2.072	2.007	2.019
69	2.082	2.051	2.007	1.993
67	2.067	2.041	1.995	1.976
64	2.045	2.021	1.969	1.963
62	2.029	2.011	1.957	1.94
59	2.005	2.000	1.944	1.935
56	1.982	1.99	1.932	1.191
54	1.969	1.98	1.908	1.893
51	1.951	1.96	1.896	1.885
49	1.940	1.95	1.884	1.862
46	1.921	1.94	1.873	1.842
44	1.911	1.93	1.862	1.839
41	1.895	1.92	1.85	1.818
38	1.880	1.899	1.839	1.802
36	1.870	1.889	1.828	1.796
33	1.855	1.879	1.806	1.775
31	1.845	1.869	1.802	1.772
28	1.830	1.849	1.785	1.756
26	1.821	1.839	1.774	1.756
23	1.807	1.819	1.764	1.736
21	1.798	1.808	1.753	1.718
18	1.784	1.788	1.733	1.700
15	1.767	1.768	1.722	1.666
13	1.755	1.758	1.712	1.649
10	1.736	1.748	1.692	1.633
8	1.719	1.728	1.682	1.602
5	1.686	1.707	1.651	1.557
3	1.656	1.677	1.621	1.502
0	1.000	1.000	1.000	1.000

Table 4.5: Charge, energy, power, and C-Rate for Li-S discharge curves at various constant currents.

Current mA	**Time** hr	**C-Rate** hr^{-1}	**Q** mAh	**E** mWh	$\mathbf{P_{ave}}$ mW
0.078	25	0.04	1.98	3.59	0.14
0.782	2.4	0.4	1.88	3.08	1.27
1.563	1.0	1.0	1.563	2.07	2.07
3.127	0.18	5.6	0.532	0.608	3.44

Table 4.6: Specific charge, specific energy, and specific power for Li-S discharge curves at various constant currents.

Current mA	**Time** hr	**C-Rate** hr^{-1}	$\mathbf{Q_{Specific}}$ mAh/g	$\mathbf{E_{Specific}}$ mWh/g	$\mathbf{P_{ave,\ Specific}}$ mW/g
0.078	25	0.04	507	921	35.9
0.782	2.4	0.4	482	790	326
1.563	1.0	1.0	401	530	530
3.127	0.18	5.6	136	156	882

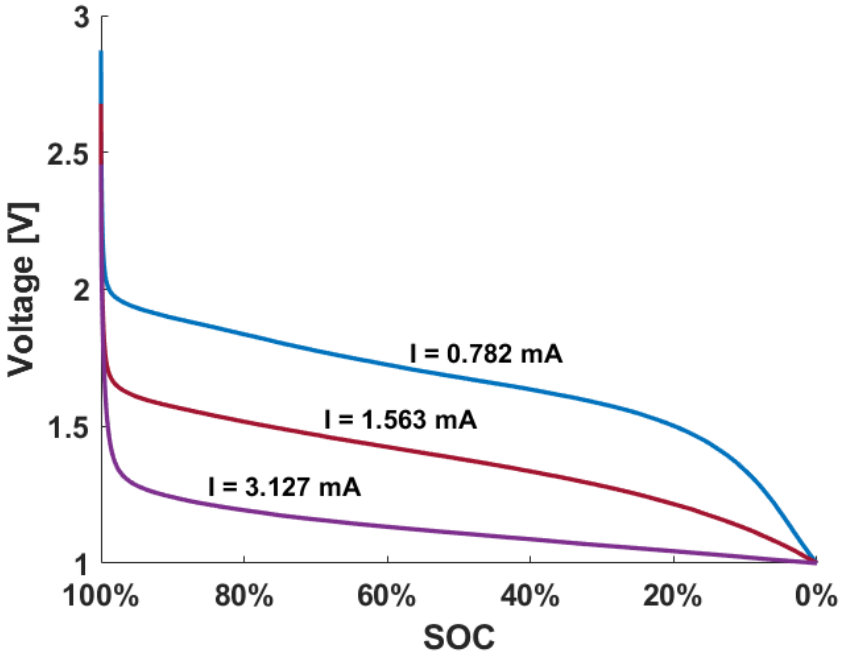

Figure 4.8: Voltage versus SOC of a Li-S cell for three constant currents: 3.127, 1.563, and 0.782 mA.

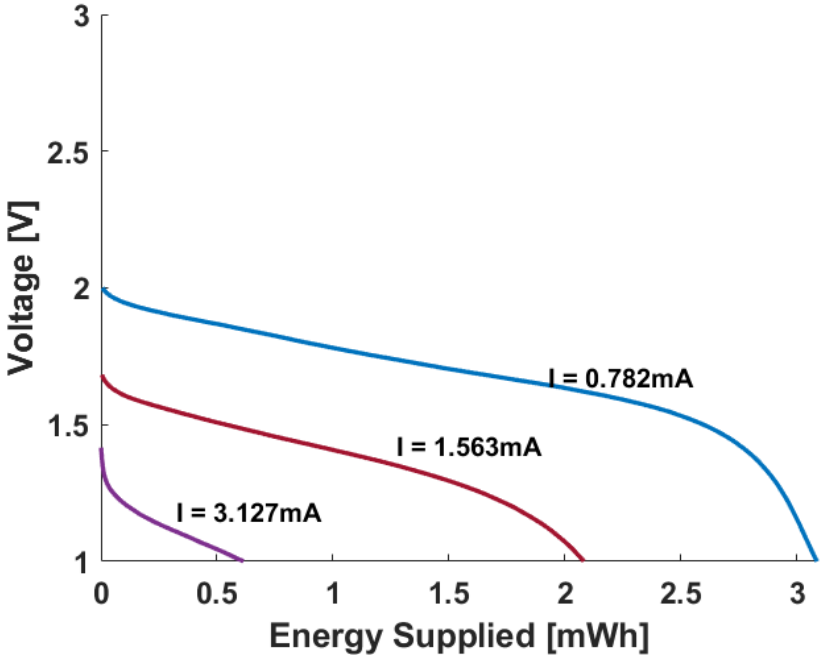

Figure 4.9: Voltage versus energy supplied by a Li-S cell for three constant currents: 3.127, 1.563, and 0.782 mA.

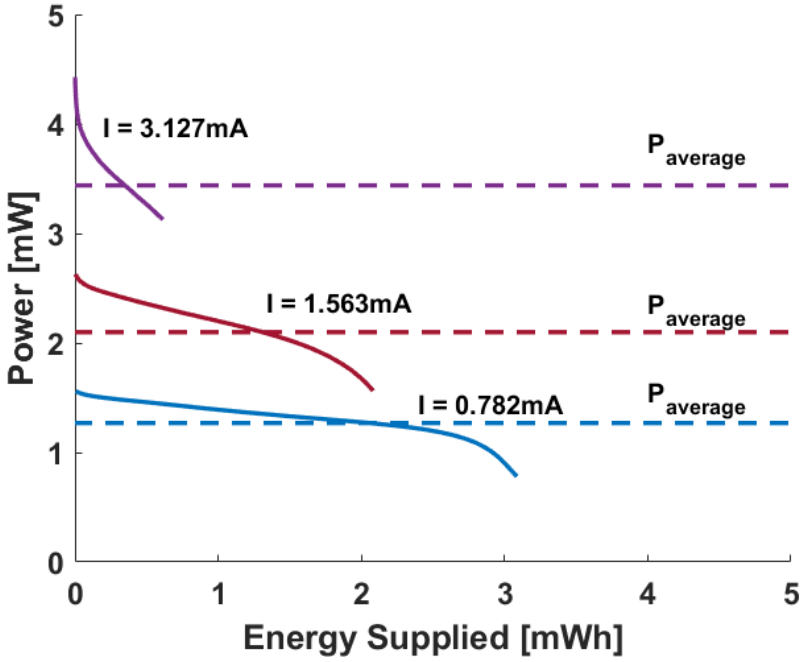

Figure 4.10: Power versus energy supplied by a Li-S cell for three constant currents: 3.127, 1.563, and 0.782 mA.

4.3 High C-Rates of Lithium-ion

Li-ion cells were also cycled at high C-Rates. Figure 4.11 shows the high C-Rate behavior of voltage versus time for the Li-ion cell. For the Li-ion cells, increasing the current does not drastically diminish the voltage.

Figure 4.12 shows the voltage versus charge supplied of the Li-ion cell at various constant currents. As expected, the lowest current has the highest charge capacity, but there is not a large difference for operation at constant currents of 0.65 mA to as high as 2.6 mA. Figure 4.13 shows the voltage versus SOC for the constant currents, and the corresponding data can be found in Table 4.7.

Figures 4.14 and 4.15 show the energy and power for these constant currents. The lowest C-Rate supplies the most energy, but the highest C-Rate supplies the most power. Table 4.8 shows the charge capacity, energy capacity, and power calculations for the operating currents of the Li-ion cell, including the low current discussed in the previous section. Table 4.9 shows the specific charge capacity, specific energy capacity, and specific power for the same cell, obtained by dividing the values by the electrode mass of 9.4 mg. Similarly to Li-S, the charge capacity and energy capacity increase with a smaller current, while the power increases with a larger current.

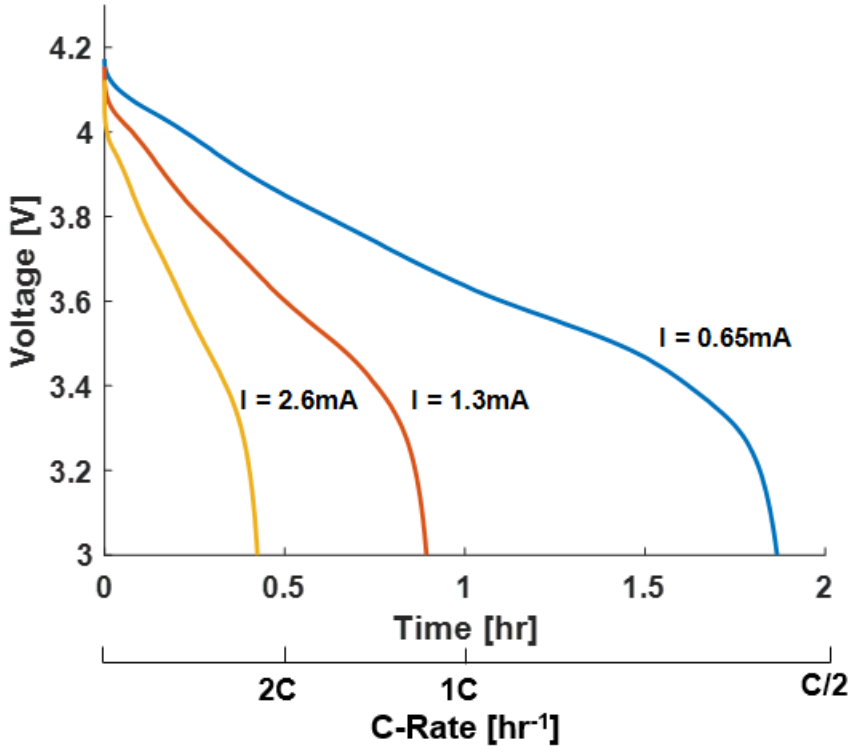

Figure 4.11: Voltage versus time of a Li-ion cell for three constant currents: 2.6, 1.3, and 0.65 mA.

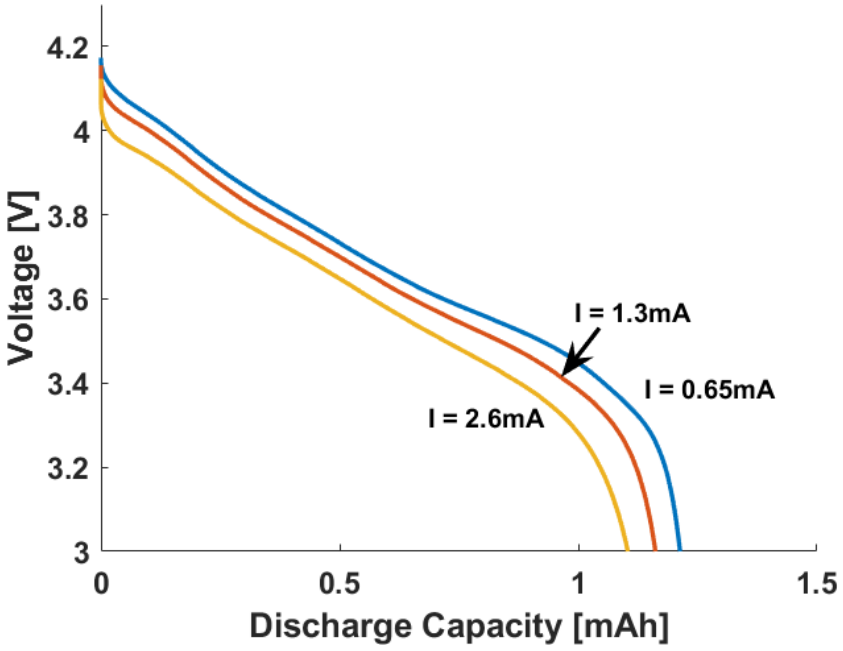

Figure 4.12: Voltage versus charge supplied of a Li-ion cell for three constant currents: 2.6, 1.3, and 0.65 mA.

Table 4.7: SOC and voltage data for discharge of a Li-ion cell at various constant currents.

	Voltage [V]			
SOC [%]	**C/25**	**C/2**	**1C**	**2C**
100	4.173	4.1714	4.155	4.123
97	4.095	3.97	3.939	3.928
95	4.070	3.889	3.888	3.878
92	4.038	3.838	3.827	3.817
90	4.015	3.808	3.797	3.786
87	3.981	3.768	3.767	3.745
85	3.960	3.748	3.747	3.725
82	3.931	3.717	3.716	3.695
79	3.904	3.697	3.696	3.674
77	3.887	3.677	3.676	3.654
74	3.861	3.657	3.656	3.634
72	3.843	3.647	3.646	3.624
69	3.814	3.626	3.625	3.603
67	3.793	3.616	3.605	3.583
64	3.762	3.596	3.595	3.563
62	3.743	3.586	3.575	3.553
59	3.716	3.566	3.556	3.532
56	3.692	3.556	3.534	3.512
54	3.677	3.535	3.524	3.491
51	3.656	3.515	3.504	3.471
49	3.643	3.505	3.484	3.461
46	3.625	3.475	3.464	3.431
44	3.614	3.465	3.444	3.42
41	3.598	3.434	3.424	3.39
38	3.583	3.414	3.403	3.37
36	3.572	3.394	3.383	3.359
33	3.553	3.374	3.363	3.339
31	3.538	3.353	3.322	3.319
28	3.515	3.333	3.322	3.299
26	3.498	3.313	3.312	3.288
23	3.469	3.283	3.282	3.258
21	3.448	3.273	3.262	3.248
18	3.414	3.232	3.231	3.218
15	3.379	3.202	3.200	3.187
13	3.360	3.182	3.180	3.166
10	3.332	3.151	3.149	3.146
8	3.302	3.131	3.139	3.136
5	3.231	3.100	3.108	3.115
3	3.167	3.079	3.088	3.095
0	3.0	3.0	3.0	3.0

Table 4.8: Charge, energy, power, and C-Rate for Li-ion discharge curves at various constant currents.

Current mA	**Time** hr	**C-Rate** hr^{-1}	**Q** mAh	**E** mWh	$\mathbf{P_{ave}}$ mW
0.052	25	0.04	1.300	4.771	0.1908
0.65	1.8	0.54	1.212	4.303	2.313
1.3	0.89	1.1	1.161	4.160	4.656
2.6	0.42	2.4	1.103	3.952	9.348

Table 4.9: Specific charge, specific energy, and specific power for Li-ion discharge curves at various constant currents.

Current mA	**Time** hr	**C-Rate** hr^{-1}	$\mathbf{Q_{Specific}}$ mAh/g	$\mathbf{E_{Specific}}$ mWh/g	$\mathbf{P_{ave,\ Specific}}$ mW/g
0.052	25	0.04	138	508	20.3
0.65	1.8	0.54	129	458	246
1.3	0.89	1.1	124	442	495
2.6	0.42	2.4	117	420	994

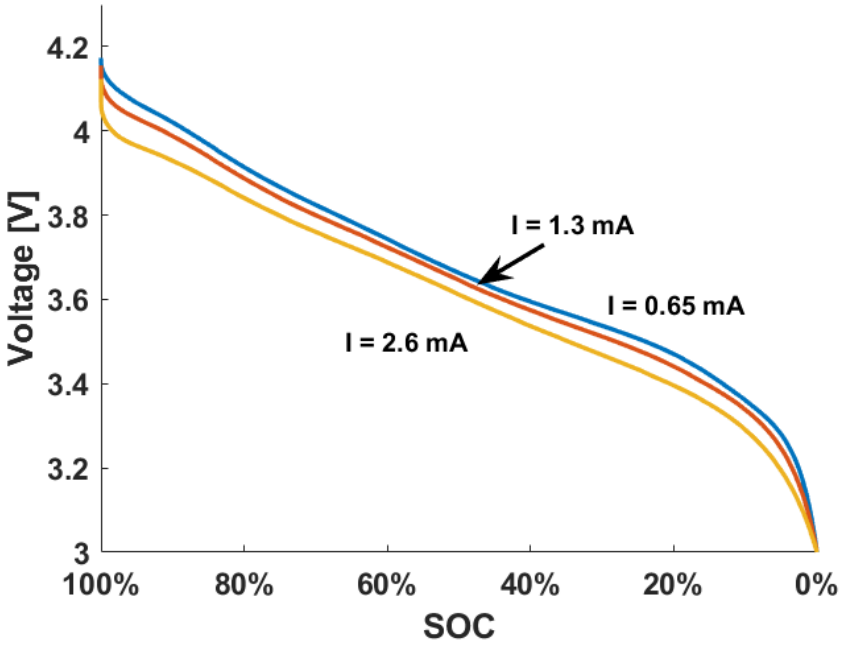

Figure 4.13: Voltage versus SOC of a Li-ion cell for three constant currents: 2.6, 1.3, and 0.65 mA.

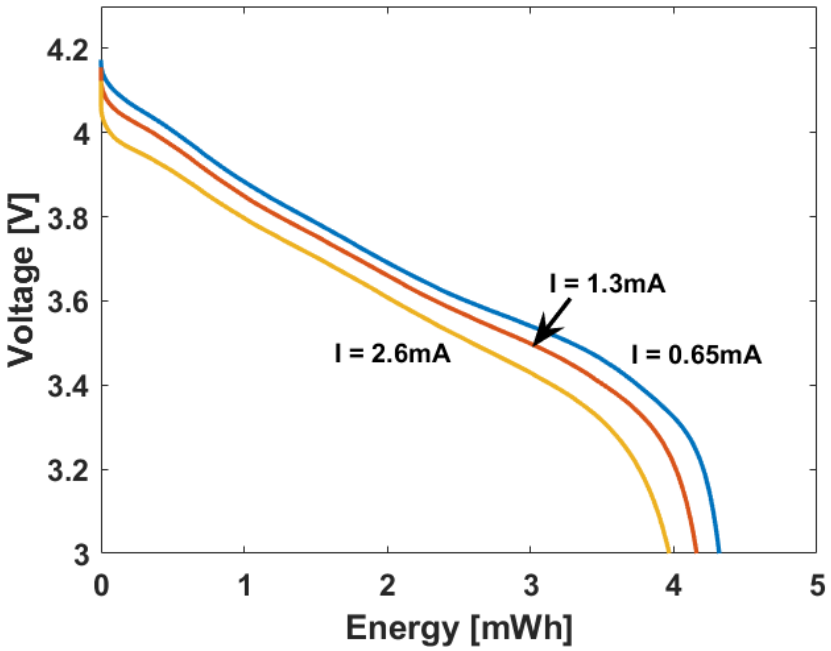

Figure 4.14: Voltage versus energy supplied by a Li-ion cell for three constant currents: 2.6, 1.3, and 0.65 mA.

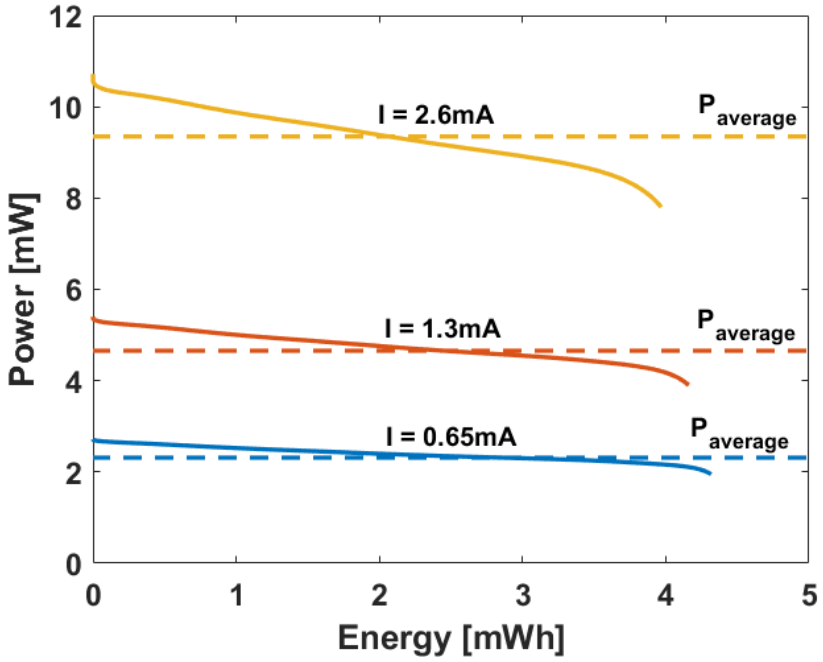

Figure 4.15: Power versus energy supplied by a Li-ion cell for three constant currents: 2.6, 1.3, and 0.65 mA.

4.4 Ragone Plot

To obtain the specific energy and specific power of the Li-S and Li-ion cells, the energy and power are divided by the electrode mass. The electrode mass of the Li-S cell is 3.9 mg. The electrode mass of the Li-ion cell is 9.4 mg. Note that this is allows for a consistent comparison between the Li-ion and Li-S cells as the overhead is identical.

Figure 4.16a shows the Ragone plot of specific power versus specific energy. Data for the Li-S and Li-ion cells can be found in Tables 4.10 and 4.11, respectively. Dashed diagonal lines represent different C-Rates. At the lower C-Rates, Li-S has almost twice the specific energy of Li-ion. At 1C they cross over yet the Li-S specific energy is still slightly higher. At C-Rates above 1C, the specific energy drops rapidly, and above 4C it essentially vanishes for Li-S. Note that at the highest C-Rate shown for Li-S, the C-Rate is unrealistically high as the high current draw of 4.7 mA caused high internal resistance and the cell discharged in only 10 seconds. This is not a feasible operating C-Rate for Li-S, as the battery would be spent far too quickly.

The results in the Ragone plot are of great import to eVTOL design. Twice the energy means either dramatic expansion of range or dramatic reduction in gross weight. A limitation of C-Rate means that expansion of range is the preferred solution. Thus, this has significant implications even on vertiport infrastructure.

Trendlines for the data in Figure 4.16a are shown in Fig. 4.16b. The trendlines are in Eqs. (4.8) and (4.9), respectively, where P is in W/kg and E in Wh/kg. Note that mW/g and mWh/g are the same as W/kg and Wh/kg, respectively. Equations (4.8) and (4.9) can be written in terms of C-Rate and energy which is better suited for aircraft design purposes. In this form, the proposed models for Li-S and Li-ion are Eqs. (4.10) and (4.11), respectively, where E is in

Table 4.10: Specific energy and power of Li-S cells at various C-Rates.

C-Rate [hr^{-1}]	**Specific Energy [Wh/kg]**	**Specific Power [W/kg]**
0.04	921	35.9
0.10	913	68.3
0.50	800	329
1.0	530	530
5.6	156	882
347	3.03	1,102

Table 4.11: Specific energy and power of Li-ion cells at various C-Rates.

C-Rate [hr^{-1}]	**Specific Energy [Wh/kg]**	**Specific Power [W/kg]**
0.04	508	20.3
0.10	500	50.0
0.54	458	246
1.1	442	495
2.4	420	994
6.6	351	2,320

Wh/kg and C-Rate in hr^{-1}.

$$P = -1.1E + 1,096 \tag{4.8}$$

$$P = -14E + 6,984 \tag{4.9}$$

$$E = \frac{1,096}{\text{C-Rate} + 1.1} \tag{4.10}$$

$$E = \frac{6,984}{\text{C-Rate} + 14} \tag{4.11}$$

Note that these models use the weight of the electrodes only, not the entire coin cell. This is

appropriate as it is uncontaminated with the construction type of the cell - coin, pouch, prismatic, etc. The construction adds overhead. The coin cell overhead is inherently exorbitant due to its small size and layers of encapsulation. It is recommended that these values are divided by an overhead factor of 2.0, and then further divided by a packing factor of 1.6 to reach installed numbers on the aircraft [7].

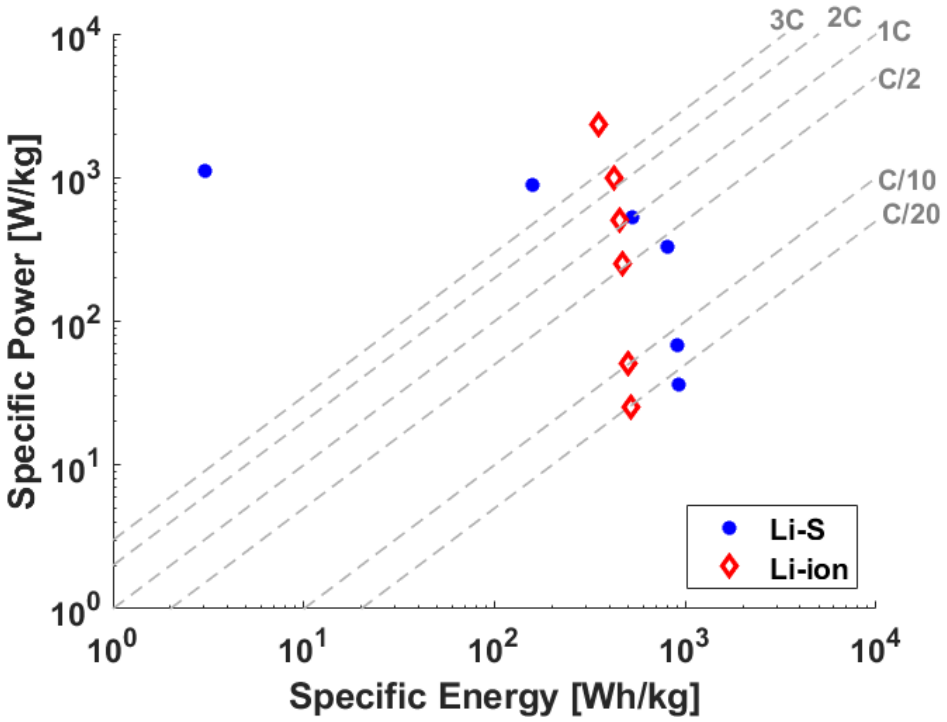

(a) Ragone plot of Li-S and Li-ion cells. Specific power and energy are calculated using weight of the electrodes.

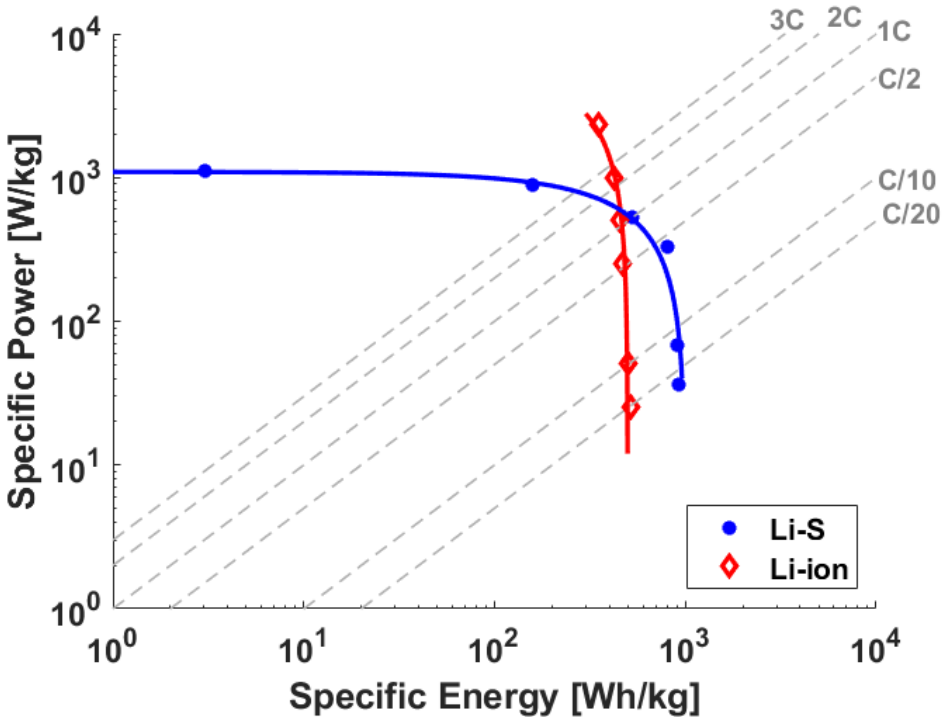

(b) Ragone plot of Li-S and Li-ion cells with fitted trendlines.

Figure 4.16: Ragone plot of Li-S and Li-ion cells.

4.5 Cycle Life

Li-S and Li-ion cells were tested to determine the impact of cycle life on charge and energy capacity. One cycle is one charge and one discharge. Figure 4.17 shows the voltage versus SOC for one cycle of a Li-ion cell cycling at C/25. Cycle life is the number of charge and discharge cycles a cell can achieve before the charge capacity falls below 80% of its initial charge capacity.

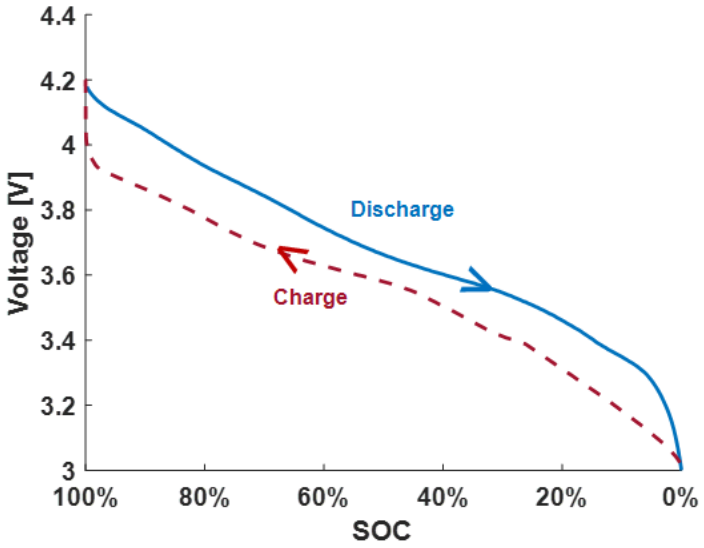

Figure 4.17: Voltage versus SOC for charge and discharge of a Li-ion cell, current of C/25.

The Li-S and Li-ion cells were cycled at 1C. Figure 4.18a shows the measured specific charge capacities for the first 100 cycles. The Li-S cells have a high specific charge capacity, but it steadily decreases with cycles. The Li-ion cells have a lower specific charge capacity, but are stable and do not decrease in charge capacity at all. Note that the capacity drop after the first two cycles is due to the formation of the SEI layer, a phenomenon that is common to both Li-S and Li-ion chemistries but is dramatic for Li-S. This SEI layer formation and the resulting loss of capacity after the first two cycles account for the gap between the theoretical and measured specific charge capacities.

Figure 4.18b shows the specific energy capacities. The Li-S specific energy capacity is initially significantly higher than that of the Li-ion cell, with mean values of 675 and 450 Wh/kg respectively. However after 100 cycles the specific energy capacities are more comparable, with mean values of 533 and 450 Wh/kg respectively. Note that this is seen when operating at a C-Rate of 1C. As shown in the Ragone plot in Figure 4.16a, Li-S specific energy can be twice that of Li-ion at C/2 and half that of Li-ion at 2C. The gradual loss in cycle life is important for eVTOL operations, as the decrease in energy capacity will decrease the range of the aircraft.

4.6 Half Cycles

The charging bottleneck and the fact that batteries are dead weight, whether full or empty, may favor fractional cycles for regulated missions with immediate recharge at stopover destinations. Tests were conducted where the cells were discharged only halfway, referred to as half cycles. The results in Figure 4.19a show the specific energy capacity per cycle versus cycle number for Li-S, with the y-axis enlarged in Figure 4.19b to provide a clear view of the relative stability in specific energy capacity. The results in Figure 4.20a show the specific energy capacity per cycle versus cycle number for Li-ion, with the y-axis enlarged in Figure 4.20b to provide a clear view of the relative stability in specific energy capacity. The results demonstrate that the half cycles improve the energy of the Li-S cells, and also seem to mitigate the cycle instability issue seen in the full cycle discharge. This energy increase and stability gain in Li-S cells would have a significant beneficial effect on eVTOL aircraft, as the higher specific energy would allow for a lighter battery pack for a specified mission. The stability of energy capacity would solve the issue of range decreasing with cycle count. Furthermore, intracity eVTOL aircraft will likely be

operating at half cycles (or other fractional cycles), as each flight can be controlled to not drain the battery fully. The battery would be able to recharge often.

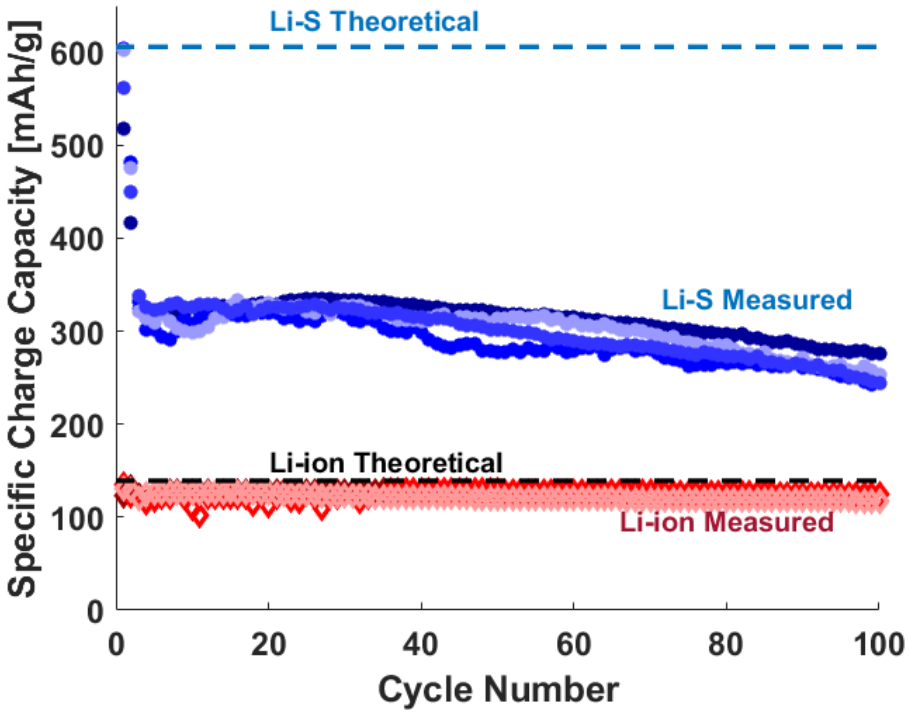

(a) Specific charge capacity.

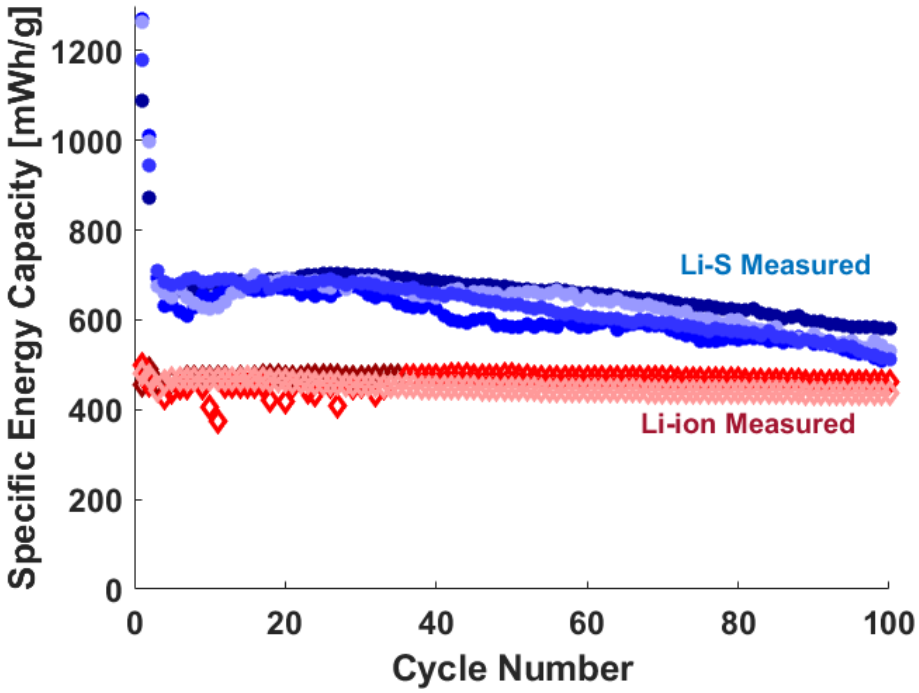

(b) Specific energy capacity.

Figure 4.18: Li-S and Li-ion specific charge and energy capacities versus cycle number, current of 1C. Different shades of blue and red reflect data from 4 different Li-S and Li-ion cells, respectively.

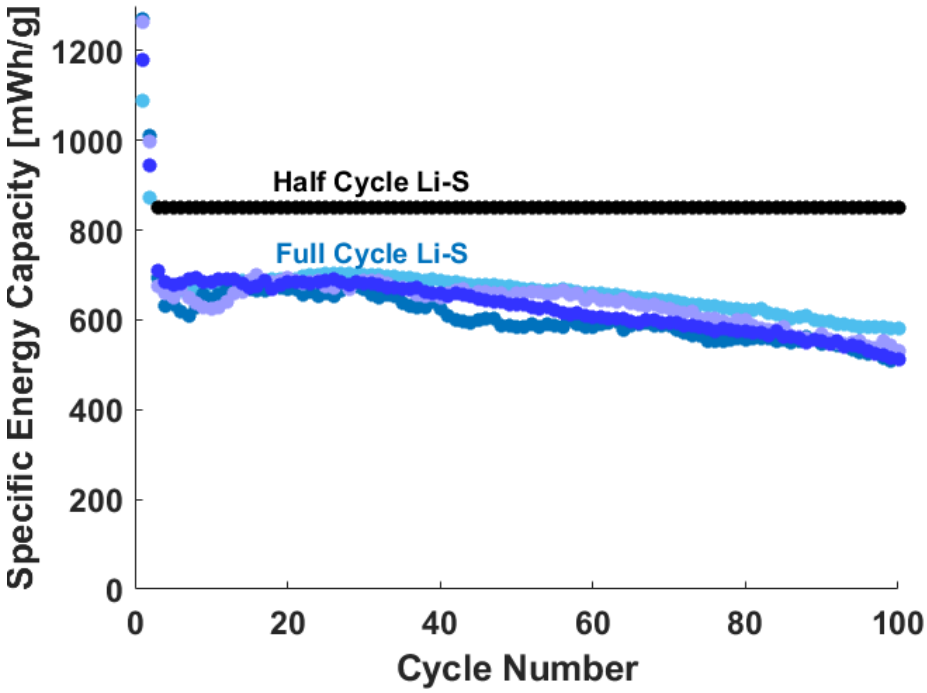

(a) Li-S half cycles vs full cycles.

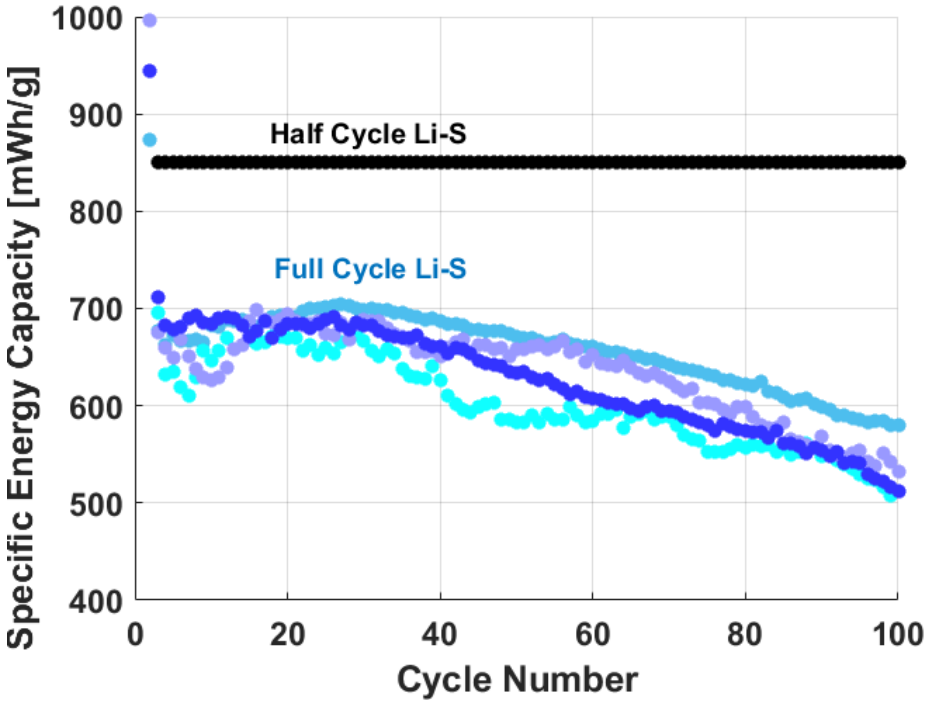

(b) Zoomed in perspective.

Figure 4.19: Impact of half cycles on Li-S, specific energy capacity vs cycle number. Different shades of blue reflect data from 4 different Li-S cells.

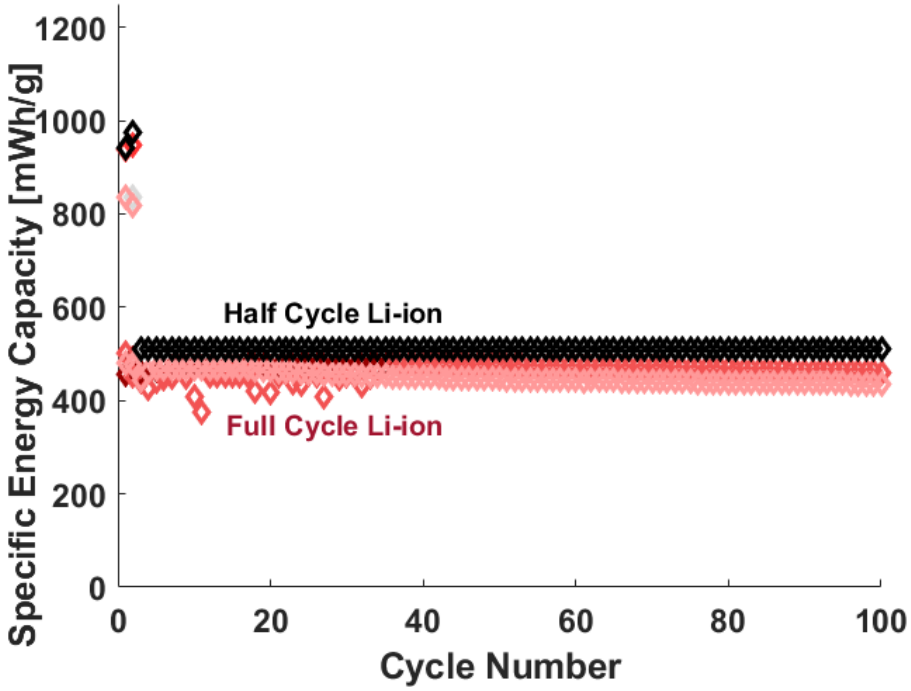

(a) Li-ion half cycles vs full cycles.

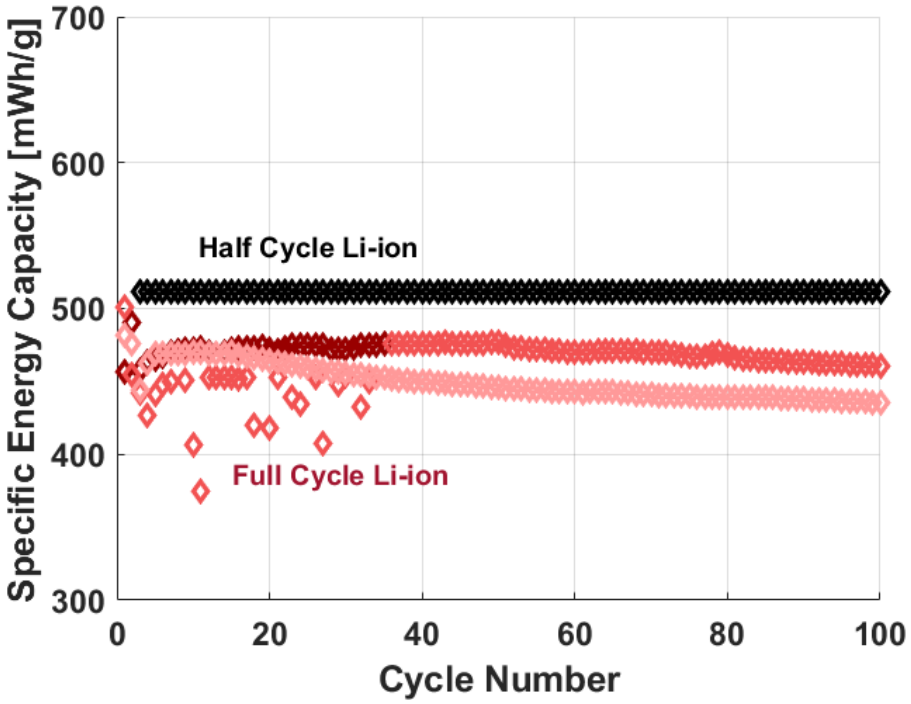

(b) Zoomed in perspective.

Figure 4.20: Impact of half cycles on Li-ion, specific energy capacity vs cycle number. Different shades of red reflect data from 4 different Li-ion cells.

4.7 Modeling

For a constant current draw, the voltage can be predicted by the classic Shepherd model [44]. The Shepherd model is the simplest of circuits, given by Equation (4.12), where V is the output cell potential in volts, E_r is an open circuit voltage in volts, R is the internal resistance times unit area, and i is current density in Amps per unit area. The area is defined as the area of the cathode; here the area is 0.97cm^2. The term Ri accounts for the voltage drop due to internal resistance.

$$V = E_r - Ri \tag{4.12}$$

The crux of the model is E_r, the open circuit voltage. It is modeled using Equation (4.13), where E_s is a constant potential in volts, Q is the charge capacity per area, t is time elapsed, and i is current density. The term $K\frac{Q}{Q-it}i$ accounts for the resistance as lithium ions diffuse through the electrolyte. The term $Ae^{\frac{-B}{Q}it}$ accounts for the voltage drop due to the charge transfer resistance, which is the voltage drop over the electrode-electrolyte interface.

In total, there are five constants that are measured empirically: E_s, K, A, B, and R. K is in units of $\Omega\cdot$ cm^2, A in volts, B is unitless, and R is in $\Omega\cdot$cm^2.

$$E_r = E_s - K\frac{Q}{Q-it}i + Ae^{\frac{-B}{Q}it} \tag{4.13}$$

The factor $(Q-it)/Q$ is $(1-DOD)$, defined earlier as SOC in Eq. (4.6). The factor (it/Q) is DOD, defined earlier in Eq. (4.7). So the Shepherd model gives the open circuit voltage E_r as a function of SOC as in Eq. (4.14), or as a function of DOD as in Eq. (4.15).

$$E_r = E_s - K\frac{i}{SOC} + Ae^{-B(1-SOC)} \tag{4.14}$$

$$E_r = E_s - K\frac{i}{1-DOD} + Ae^{-B(DOD)} \tag{4.15}$$

The Shepherd model is a crude fit to the data, but is based on underlying phenomena. The open circuit voltage cannot be easily measured, so the voltage measured at the lowest current can be approximated as the open circuit voltage. The constants E_s and K are extracted from this data. The constants A and B are determined empirically.

R is extracted from the jump in voltage at $SOC = 1$, with change in current. Note that at $SOC = 1$ (i.e., $DOD = 0$ or time $t = 0$), the jump in voltage ΔV with a change in current Δi is $\Delta V = (K + R)\Delta i$. It is easier to determine $(K + R)$ first, then R, to get good fits at higher currents.

Figure 4.21a shows the discharge curves of voltage versus time for a Li-S cell cycling at three C-Rates: C/25, C/2, and 1C. The data are represented as symbols and the model as lines. Figure 4.21b shows the discharge curves of voltage versus time for a Li-ion cell cycling at same three C-Rates: C/25, C/2, and 1C. The data are represented as symbols and the model as lines. Model parameters for the Li-S and Li-ion models are found in Table 4.12. Overall, Li-S parameters show a higher resistance compared to Li-ion.

Table 4.12: Constants used for the Shepherd model for Li-S and Li-ion discharge curves.

Parameter	**Units**	**Li-S**	**Li-ion**
$\mathbf{E_s}$	V	1.40	3.70
K	$\Omega \cdot \text{cm}^2$	45.0	5.0
A	V	0.80	0.45
B		1.0	4.0
R	$\Omega \cdot \text{cm}^2$	150.5	1.50

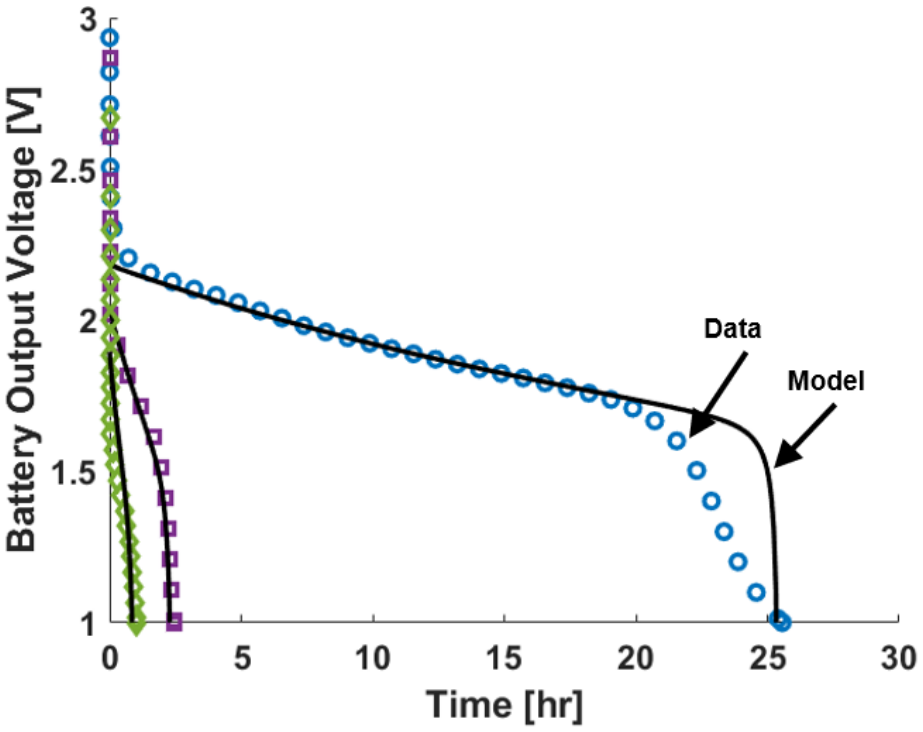

(a) Li-S.

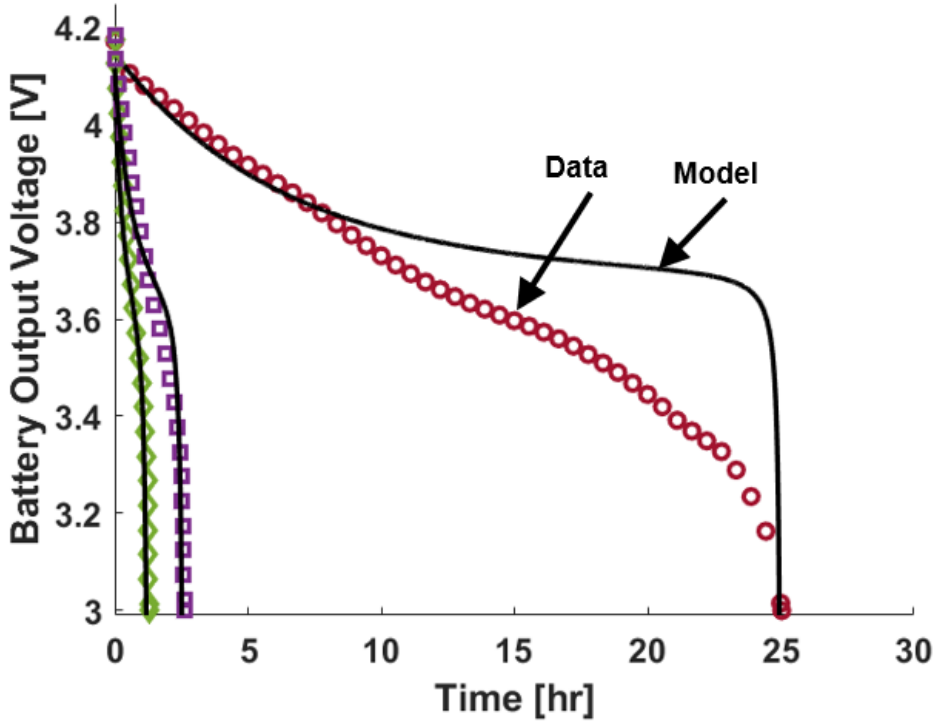

(b) Li-ion.

Figure 4.21: Shepherd model applied to discharge voltage versus time data of Li-S and Li-ion coin cells, cycled at various C-Rates.

4.8 Summary

Steady state testing was performed on Li-S and Li-ion coin cells. Measured specific charge capacities for these cells were compared to the theoretical values. The discharge characteristics were collected for a range of C-Rates, which allowed for the construction of a Ragone Plot of specific power versus specific energy. The cycle life was investigated, and the impact of half cycles was determined. Modeling of the steady state behavior was performed using the Shepherd model. The following key conclusions can be made.

1. Measured specific charge capacity of the Li-ion cells at a current of 1C was 127 Ah/kg and remained steady with cycles. Li-S cells was 401 Ah/kg at a current of 1C. The measured charge capacity of the fabricated cells match well with the theoretical prediction.

2. SEI layer formation appeared to be a major problem in the Li-S cells, leading to a high loss in charge and energy capacity during its formation in the first 1-2 cycles.

3. The measured specific energy capacity after the first 2 full discharge cycles of the Li-ion cells was 460 Wh/kg, and that of the Li-S cells was 533 Wh/kg, both at a C-Rate of 1C.

4. For C-Rates up to C/2, Li-S has twice the specific energy of Li-ion. Around 1C see they crossover but thereafter Li-S drops rapidly. By 4C, the specific energy for LiS almost vanishes. These numbers, if valid, upon scale-up have dramatic import on eVTOL and infrastructure. It favors a dramatic expansion of range of eVTOL over a reduction in gross weight.

5. The cycle life of Li-S is poor, but only when it is fully discharged. If only half cycles are

allowed, the loss in capacity is almost eliminated. Operating at half cycles results in higher Li-S energy output compared to that of Li-ion, and more importantly stabilizes the Li-S cells where there is no decrease in specific energy capacity at least for the first 100 cycles.

6. The Shepherd model can predict the behavior of voltage in response to a steady current. However the dynamic behavior is more complicated than what can be modeled by an open circuit voltage and a resistor. Model parameters were chosen for best fit at C/2 and adequate fit at higher and lower C-Rates. Overall, Li-S modeling showed that Li-S cells have a higher internal resistance than Li-ion.

With steady state analysis and modeling complete, attention turned to transient behavior.

Chapter 5: Transient Data and Modeling

Transient operations are crucial for eVTOL, as various in-flight maneuvers such as take-off, ascent, hover, and turns require varying amounts of power. Power is equal to rotor speed times torque. The speed is controlled by the voltage, and the torque determines the current.

Transient data under varying current is collected for the Li-S and Li-ion cells. First, Electrochemical Impedance Spectroscopy (EIS) data is collected and analyzed. An Equivalent Circuit Model (ECM) is developed based on the impedance data. The model is then converted from the frequency domain to the time domain. Voltage response of Li-S and Li-ion cells to step and pulse currents are collected, and the model in the time domain is applied to the data.

5.1 Electrochemical Impedance Theory

In EIS, a sinusoidal current is drawn and the corresponding voltage measured. The impedance Z is equal to voltage/current as in Eq. (5.1). With a sinusoidal current input of $I = I_0 sin(\omega t)$, the measured voltage response can be split into sine and cosine components as seen in Eq. (5.2). Eq. (5.1) then becomes Eq. (5.3), where the impedance is split into an in-phase voltage response and an out of phase voltage response.

$$\text{Impedance} = Z = \frac{V_{out}}{I_0} \tag{5.1}$$

$$V_{out} = v_s sin(\omega t) + v_c cos(\omega t) \tag{5.2}$$

$$Z = \frac{v_s sin(\omega t)}{I_0} + \frac{v_c cos(\omega t)}{I_0} \tag{5.3}$$

To find the output voltage, an ECM can be developed as seen in Figure 5.1, where the circuit model varies for different types of batteries.

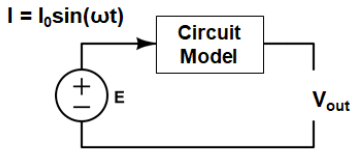

Figure 5.1: Battery Internal Circuit

The components of the ECM affect the impedance of the model. Consider an ECM that is simply a resistor as in Figure 5.2a. The impedance would be simply equal to the value of that resistor as seen in Eq. (5.4), shown in Figure 5.2b. Impedance is plotted with the frequency of the sinusoid as a parameter. This is essentially a Nyquist plot, as it is a frequency response plot. The in-phase voltage response to unit current, Z_{real}, is plotted on the x-axis and the out of phase, Z_{imag}, on the y-axis. Z_{real} is v_s/I_0 and Z_{imag} is v_c/I_0. The y-axis is inverted, so negative values are plotted.

$$Z = \frac{V}{I_0} = \frac{RI_0}{I_0} = R \tag{5.4}$$

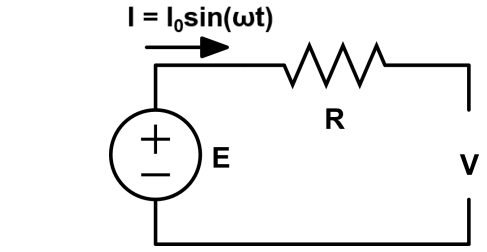

(a)

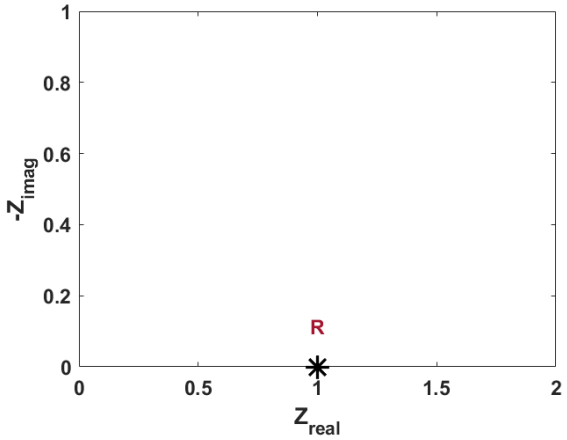

(b)

Figure 5.2: a) Single resistor model and b) Impedance Nyquist plot for single resistor model.

If the ECM is a Resistor-Capacitor (R//C) block as in Figure 5.3a, the impedance would take the shape of a semi-circle as seen in Figure 5.3b. The value of the resistor is the diameter of the semi-circle. The capacitance can be found by $C = (Rf^*)^{-1}$, where f^* is the frequency at the highest point of the semi-circle. To find the impedance expression for this circuit, the following procedure is followed. The impedance of a capacitor is Eq. (5.5), where C is the capacitance of the capacitor in Farad, ω is the frequency, and $i = \sqrt{-1}$. The impedance of this R//C circuit is found in Eq. (5.6). Separating this equation into real and imaginary terms gives Eq. (5.7).

$$Z_C = \frac{1}{i\omega C} \tag{5.5}$$

$$Z = \frac{1}{\frac{1}{Z_R} + \frac{1}{Z_C}} = \frac{1}{\frac{1}{R} + \frac{1}{(i\omega C)^{-1}}} = \frac{1}{\frac{1}{R} + i\omega C} \tag{5.6}$$

$$Z = \frac{R}{1 + (R\omega C)^2} + i\frac{-\omega RC}{1 + (R\omega C)^2} = Z_{real} + iZ_{imag} \tag{5.7}$$

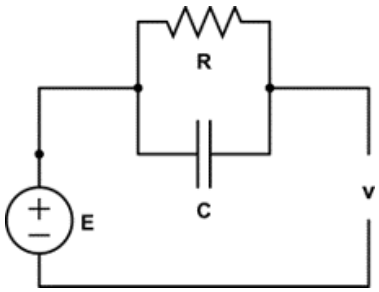

(a)

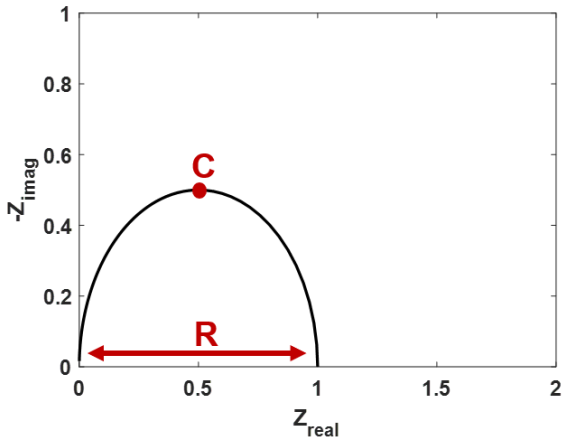

(b)

Figure 5.3: a) R//C-block model and b) Impedance plot for R//C-block model.

Adding a resistor in series with the R//C block, seen in Figure 5.4a, shifts the semi-circle to the right by the value of the additional resistor, as seen in Figure 5.4b. The impedance equation for this circuit is Eq. (5.8). When split into real and imaginary components, the equation becomes Eq. 5.9.

$$Z = Z_{R_0} + \frac{1}{\frac{1}{Z_{R_1}} + \frac{1}{Z_C}} = R_0 + \frac{1}{\frac{1}{R_1} + i\omega C_1} \tag{5.8}$$

$$Z = R_0 + \frac{R_1}{1 + (R_1 \omega C_1)^2} - i \frac{\omega C_1 R_1^2}{1 + (R_1 \omega C_1)^2} \tag{5.9}$$

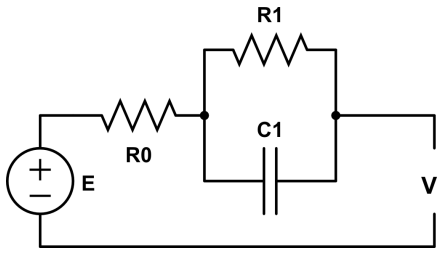

(a)

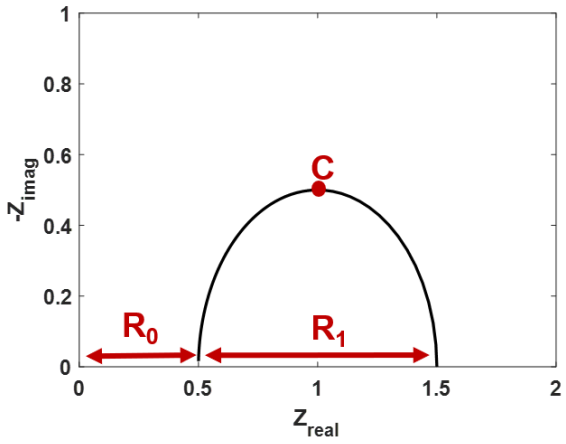

(b)

Figure 5.4: a) R_0-R//C-block model and b) Impedance plot for this model.

Adding an additional component called the Warburg element, the circuit becomes Figure 5.5a. In Nyquist plots, it is seen as a 45° line in the low frequency region, as in Figure 5.5b. The impedance equation for this circuit is Eq. (5.10). Z_w is defined by Eq. (5.11), where σ is the Warburg coefficient in $\Omega/\sqrt{s}$. The Warburg element has a strong influence at low frequencies (0.01 - 1.0 Hz scale), and is used to account for resistance due to diffusion. This low frequency region is important for eVTOL as it covers the typical rotor frequency range. The Warburg element is named after Emil Warburg, and was first developed in oncology research by his son Otto Warburg in the early 1930s [45].

$$Z = Z_{R_0} + \frac{1}{\frac{1}{Z_{R_1}+Z_w} + \frac{1}{Z_{C_1}}} = \frac{1}{\frac{1}{R_1+Z_W} + i\omega C_1} \tag{5.10}$$

$$Z_w = \sigma\omega^{-1/2}(1-i) \tag{5.11}$$

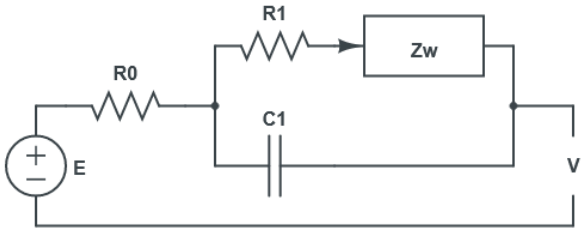

(a)

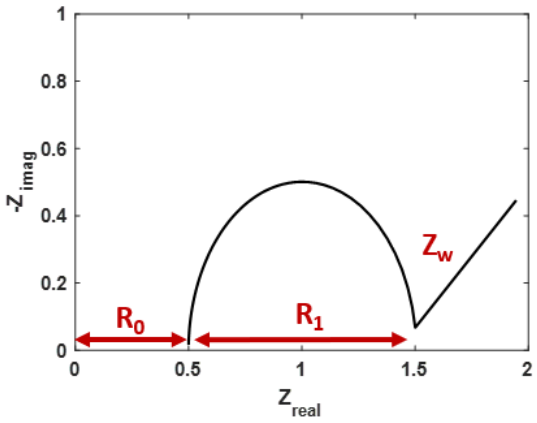

(b)

Figure 5.5: a) R_0-(R_1-W)//C-block and b) Impedance plot for this model.

Consider the R_0-R_1//C_1 circuit shown in Figure 5.4a. The output voltage can be solved for using the following method. The voltage equation is shown in Eq. (5.12), where I is the current over R_0 and I_1 is the current over R_1. Let I be equal to Eq. (5.13). Let I_1 and consequently $\dot{I}_1$ be equal to the expressions in Eq. (5.14). An expression for $\dot{I}_1$ as a function of total current I can

also be found using a current balance, as seen in Eq. (5.15).

$$V = E - R_0 I - R_1 I_1 \tag{5.12}$$

$$I = I_0 sin(\omega t) \tag{5.13}$$

$$\begin{aligned} I_1 = &\quad a cos(\omega t) + b sin(\omega t) \\ \dot{I}_1 = &\quad -a\omega sin(\omega t) + b\omega cos(\omega t) \end{aligned} \tag{5.14}$$

$$\begin{aligned} I = &\quad I_{R1} + I_{C1} \\ I = &\quad I_{R1} + C_1 \dot{v_{C1}} \\ I = &\quad I_{R1} + C_1 \dot{I_{R1}} R_1 \\ \frac{1}{R_1 C_1} I = &\quad \dot{I}_1 + \frac{1}{R_1 C_1} I_1 \end{aligned} \tag{5.15}$$

Substituting Eqs. (5.13) and (5.14) into Eq. (5.15) gives the expression in Eq. (5.16). Comparing the coefficients of the sine and cosine terms gives Eqs. (5.17) and (5.18) respectively. Solving this system of equations gives expressions for a and b, seen in Eqs. (5.19) and (5.20) respectively.

$$\frac{I_0 sin(\omega t)}{R_1 C_1} = -a\omega sin(\omega t) + b\omega cos(\omega t) + \frac{1}{R_1 C_1} a cos(\omega t) + \frac{1}{R_1 C_1} b sin(\omega t) \tag{5.16}$$

$$\frac{I_0}{R_1 C_1} = -a\omega + \frac{b}{R_1 C_1} \tag{5.17}$$

$$0 = b\omega + \frac{a}{R_1 C_1} \tag{5.18}$$

$$a = -\frac{\omega I_0 R_1 C_1}{(\omega R_1 C_1)^2 + 1} \tag{5.19}$$

$$b = \frac{I_0}{(\omega R_1 C_1)^2 + 1} \tag{5.20}$$

The output voltage can now be determined as in Eq. (5.21). Splitting this into cosine and sine components gives expressions for v_c and v_s, seen in Eqs. (5.22) and (5.23) respectively.

$$V = E - R_0 I_0 sin(\omega t) - R_1 \left[-\frac{\omega I_0 R_1 C_1}{(\omega R_1 C_1)^2 + 1} cos(\omega t) + \frac{I_0}{(\omega R_1 C_1)^2 + 1} sin(\omega t) \right] \tag{5.21}$$

$$v_c = \frac{\omega R_1^2 I_0 C_1}{(\omega R_1 C_1)^2 + 1} \tag{5.22}$$

$$v_s = -R_0 I_0 - \frac{R_1 I_0}{(\omega R_1 C_1)^2 + 1} \tag{5.23}$$

5.2 Electrochemical Impedance Measurement

EIS was used to measure cell impedance with a Solartron Analytical PARSTAT instrument, shown in Figure 5.6.

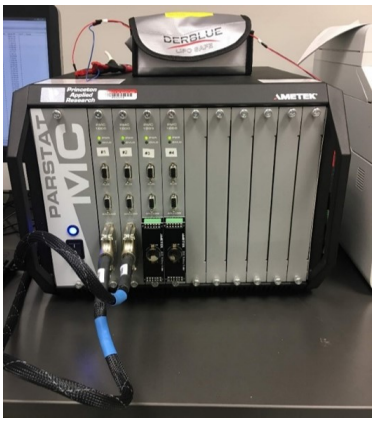

Figure 5.6: Solartron Analytical PARSTAT instrument used to collect transient data for coin cells.

A measured impedance test of a Li-S cell can be seen in Figure 5.7 and that of a Li-ion cell in Figure 5.8. The data are collected from high to low frequency, where each data point corresponds to a unique frequency. From these Figures, it is clear that not only is the Li-S cell impedance an order of magnitude higher than Li-ion, but it also is more affected by the low frequency Warburg region. In fact, it appears as though the Li-ion impedance for this frequency range contains no Warburg.

Impedance tests subject the cells to many full charge and discharge cycles. This stresses the cells and gradually changes their internal properties. Here, the data was collected when the cells reached 20 steady state cycles of charging and discharging at 1C.

5.3 Electrochemical Impedance Model

The impedance data gives insight to the internal aspects of the cell. The shape of the data helps to determine an ECM. Semi-circles in the data indicate the presence of R//C blocks. Position of the data on the x-axis indicates the value of the single resistor in series with the R//C blocks. A linear portion of the data in the low frequency range indicates the presence of a

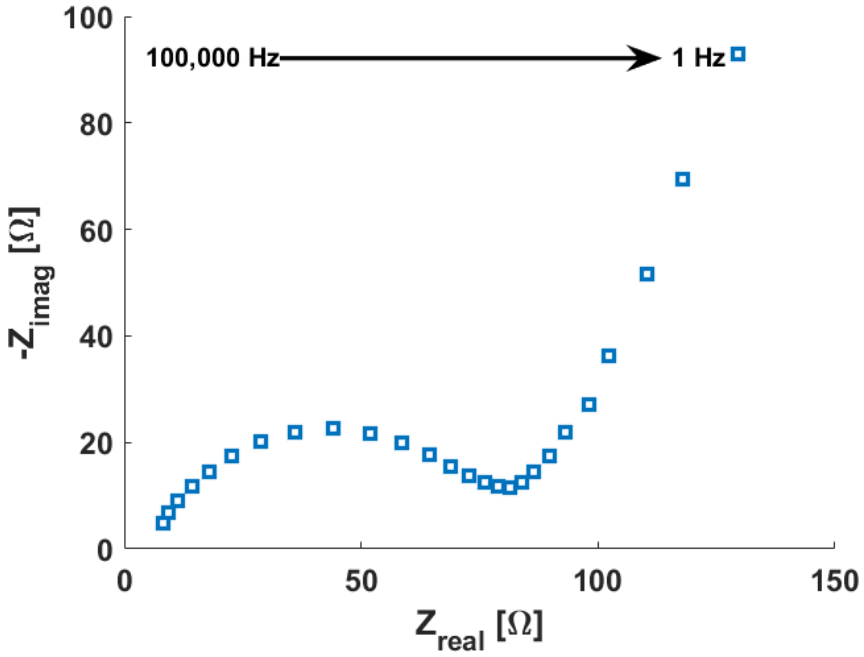

Figure 5.7: Li-S impedance data.

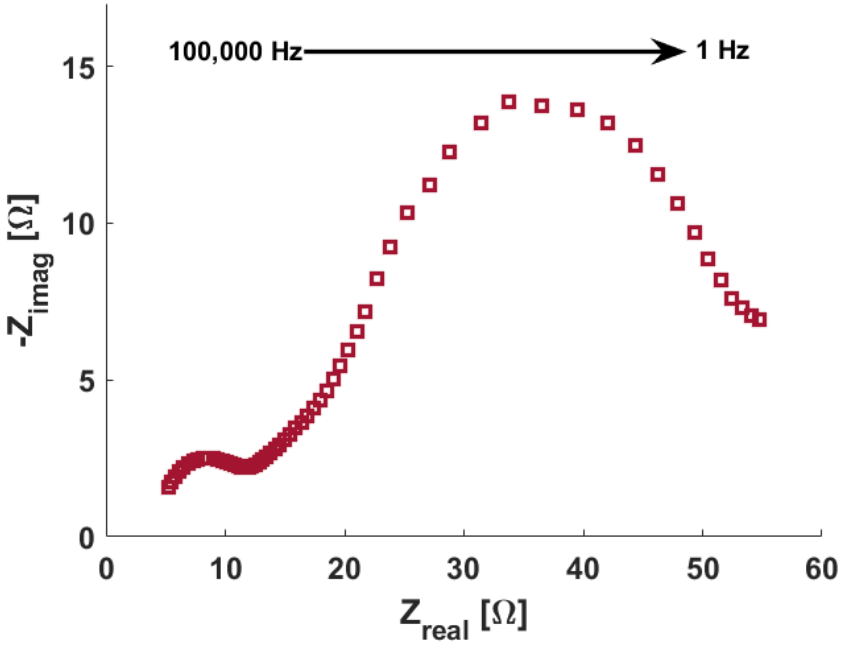

Figure 5.8: Li-ion impedance data.

Warburg element. Figure 5.9 shows the developed ECM for the Li-S cells. E is the open circuit voltage. The circuit consists of Resistor-Capacitor (R//C) blocks. The capacitor is in general

non-ideal and is represented as a Constant Phase Element (CPE). The impedance of a CPE can be calculated as in Eq. (5.24), where C is the capacitance in Farad and $0 \leq \alpha \leq 1$. If $\alpha = 1$, the CPE is an ideal capacitor. Additionally, a Warburg element, shown as Zw, is needed to represent the linear behavior of impedance at low frequencies. The low frequency region is important as it covers the typical rotor frequency range.

$$Z_{CPE} = \frac{1}{C(j\omega)^{\alpha}} \tag{5.24}$$

.

The utility of this model is that each component corresponds to a physical mechanism of the cell. The anode is represented by the first R_1//CPE_1 block, and represents the resistance due to mass and charge transfer over the electrode-electrolyte interface. The electrolyte and other component electronic resistances are represented by R_s. The cathode is represented by the R_{CT}//CPE_2 block, and represents the resistance due to ion transfer. The Warburg element is included in the cathode block and accounts for the resistance due to diffusion. This model was used to understand the impedance data.

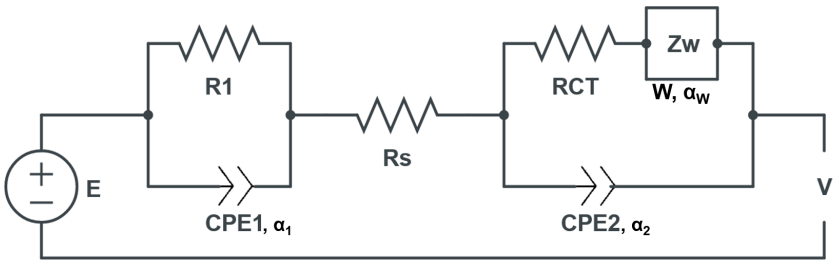

Figure 5.9: Equivalent circuit model developed for Li-S cells

5.4 Impedance versus Cycle Life

The impedance of Li-S and Li-ion are compared versus cycle life. With cycles, the cells degrade and the impedance analysis reveals why. The variation of impedance is seen in Figures 5.11 and 5.12 for Li-S and Li-ion respectively. Several cells were used for repeatability. Results from two cells are shown for each type of cell. Data is shown as points and the model as lines. Parameters extracted from the model provide insight into the changing physical mechanisms inside the cells. First, Li-S impedance is an order of magnitude greater than Li-ion. Second, the Li-S impedance increased with cycles, although was fairly stable up to 80 cycles. The Li-ion impedance also increased with cycles but more slowly.

The Li-S impedance is very different when compared to the Li-ion cells, both in magnitude and shape. Not only is the Li-S cell impedance an order of magnitude higher than Li-ion, but it also is more affected by the low frequency Warburg region. In fact, it appears as though the Li-ion impedance for this frequency range contains no Warburg, so a simpler ECM is used as seen in Figure 5.10. Table 5.1 shows the ECM parameters for the Li-S and Li-ion cells shown in Figures 5.11a and 5.12a, at 20 cycles and at over 100 cycles. The values demonstrate that the Li-S cells have consistently higher combined resistances, meaning that the internal cell resistance is much higher for Li-S compared to Li-ion.

Table 5.1: ECM parameters used to model Li-S and Li-ion impedance at 20 cycles and over 100 cycles.

		Li-S		Li-ion	
Parameter	**Units**	20 cycles	160 cycles	20 cycles	120 cycles
$\mathbf{R_s}$	Ω	6.2	31.0	4.5	5.2
$\mathbf{R_1}$	Ω	2.0	77.0	7.5	13.0
$\mathbf{CPE_1}$	Farad	$2.6 \cdot 10^{-9}$	$2.2 \cdot 10^{-6}$	$2.2 \cdot 10^{-5}$	$6.2 \cdot 10^{-4}$
α_1		1.0	0.85	0.75	0.5
$\mathbf{R_{CT}}$	Ω	84.0	93.0	44.0	64.0
$\mathbf{CPE_2}$	Farad	$9.5 \cdot 10^{-5}$	$6.5 \cdot 10^{-5}$	$1.01 \cdot 10^{-3}$	$4.1 \cdot 10^{-3}$
α_2		0.55	0.80	0.7	0.7
W	Farad	1.20	0.80	-	-
α_w		0.65	0.65	-	-

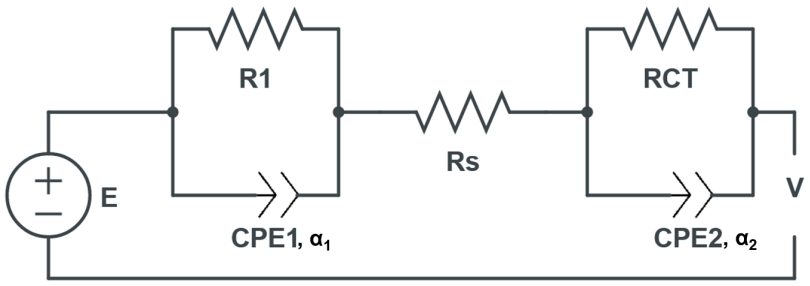

Figure 5.10: ECM developed for Li-ion cells.

Table 5.2: Impedance data for Li-S cell 1. All impedance measurements shown are in units of Ω.

Frequency	**20 cycles**		**40 cycles**		**60 cycles**		**80 cycles**		**160 cycles**	
[Hz]	$\mathbf{Z_{real}}$	$\mathbf{-Z_{imag}}$	$\mathbf{Z_{real}}$	$\mathbf{-Z_{imag}}$	$\mathbf{Z_{real}}$	$\mathbf{-Z_{imag}}$	$\mathbf{Z_{real}}$	$\mathbf{-Z_{imag}}$	$\mathbf{Z_{real}}$	$\mathbf{-Z_{imag}}$
100000	8.180	4.810	10.17	5.130	9.47	5.35	12.67	5.41	31.09	7.93
63095.74	9.380	6.760	11.53	7.070	10.92	7.390	14.01	7.35	32.74	10.47
39810.72	11.35	9.140	13.73	9.380	13.24	9.780	16.11	9.8	35.29	14.09
25118.87	14.21	11.78	16.92	11.76	16.61	12.21	19.22	12.59	39.46	18.74
15848.94	18	14.56	20.97	13.97	20.85	14.33	23.41	15.44	45.91	23.78
10000	22.81	17.42	25.80	15.88	25.72	16.10	28.72	18.12	54.67	28.06
6309.58	28.88	20.09	31.35	17.30	31.10	17.52	35.07	20.34	64.85	30.77
3981.07	36.16	21.99	37.42	17.94	36.98	18.48	42.3	21.7	75.42	31.97
2511.89	44.06	22.54	43.52	17.61	43.14	18.78	49.89	21.87	85.79	32.03
1584.89	51.80	21.66	49.18	16.48	49.22	18.41	57.16	20.87	95.63	31.38
1000	58.62	19.83	54.03	14.91	54.88	17.50	63.59	19.14	104.64	30.47
630.96	64.29	17.62	58	13.40	60.01	16.39	69.04	17.19	112.98	29.9
398.11	68.93	15.57	61.47	12.12	64.49	15.30	73.58	15.4	120.93	30.33
251.19	72.86	13.86	64.61	11.23	68.66	14.35	77.52	13.84	129.52	31.69
158.49	76.18	12.45	67.40	10.51	72.33	13.52	80.95	12.6	139.39	33.2
100	78.98	11.67	69.84	10.11	75.49	13.16	83.61	11.84	150.33	33.67
63.10	81.46	11.58	71.91	10.28	78.15	13.65	85.8	11.91	160.91	32.56
39.81	83.86	12.54	73.80	11.48	80.60	15.53	87.74	13.36	169.38	30.7
25.12	86.48	14.52	75.91	14.10	83.47	19.10	89.87	16.71	175.77	30.51
15.85	89.63	17.56	78.55	18.23	87.18	24.48	92.53	21.81	181.21	33.35
10	93.10	21.96	82.23	24.01	92.02	33	96.52	29.9	185.54	40.62
6.310	98.01	27.02	85.88	31.76	99.16	43.79	103.19	39.11	194.24	51.57
3.980	102.33	36.25	91.60	42.56	106.14	59.47	109.92	54.49	204.21	69.63
2.510	110.31	51.61	98.86	60.32	117.35	81.01	121.58	77.25	214.01	96.94
1.580	118	69.37	109.72	84.36	134.72	113.9	135.74	104.41	241.21	140.2
1	129.44	93.07	123.05	114.71	155.11	153.2	162	138.15	259.09	193.52

Table 5.3: Impedance data for Li-S cell 2. All impedance measurements shown are in units of Ω.

Frequency	**20 cycles**		**40 cycles**		**60 cycles**		**160 cycles**	
[Hz]	$\mathbf{Z_{real}}$	$\mathbf{-Z_{imag}}$	$\mathbf{Z_{real}}$	$\mathbf{-Z_{imag}}$	$\mathbf{Z_{real}}$	$\mathbf{-Z_{imag}}$	$\mathbf{Z_{real}}$	$\mathbf{-Z_{imag}}$
100000	12.99	4.51	22.34	4.79	11.79	4.56	27.59	7.33
63095.74	13.82	6.56	23.36	6.64	12.81	6.28	29.08	9.65
39810.72	15.24	9.44	25.08	9.16	14.37	8.57	31.22	12.99
25118.87	17.75	13.23	27.9	12.27	16.82	11.48	34.53	17.55
15848.94	21.77	17.75	32.1	15.56	20.45	14.82	39.72	23.27
10000	27.67	22.66	37.74	18.52	25.53	18.28	47.61	29.53
6309.58	35.65	27.35	44.58	20.61	32.16	21.32	58.4	35.12
3981.07	45.6	31.1	52.15	21.4	40.06	23.24	71.41	38.89
2511.89	56.96	33.16	59.56	20.8	48.51	23.58	85.32	40.19
1584.89	68.66	33.22	66.2	19.19	56.52	22.38	98.63	39.29
1000	79.73	31.52	71.74	17.16	63.43	20.3	110.33	37.37
630.96	89.56	28.75	76.37	15.25	69.12	17.95	120.18	35.81
398.11	97.78	25.36	80.2	13.67	73.84	15.91	129.66	35.59
251.19	104.6	21.89	83.71	12.53	77.88	14.16	139.47	36.67
158.49	110.1	18.7	86.96	11.55	81.37	12.69	150.74	38.27
100	114.28	16.17	89.67	10.81	84.13	11.64	163.32	38.68
63.1	117.62	14.66	91.92	10.57	86.44	11.4	175.6	37.11
39.81	120.41	14.29	93.8	11.34	88.28	12.29	185.18	34.74
25.12	123.21	15.33	95.85	13.24	90.36	14.71	192.55	34.1
15.85	126.19	17.4	98.32	16.98	92.81	19	198.29	37.01
10	129.74	21.56	101.35	21.84	96.59	25.65	204.88	43.29
6.31	133.6	26.44	105.96	30.78	102.02	34.14	213.74	57.52
3.98	138.28	35.7	111.92	41.78	108.45	46.18	225.61	76.47
2.51	147.14	49.45	116.27	58.35	116.6	64.97	241.59	99.62
1.58	152.62	65.84	130.57	79.49	128.4	89.67	255.85	142.46
1	168.2	87.41	142.05	119.8	149.07	122.19	285.93	184.25

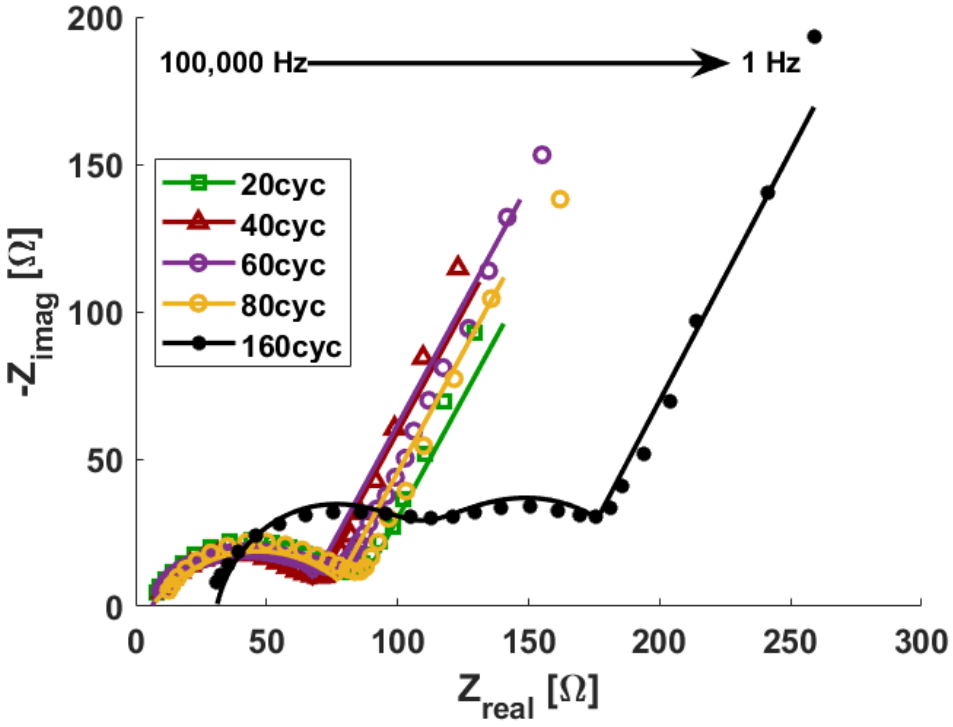

(a) Cell 1.

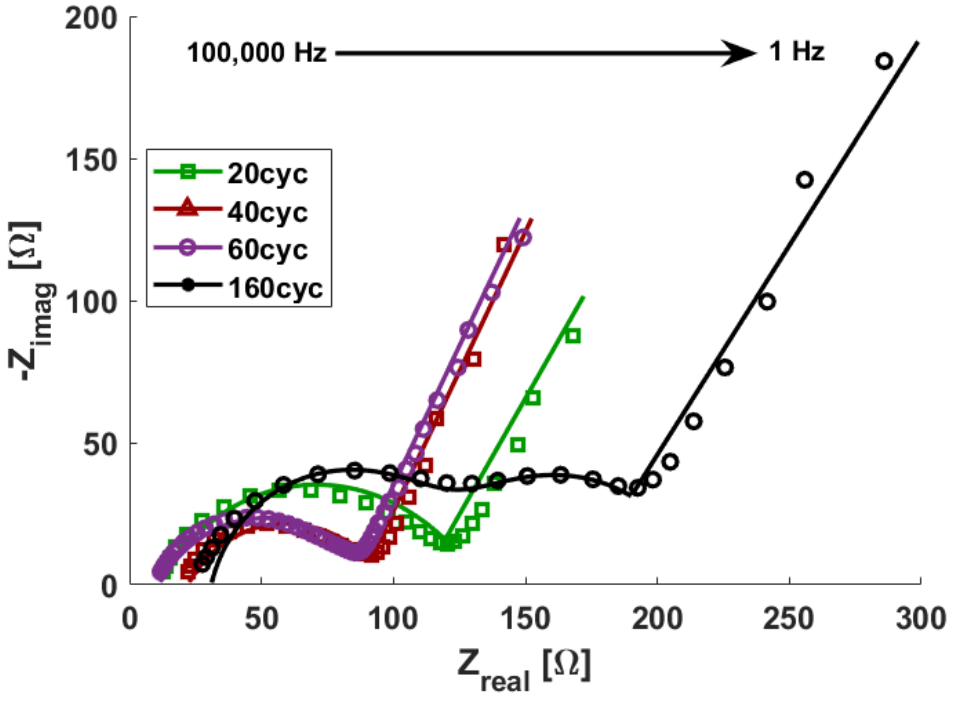

(b) Cell 2.

Figure 5.11: Impedance for Li-S cells as cycle count increases, points are data and lines are models.

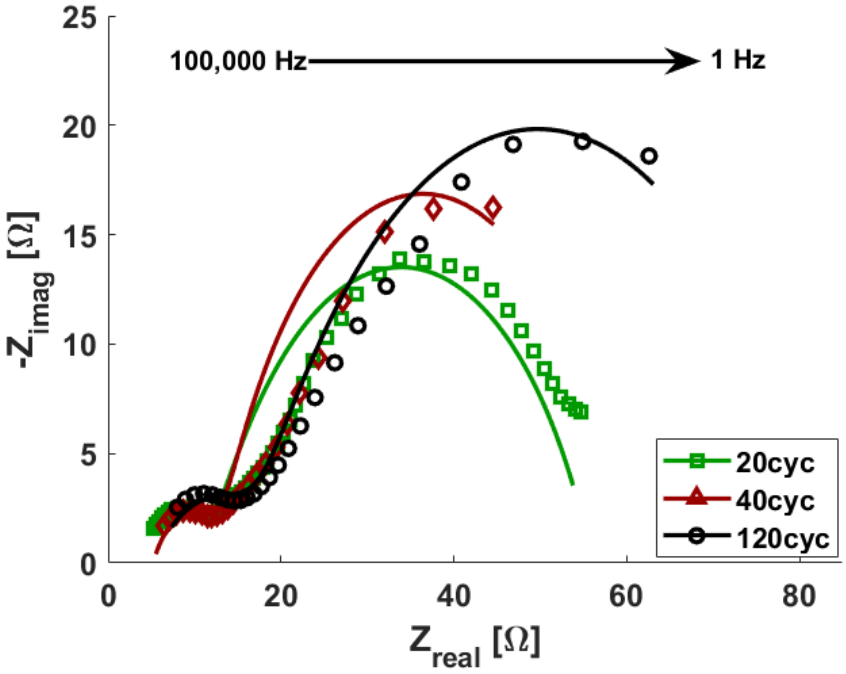

(a) Cell 1.

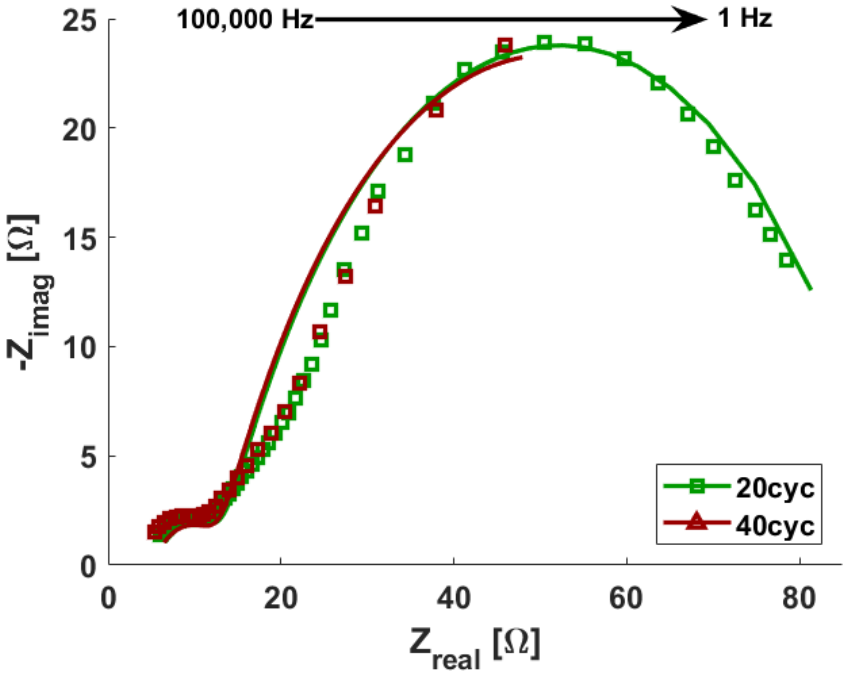

(b) Cell 2.

Figure 5.12: Impedance for Li-ion cells as cycle count increases, points are data and lines are models.

Table 5.4: Impedance data for Li-ion cell 1. All impedance measurements shown are in units of Ω.

Frequency	**20 cycles**		**40 cycles**		**120 cycles**	
[Hz]	$\mathbf{Z_{real}}$	$\mathbf{-Z_{imag}}$	$\mathbf{Z_{real}}$	$\mathbf{-Z_{imag}}$	$\mathbf{Z_{real}}$	$\mathbf{-Z_{imag}}$
100000	5.24	1.56	6.02	1.36	7.3	2.12
63095.74	5.81	1.92	6.50	1.70	8.04	2.55
39810.72	6.51	2.22	7.12	2.01	8.95	2.90
25118.87	7.30	2.41	7.84	2.24	10.00	3.11
15848.94	8.14	2.50	8.63	2.36	11.06	3.17
10000	8.96	2.50	9.42	2.38	12.07	3.11
6309.58	9.73	2.42	10.17	2.33	12.99	2.99
3981.07	10.43	2.31	10.84	2.24	13.83	2.89
2511.89	11.06	2.24	11.46	2.17	14.59	2.83
1584.89	11.65	2.21	12.03	2.15	15.33	2.86
1000	12.23	2.25	12.60	2.20	16.08	2.98
630.96	12.82	2.36	13.19	2.31	16.88	3.16
398.11	13.47	2.56	13.8	2.51	17.74	3.49
251.19	14.18	2.80	14.49	2.78	18.66	3.90
158.49	14.99	3.10	15.27	3.11	19.68	4.47
100	15.88	3.46	16.14	3.50	20.85	5.24
63.1	16.85	3.87	17.12	3.98	22.25	6.26
39.81	17.90	4.36	18.21	4.56	23.93	7.56
25.12	19.03	5.03	19.43	5.31	26.23	9.15
15.85	20.30	5.95	20.76	6.35	28.91	10.84
10	21.74	7.19	22.19	7.78	32.18	12.65
6.31	23.78	9.23	24.4	9.39	36.05	14.57
3.98	27.07	11.2	27.18	12.00	40.88	17.41
2.51	31.42	13.21	31.97	15.16	46.86	19.12
1.58	36.57	13.76	37.67	16.16	54.9	19.26
1	41.99	13.20	44.56	16.27	62.60	18.60

Table 5.5: Impedance data for Li-ion cell 2. All impedance measurements shown are in units of Ω.

Frequency	**20 cycles**		**40 cycles**	
[Hz]	$\mathbf{Z_{real}}$	$\mathbf{-Z_{imag}}$	$\mathbf{Z_{real}}$	$\mathbf{-Z_{imag}}$
100000	5.78	1.28	4.95	1.23
63095.74	6.23	1.52	5.38	1.51
39810.72	6.76	1.72	5.91	1.77
25118.87	7.34	1.87	6.52	1.98
15848.94	7.95	1.98	7.18	2.13
10000	8.60	2.05	7.89	2.22
6309.58	9.23	2.07	8.60	2.25
3981.07	9.83	2.07	9.28	2.24
2511.89	10.41	2.08	9.92	2.22
1584.89	10.97	2.13	10.52	2.23
1000	11.53	2.24	11.11	2.31
630.96	12.13	2.43	11.73	2.46
398.11	12.78	2.71	12.38	2.71
251.19	13.53	3.07	13.12	3.04
158.49	14.4	3.52	13.96	3.46
100	15.42	4.03	14.93	3.97
63.1	16.6	4.61	16.08	4.58
39.81	17.91	5.27	17.37	5.27
25.12	19.37	6.02	18.81	6.05
15.85	20.90	6.98	20.41	7.00
10	22.68	8.45	22.16	8.34
6.31	24.64	10.31	24.48	10.65
3.98	27.24	13.54	27.4	13.21
2.51	31.22	17.10	30.92	16.44
1.58	37.64	21.15	37.9	20.83
1	45.68	23.51	45.88	23.8

5.5 Fractional Derivative for Time Domain

Time domain models are needed to calculate state of charge (SOC). The SOC gives the fuel level remaining in flight, so its accurate prediction is crucial. The presence of a Warburg element or CPE complicates the conversion to the time domain. A time domain model of a Warburg or CPE involves fractional derivatives. There is a vast literature on fractional calculus, see for example, books by Miller and Ross [46] and Oldham and Spanier [47]. The implementation here follows [48].

The Warburg or CPE is essentially a capacitor with some leakage current, characterized by a factor α. In time domain, the voltage V of a capacitor C is related to the current I through a fractional derivative seen in Eq. (5.25), where α is a non-integer value between $0-1$. $\alpha = 1$ for an ideal capacitor.

$$C\,\frac{d^{\alpha}V}{dt^{\alpha}} = I \tag{5.25}$$

In Laplace domain, this becomes Eq. (5.26), assuming zero initial conditions without any loss of generality.

$$C\,\frac{V(s)}{I(s)} = \frac{1}{s^{\alpha}} \tag{5.26}$$

So to find V in time domain, the inverse Laplace of $1/s^{\alpha}$ must be found. This is easily

found. For an integer n, the Laplace transform of the function t^n is:

$$\mathcal{L}\{t^n\} = \frac{n!}{s^{n+1}}$$

For a general non-integer α, the factorial is generalized by the Gamma function Γ:

$$\mathcal{L}\{t^\alpha\} = \frac{\Gamma(\alpha+1)}{s^{\alpha+1}}$$

$\Gamma(n+1) = n!$ for integer n.

$\Gamma(\alpha+1) = \alpha\,\Gamma(\alpha)$ always.

Some commonly needed values are as follows.

$\Gamma(1) = 1$

$\Gamma(2) = 1$

$\Gamma(1/2) = \sqrt{\pi}$

$\Gamma(1/3) = 2.679$

$\Gamma(1/4) = 3.626$

Replacing α with $\alpha - 1$, and remembering the Gamma function evaluation is a constant, it follows that the inverse Laplace of $1/s^\alpha$ is as seen in Eq. (5.27).

$$\mathcal{L}^{-1}\left\{\frac{1}{s^\alpha}\right\} = \frac{t^{\alpha-1}}{\Gamma(\alpha)} \tag{5.27}$$

Using Eq. (5.26) and Eq. (5.27), analytical solutions of Eq. 5.25 can be found for simple currents.

For a step current, the expression for $I(t)$ is shown in Eq. (5.5), where $u = 0$ for $t < t_1$ and

1 afterward. $I(s) = 1/s$, hence $V(s) = 1/C\, s^{\alpha+1}$. Taking the Laplace inverse using Eq (5.27) and the identity $\Gamma(\alpha+1) = \alpha\,\Gamma(\alpha)$, the voltage is found as below in Eq. (5.5) where V_0 is $V(0)$.

$$I(t) = u(t - t_1)$$

$$V(t) = \frac{t^{\alpha}}{C\alpha\Gamma(\alpha)} + V_0$$

For a square pulse current, the expression for $I(t)$ is seen in Eq. (5.28), where $u = 1$ between t_1 and t_2 and 0 everywhere else. Following the same procedure as before, the voltage is found, as in Eq. (5.29).

$$I(t) = u(t - t_1) - u(t - t_2) \tag{5.28}$$

$$I(s) = \frac{1}{s}\left(e^{-s\,t_2} - e^{-s\,t_1}\right)$$

hence

$$V(s) = \frac{1}{C\, s^{\alpha+1}}\left(e^{-s\,t_2} - e^{-s\,t_1}\right)$$

$$V(t) = \frac{1}{C\alpha\Gamma(\alpha)}[(t - t_1)^{\alpha}u(t - t_1) - (t - t_2)^{\alpha}u(t - t_2)] + V_0 \tag{5.29}$$

The pulse current can be used as a template for any generic current variation with time. Any continuous current can be decomposed into a series of square pulses of step size h where $h = t_2 - t_1$. For simplicity, consider a constant h. Then the current at any time step when

$t = (k+1)\,h$ can be written as an accumulation of square pulses.

$$I_{k+1} = \sum_{i=0}^{k} I_i[u(t-ih) - u(t-(i+1)h)]$$

The voltage response follows as seen in Eq. (5.30).

$$\begin{aligned} V_{k+1} &= V_0 + \frac{h^\alpha}{C\,\alpha\,\Gamma(\alpha)} \sum_{i=0}^{k} f_i\, w_i \\ &\text{where} \\ f_i &= I_i \\ w_i &= (k+1-i)^\alpha - (k-i)^\alpha \end{aligned} \tag{5.30}$$

Eq. 5.30 is the time domain solution to Eq. 5.25. Note that the solution is not local but requires current at all previous time steps, including the initial current I_0.

It can be checked that for $\alpha = 1$ the simple Euler forward scheme is recovered:

$$V_{k+1} = V_k + \frac{h}{C}\, I_k \tag{5.31}$$

The solution in Eq. 5.30 is verified with analytical solutions to step and pulse currents (Eqs. 5.5 and 5.29 respectively) for $C = 1$ and various α in Figure 5.13. As α decreases from the ideal value of 1.0, the capacitance becomes lossy and the voltage response lags.

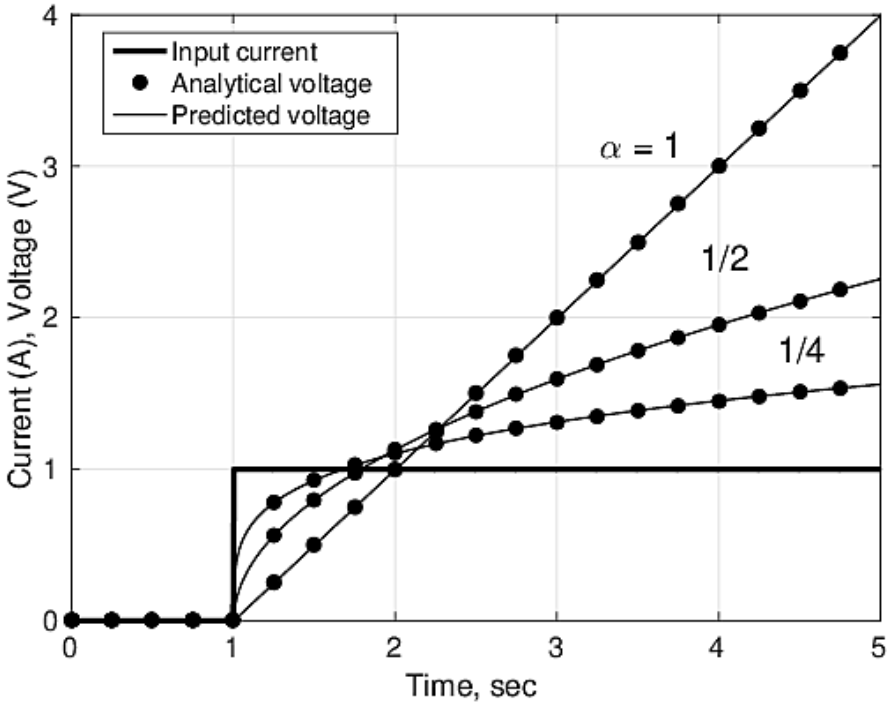

(a) Voltage in response to step current at $t = 1$ second.

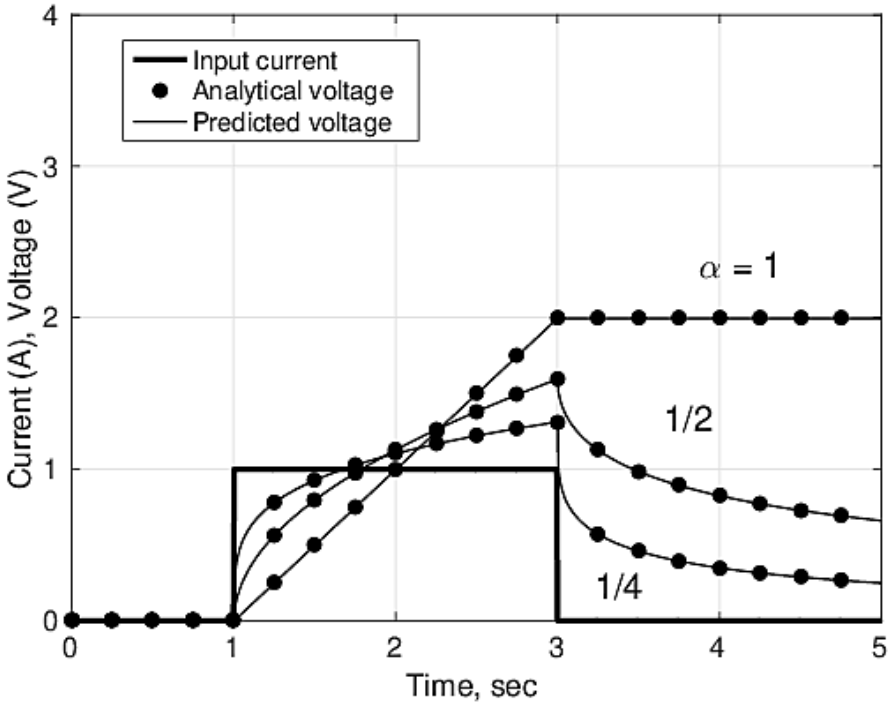

(b) Voltage in response to pulse current between $1 < t < 3$ seconds.

Figure 5.13: Verification of fractional finite difference with analytical solutions.

5.6 Blocks and Full Model in Time Domain

The ECM shown in Figure 5.9 are converted to the time domain block by block. The fractional derivative discussed in the previous section is used for the Warburg element and CPEs.

Block 1:

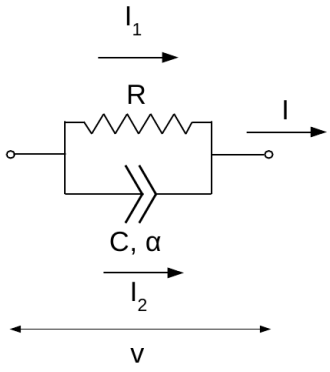

Figure 5.14: A R-C block.

Block 1 represents the anode and is modeled with a resistor R in parallel with a capacitor C (R//C) as shown in Figure 5.14. The capacitor in general is a CPE of order α. $\alpha = 1$ for an ideal capacitor. Given a current I, the voltage drop across the R//CPE block must be found.

Let the branch currents be I_1 through the resistor R and I_2 through the CPE. The current balance is as follows.

$$I = I_2 + I_1$$

The voltage is the same across the resistor and CPE. The CPE has capacitance C and is of order α. If this voltage is denoted V_C, then the voltage balance is as follows.

$$V_C = I_1 R$$

The current through the CPE is as follows.

$$I_2 = \frac{d^\alpha V_C}{dt^\alpha} = CR\frac{d^\alpha I_1}{dt^\alpha}$$

Substitution in the current balance equation gives the governing differential equation for I_1 of fractional order α where $0 < \alpha < 1$.

$$CR\frac{d^\alpha I_1}{dt^\alpha} + I_1 = I$$

It follows that I_1 is solved for in terms of a fractional derivative as in Eq. (5.6).

$$\frac{d^\alpha I_1}{dt^\alpha} = \frac{1}{CR}(I - I_1)$$

Consider N time steps of size h so that the time at the k-th step is $t_k = k\,h$ where $k = 0, 1, 2, ...N$. The current at step $k+1$ is obtained as follows.

$$\begin{aligned} I_{1k+1} &= I_{10} + \frac{h^\alpha}{\alpha\,\Gamma(\alpha)} \sum_{i=0}^{k} f_i\, w_i \\ &\text{where} \\ w_i &= (k+1-i)^\alpha - (k-i)^\alpha \\ f_i &= \frac{1}{C\,R}\,(I_i - I_{1i}) \end{aligned} \tag{5.32}$$

Given current I, the branch current I_1 can be solved as above. The branch current I_2 and

the block voltage V_C then fall out of the current and voltage balance respectively.

$$I_2 = I - I_1$$

$$V_{\text{block 1}} = V_C = I_1 R$$

As an example, the output block voltage in response to an input step current is calculated for the following parameters, and the results are shown in Figure 5.15.

$R = 1$ Ohm

$C = 1$ Farad

$\alpha = 1$ and $^1/_2$

Figure 5.15a shows that the current is initially drawn from the capacitor and as a consequence its voltage increases. For $\alpha = 1$, the voltage reaches a steady state eventually, when dV_C/dt becomes zero, so the current through the capacitor $C\, dV_C/dt$ becomes zero. The current is then drawn entirely through the resistor. For $\alpha = 1/2$, $d^\alpha V_C/dt^\alpha$ never becomes zero, which means there is always a current through the capacitor. Thus, the constant phase element acts like a capacitor with leakage.

Block 2:

Block 2 represents the cathode. A resistor R is in series with a Warburg capacitor (R-W) and the combination is in parallel with a CPE (R-W//CPE) as shown in Figure 5.14. The Warburg capacitor is a CPE with $\alpha = {}^1/_2$. Let the branch currents be I_1 through the resistor R and I_2 through the capacitor C.

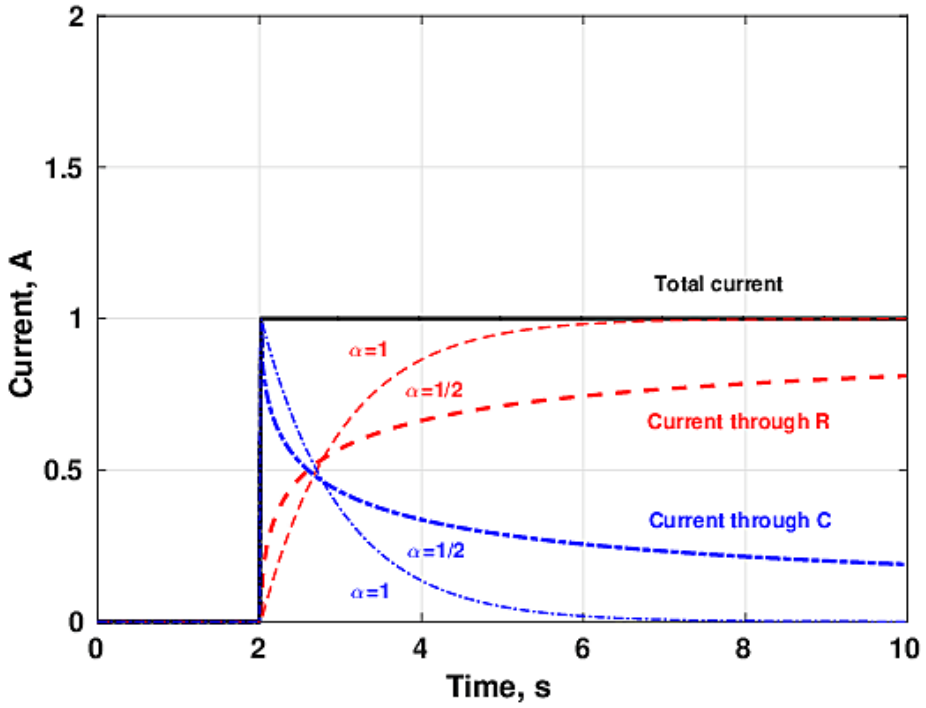

(a)

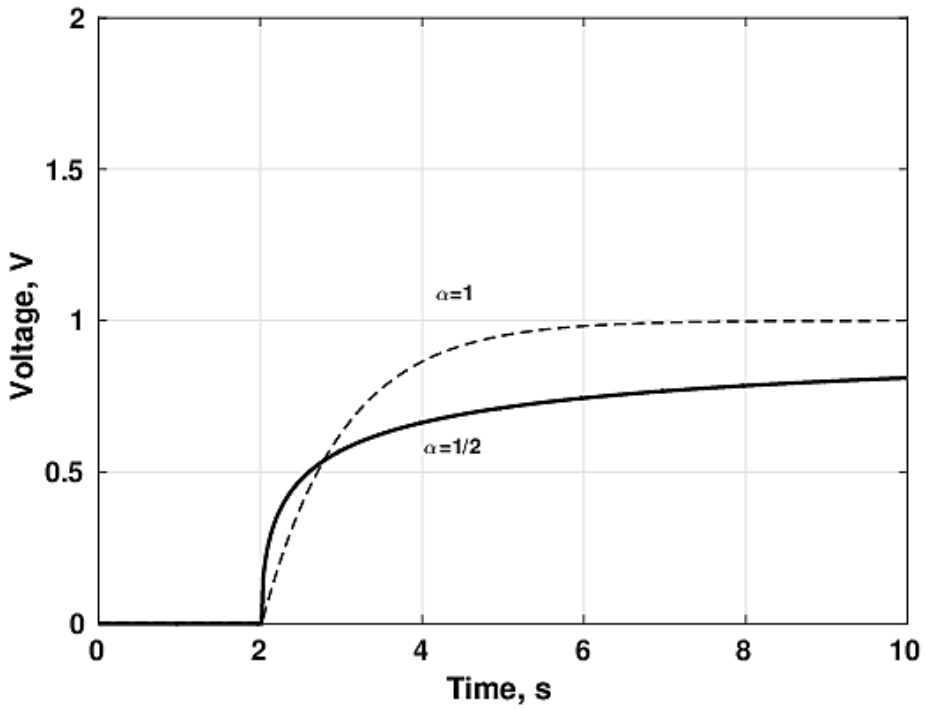

(b)

Figure 5.15: Output block voltage response to step current drawn through a R//C block circuit.

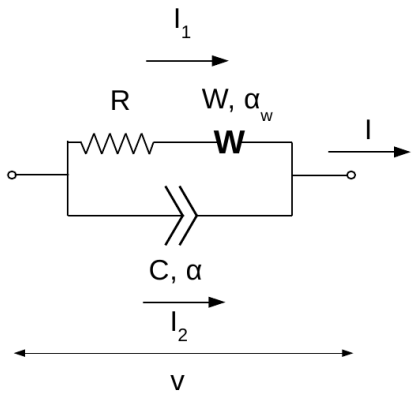

Figure 5.16: A R-W//C block.

The current and voltage balances are

$$I_2 + I_1 = I$$

$$V_C = I_1 R + V_W$$

The current through the CPE is

$$I_2 = C \frac{d^\alpha V_C}{dt^\alpha} = C R \frac{d^\alpha I_1}{dt^\alpha} + C \frac{d^\alpha V_W}{dt^\alpha}$$

Substitution in the current balance equation gives the governing differential equation for I_1 of fractional order α where $0 < \alpha < 1$.

$$C R \frac{d^\alpha I_1}{dt^\alpha} + C \frac{d^\alpha V_W}{dt^\alpha} + I_1 = I$$

This equation contains two unknowns I_1 and V_W.

But

$$W \frac{d^{\alpha_W} V_W}{dt^{\alpha_W}} = I_1$$

Now consider: $\alpha = \alpha_W$

This is normally a good assumption. This assumption is needed for a simple arrangement of the derivatives. Unlike non-negative integer derivatives, fractional orders do not follow the composition rule of exponents. Then the equation becomes,

$$C \frac{d^{\alpha} V_W}{dt^{\alpha}} = \frac{C}{W} I_1$$

and the governing equation reduces to

$$C R \frac{d^{\alpha} I_1}{dt^{\alpha}} + \left(1 + \frac{C}{W}\right) I_1 = I$$

It follows

$$\frac{d^{\alpha} I_1}{dt^{\alpha}} = \frac{I}{C R} - \frac{I_1}{R} \left(\frac{1}{C} + \frac{1}{W}\right) \tag{5.33}$$

which has the same form as Eq. 5.6 and therefore the same solution as Eq. 5.32 with the only change being,

$$f_i = \frac{I_i}{CR} - \frac{I_{1i}}{R} \left(\frac{1}{C} + \frac{1}{W}\right)$$

Thus, given current I, the branch current I_1 can be solved.

Next, the voltage across the Warburg element is found from its definition,

$$\frac{d^{\alpha_W} V_W}{dt^{\alpha_W}} = \frac{I_1}{W}$$

which has the same form as Eq. 5.6 and therefore a similar solution as Eq. 5.32.

$$\begin{aligned} V_{Wk+1} &= V_{W0} + \frac{h^{\alpha_W}}{\alpha_W \, \Gamma(\alpha_W)} \sum_{i=0}^{k} f_i \, w_i \\ &\text{where} \\ w_i &= (k+1-i)^{\alpha} - (k-i)^{\alpha} \\ f_i &= \frac{I_{1i}}{W} \end{aligned} \tag{5.34}$$

With I_1 and V_W known, the branch current I_2 and voltage V_C fall out of the current and voltage balance respectively.

$$I_2 = I - I_1$$

$$V_{\text{block 2}} = V_C = I_1 R + V_W$$

Full circuit:

The full circuit consists of two blocks and a resistor as shown earlier in Figure 5.9. The

output voltage of the full circuit is determined by Eq. (5.6). E is the open circuit voltage from the Shepherd model in Eq. (4.12). The iR term from the Shepherd model is now replaced with $IR_S - V_{\text{block 1}} - V_{\text{block 2}}$.

$$V = E - IR_S - V_{\text{block 1}} - V_{\text{block 2}}$$

For block 1, $R = R_1$, $C = C_1$ and $\alpha = \alpha_1$.

For block 2, $R = R_{CT}$, $C = C_2$, $\alpha = \alpha_W$, and W is the Warburg capacitance. The capacitance is related to the Warburg coefficient σ by $W = {}^{1}/_{\sqrt{2}\,\sigma}$.

5.7 Lithium Sulfur and Lithium-ion Measured Voltage Response

The voltage response of the Li-S and Li-ion cells were measured for step and pulse currents of magnitude C/2. Various pulse frequencies were applied: 0.20 Hz, 1.0 Hz, and 10 Hz. The voltage responses of the Li-ion cell to the step and pulse currents are shown in Figures 5.17-5.20. The voltage responses of the Li-S cell are shown in Figures 5.21-5.24. Li-ion has a much lower voltage drop for the same applied C-Rate of C/2. This is consistent with the lower impedance measured earlier.

The difference in the capacitative behavior is also apparent. Li-ion responds faster. The nature of the response makes it clear that the Shepherd model with just a resistance does not begin to capture the internal dynamics of the cells, particularly for the Li-S cells. Note that the current drawn is plotted negative in Figures 5.17-5.24 only for convenient axes - in the models, current drawn is positive.

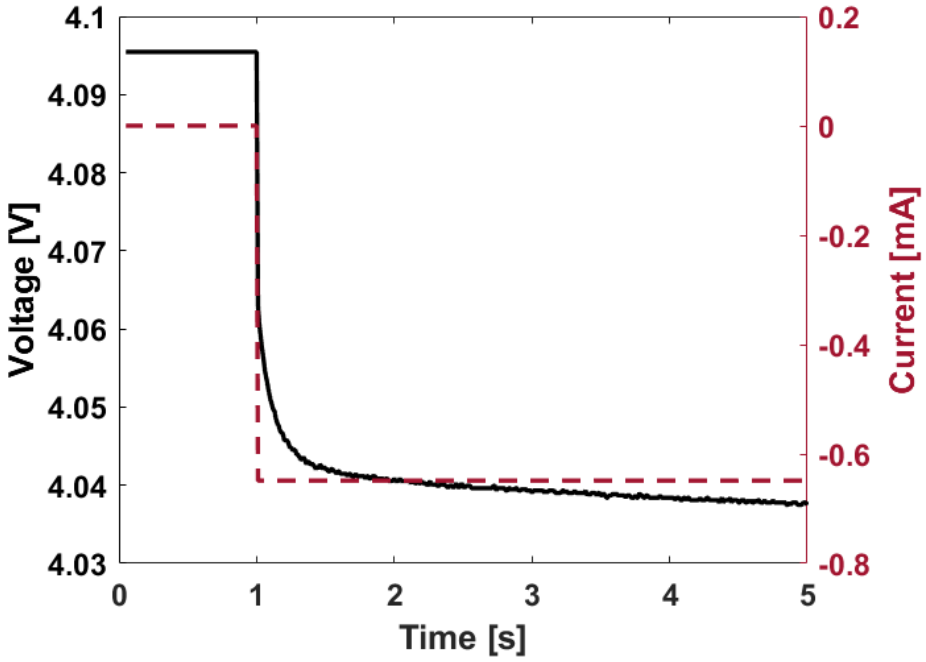

Figure 5.17: Measured Li-ion cell voltage response (solid line) to step current (dashed line), $I = C/2 = 0.649$ mA.

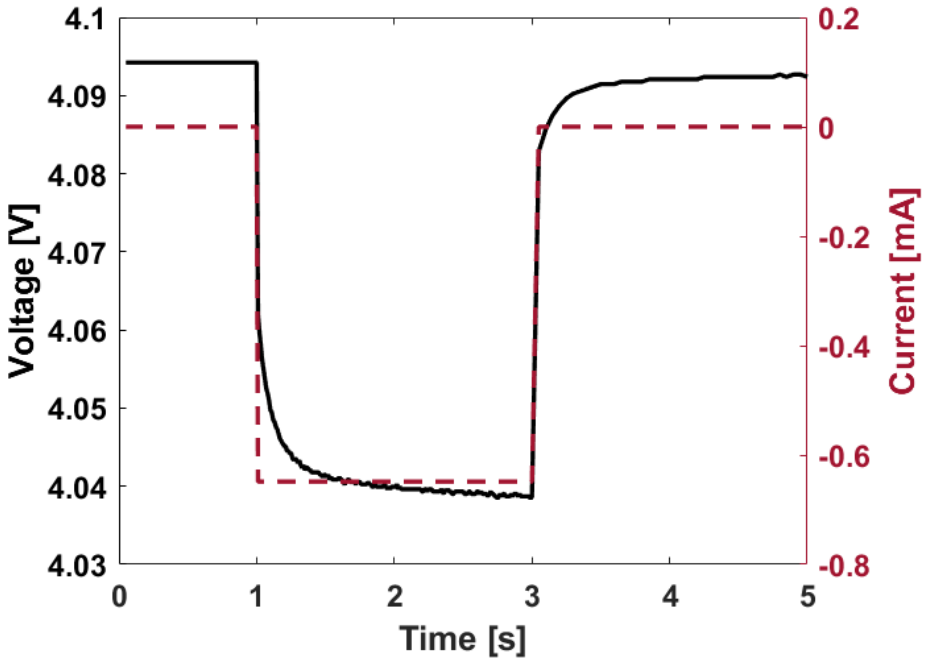

Figure 5.18: Measured Li-ion cell voltage response (solid line) to 0.20 Hz pulse current (dashed line), $I = C/2 = 0.649$ mA.

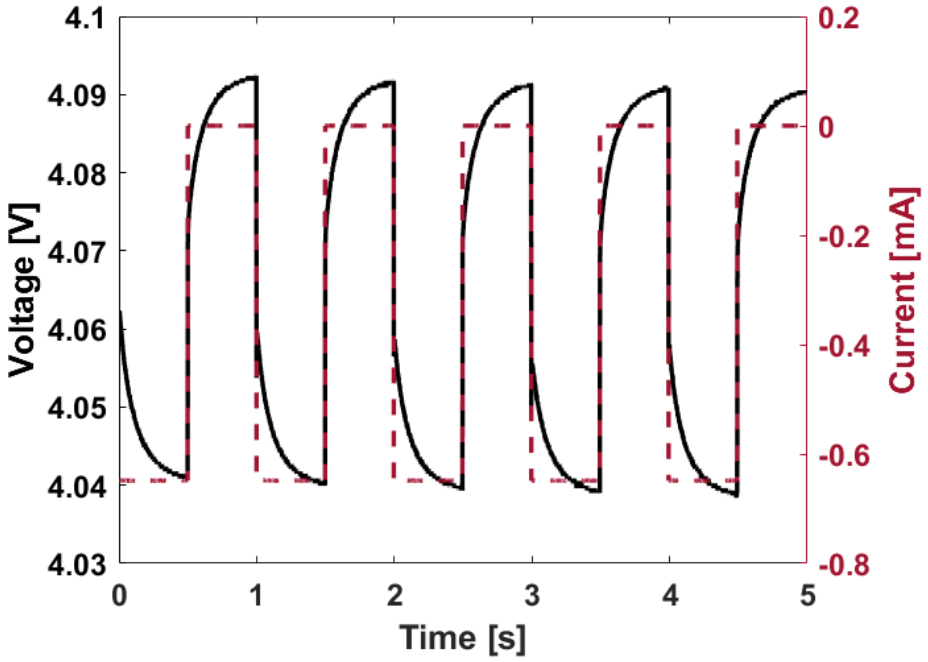

Figure 5.19: Measured Li-ion cell voltage response (solid line) to 1 Hz pulse current (dashed line), $I = C/2 = 0.649$ mA.

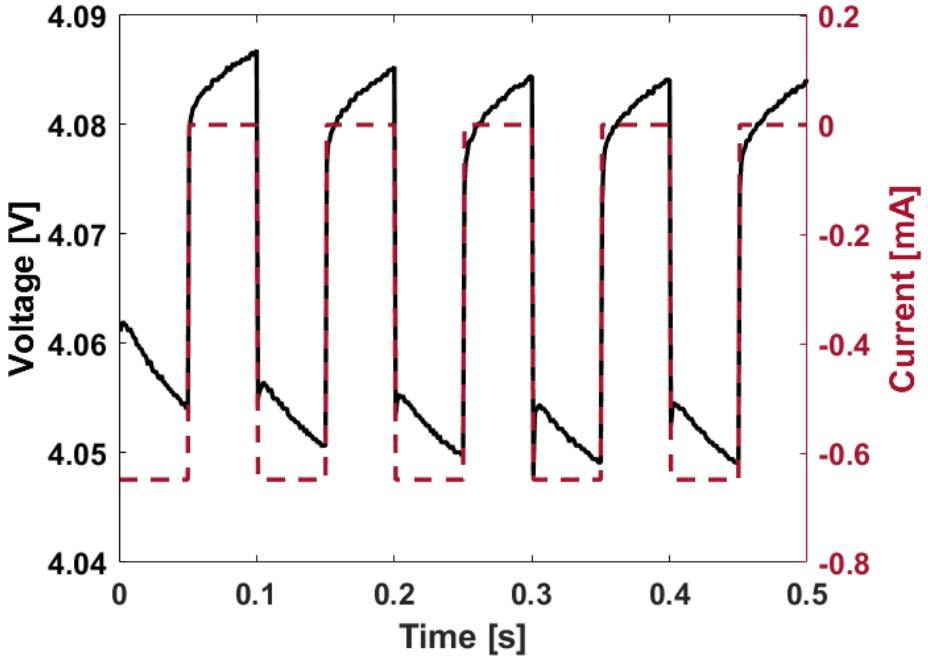

Figure 5.20: Measured Li-ion cell voltage response (solid line) to 10 Hz pulse current (dashed line), $I = C/2 = 0.649$ mA.

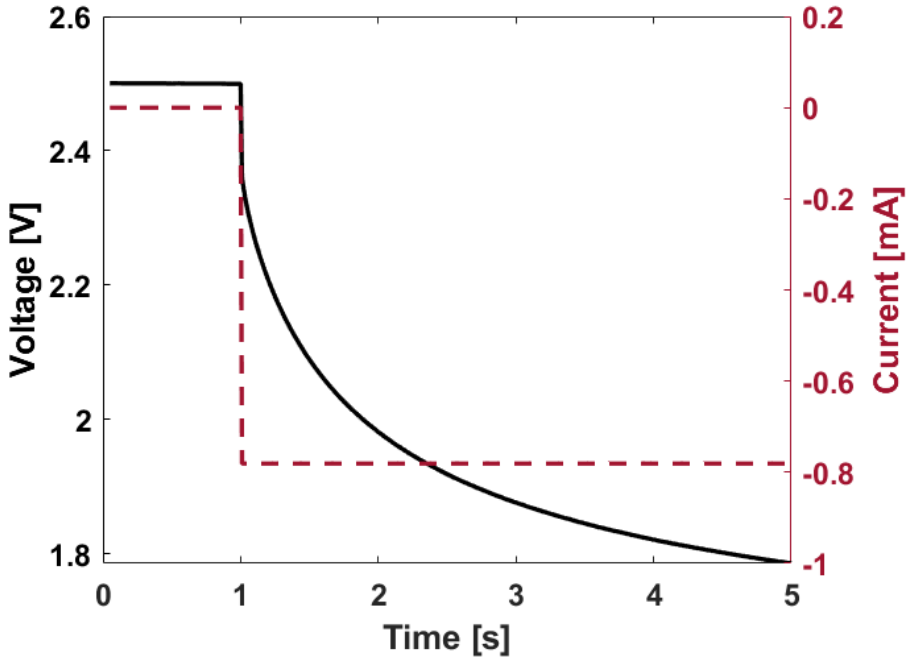

Figure 5.21: Measured Li-S cell voltage responses (solid line) to step current (dashed line), $I = C/2 = 0.782$ mA.

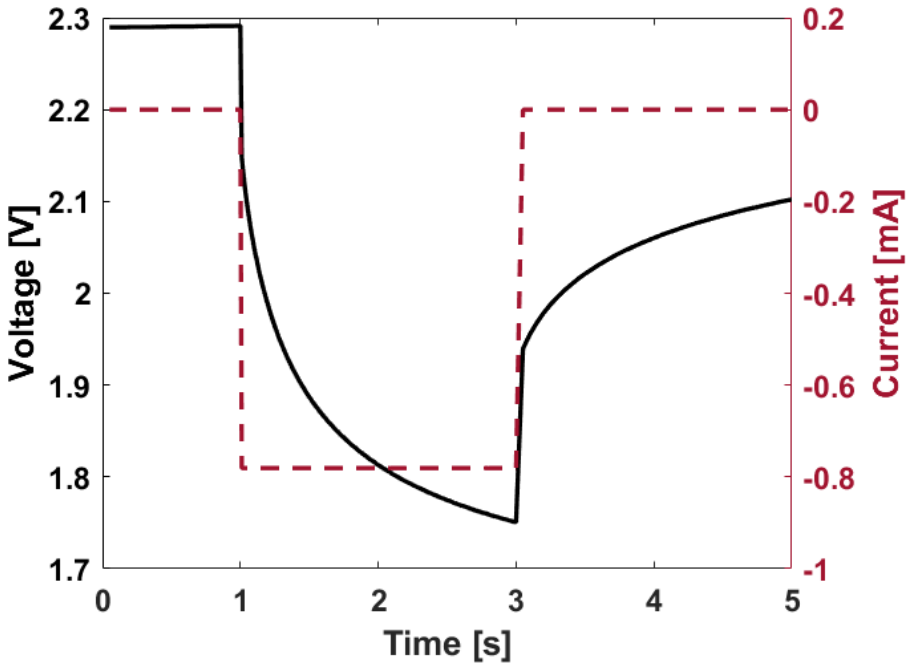

Figure 5.22: Measured Li-S cell voltage responses (solid line) to 0.2 Hz pulse current (dashed line), $I = C/2 = 0.782$ mA.

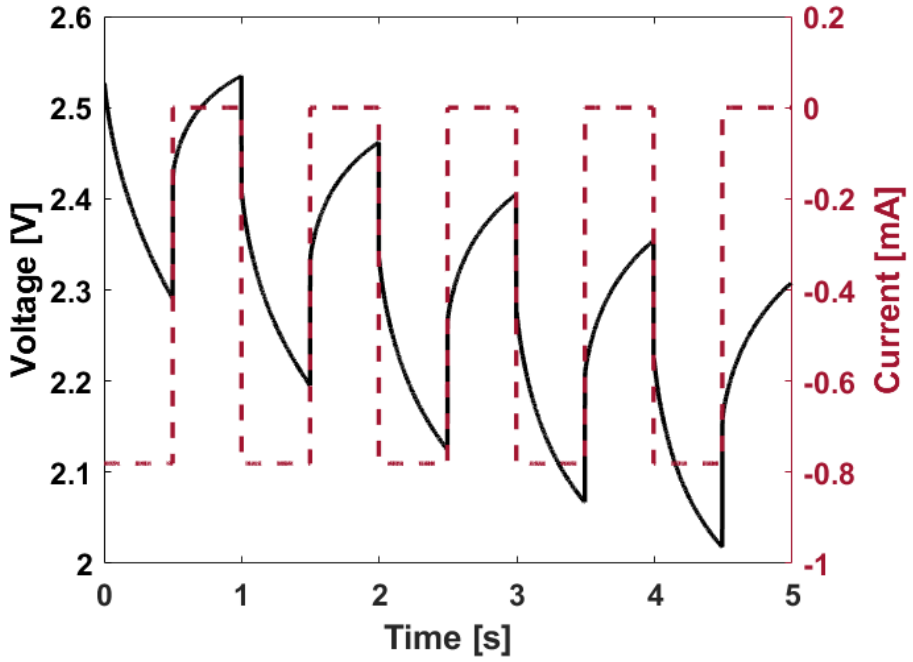

Figure 5.23: Measured Li-S cell voltage responses (solid line) to 1 Hz pulse current (dashed line), $I = C/2 = 0.782$ mA.

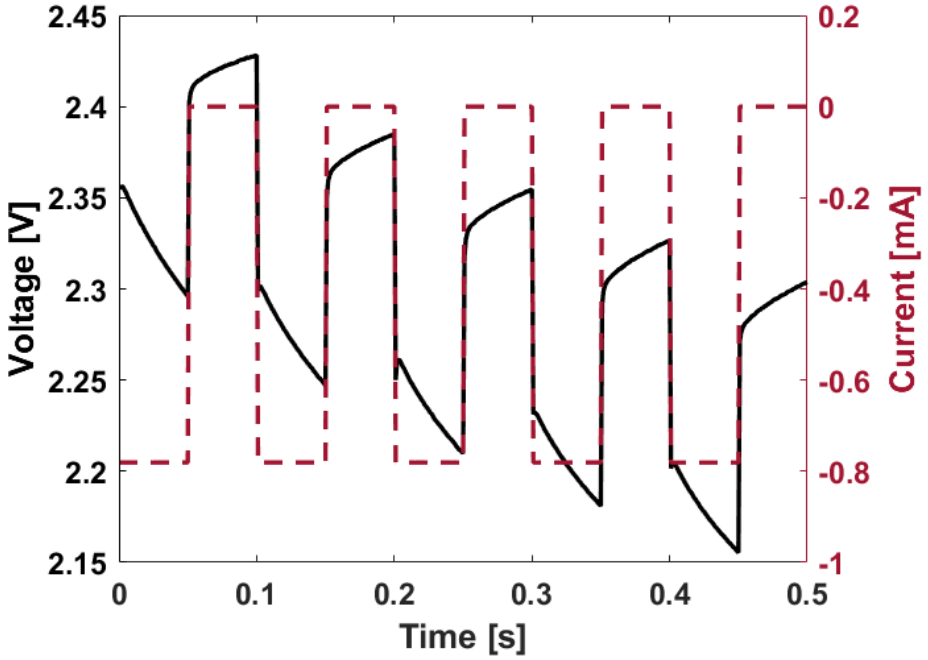

Figure 5.24: Measured Li-S cell voltage responses (solid line) to 10 Hz pulse current (dashed line), $I = C/2 = 0.782$ mA.

5.8 Fitting the Time Domain Model

The developed time domain model should be able to predict the measured transient data shown in Figures 5.17-5.24. The model parameters are determined by best fit to the collected step response data.

The goal was to find the best fit for the simplest model first, with only V_S and $V_{\text{block 1}}$:

$$V = E - I\,R_S - V_{\text{block 1}}$$

The model is then progressively refined to understand the impact of additional blocks. The parameters extracted for Li-ion are given in Table 5.6. The first column gives the parameters that best represent the step, 0.20 Hz pulse, and 1.0 Hz pulse response. For these voltage responses, a single R//C block is adequate. The higher frequency 10 Hz pulse current required the full circuit model. The parameters required for the 10 Hz pulse current are found in the final column of Table 5.6. The corresponding predictions are shown in Figures 5.25 and 5.26.

The extracted parameters for Li-S are in Table 5.7. The first column gives the parameters that best represent the step response. For a step response, a single R//C block is adequate. The second column gives the parameters that best represent the 0.20 Hz and 1.0 Hz pulse response. These pulse responses require the full circuit with both R//C blocks and the Warburg element. The third column shows new parameters required to accurately model the behavior for the higher frequency 10 Hz pulse current. The corresponding predictions are shown in Figures 5.27 and 5.28.

Table 5.6: Time domain model parameters extracted from Li-ion step and pulse current data.

Parameter	Units	Step 0.20 Hz Pulse 1.0 Hz Pulse	10 Hz Pulse
E	V	4.1	4.1
$\mathbf{R_s}$	Ω	5.60	5.6
$\mathbf{R_1}$	Ω	79.4	28.8
$\mathbf{C_1}$	Farad	$9.12 \cdot 10^{-4}$	$1.09 \cdot 10^{-6}$
α_1		0.65	0.77
$\mathbf{R_{CT}}$	Ω	-	32.0
$\mathbf{C_2}$	Farad	-	$4.69 \cdot 10^{-3}$
α_2		-	0.60
W	Farad	-	0.92
α_W		-	0.60

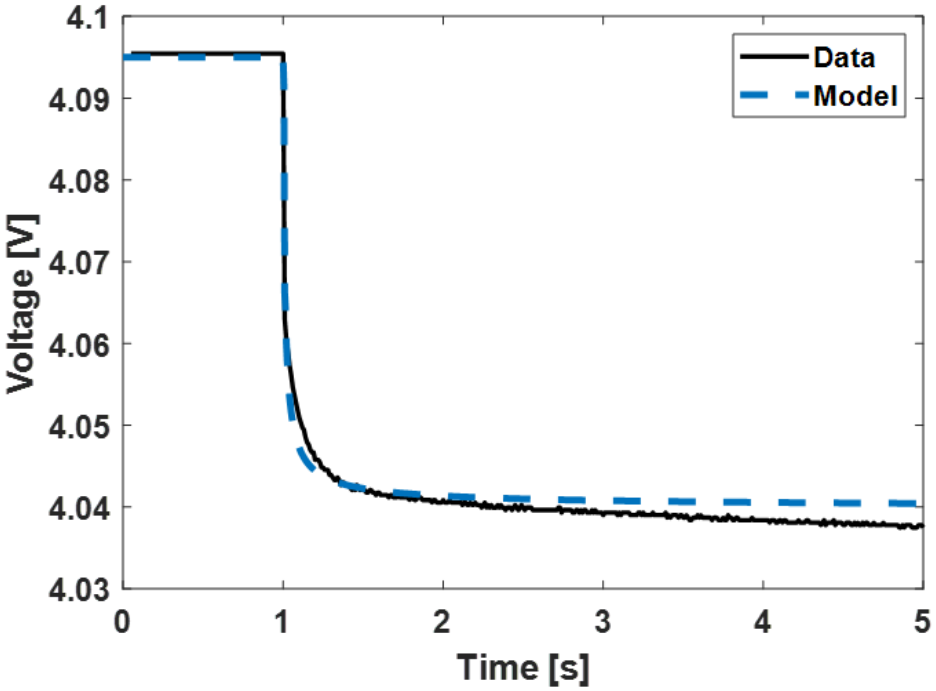

(a) Voltage response to step current at $t = 1$ second.

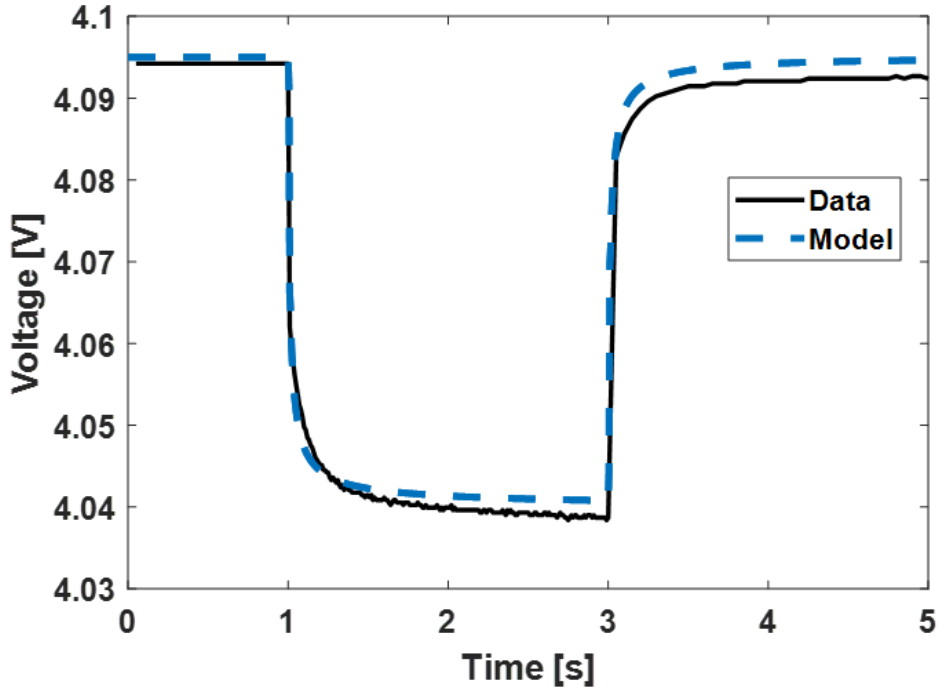

(b) Voltage response to pulse current between $1 < t < 3$ seconds.

Figure 5.25: Actual and predicted voltage response of a Li-ion coin cell for step and pulse currents with $I = C/2$.

Table 5.7: Time domain model parameters extracted from Li-S step and pulse current data.

Parameter	Units	Step	0.20 Hz Pulse 1.0 Hz Pulse	10 Hz Pulse
E	V	2.5	2.5	2.5
$\mathbf{R_s}$	Ω	230	180	110
$\mathbf{R_1}$	Ω	681	230	130
$\mathbf{C_1}$	Farad	$1.20 \cdot 10^{-3}$	$1.20 \cdot 10^{-3}$	$1.20 \cdot 10^{-3}$
α_1		0.90	0.90	0.90
$\mathbf{R_{CT}}$	Ω	-	7.0	7.0
$\mathbf{C_2}$	Farad	-	$4.20 \cdot 10^{-3}$	$3.12 \cdot 10^{-4}$
α_2		-	0.83	0.88
W	Farad	-	$2.35 \cdot 10^{-3}$	$1.05 \cdot 10^{-3}$
α_W		-	0.83	0.83

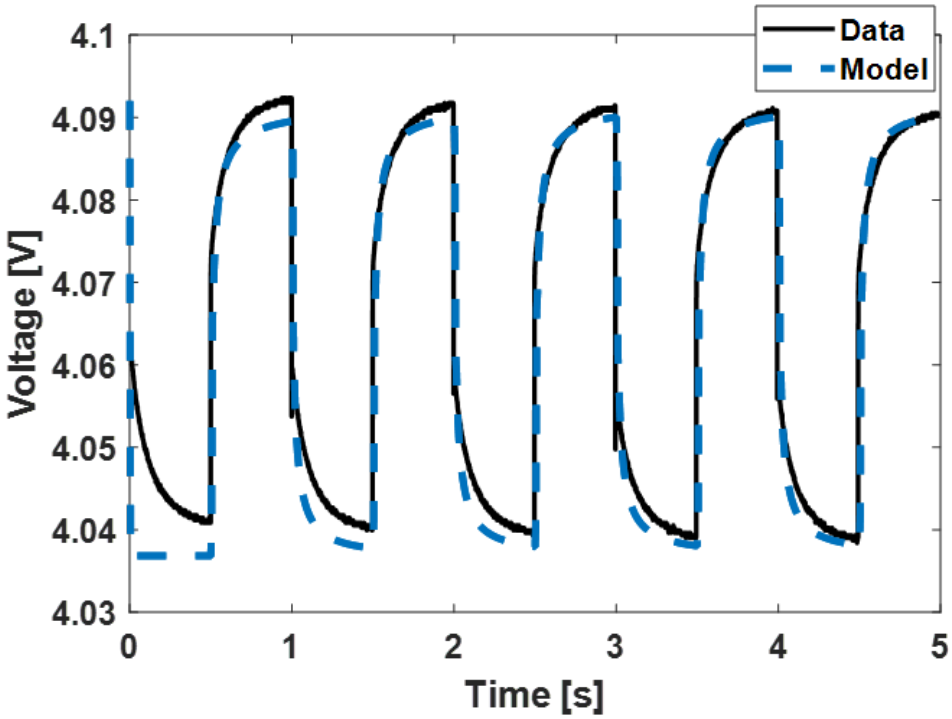

(a) Voltage response to 1Hz square current.

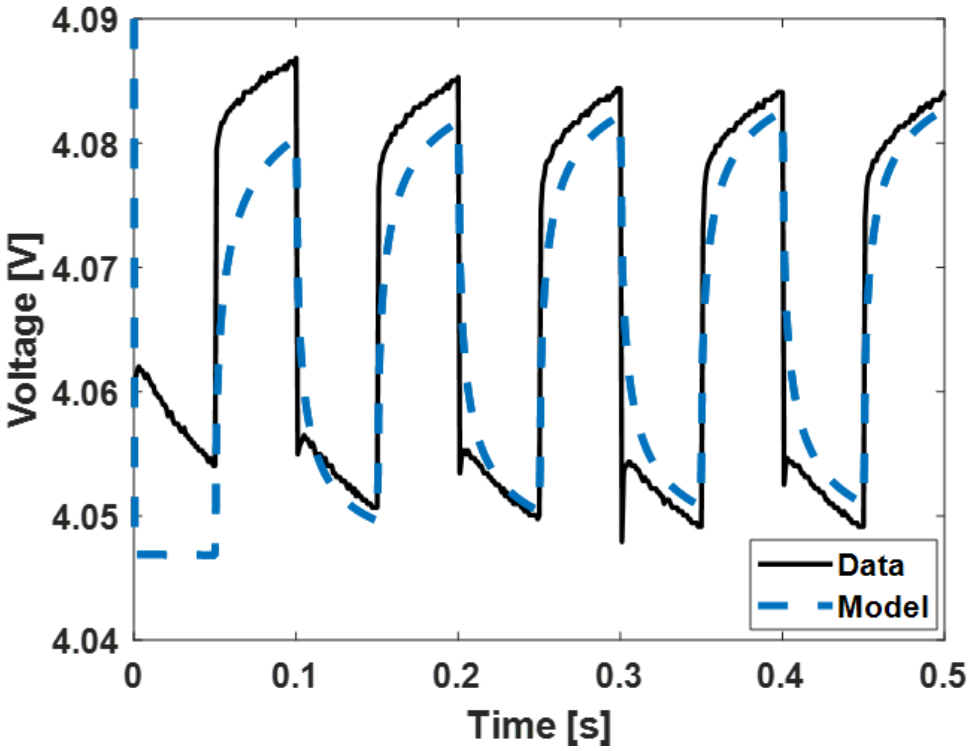

(b) Voltage response to 10Hz square current.

Figure 5.26: Predicted and actual voltage response of a Li-ion coin cell for square currents of 1Hz and 10Hz frequency, $I = C/2$.

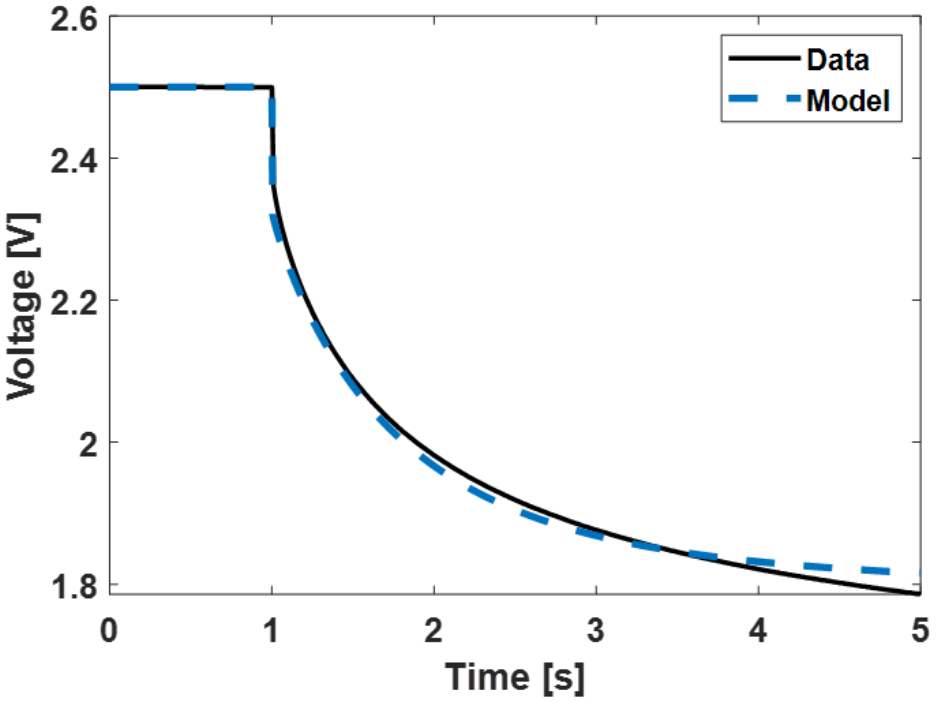

(a) Voltage response to step current at $t = 1$ second.

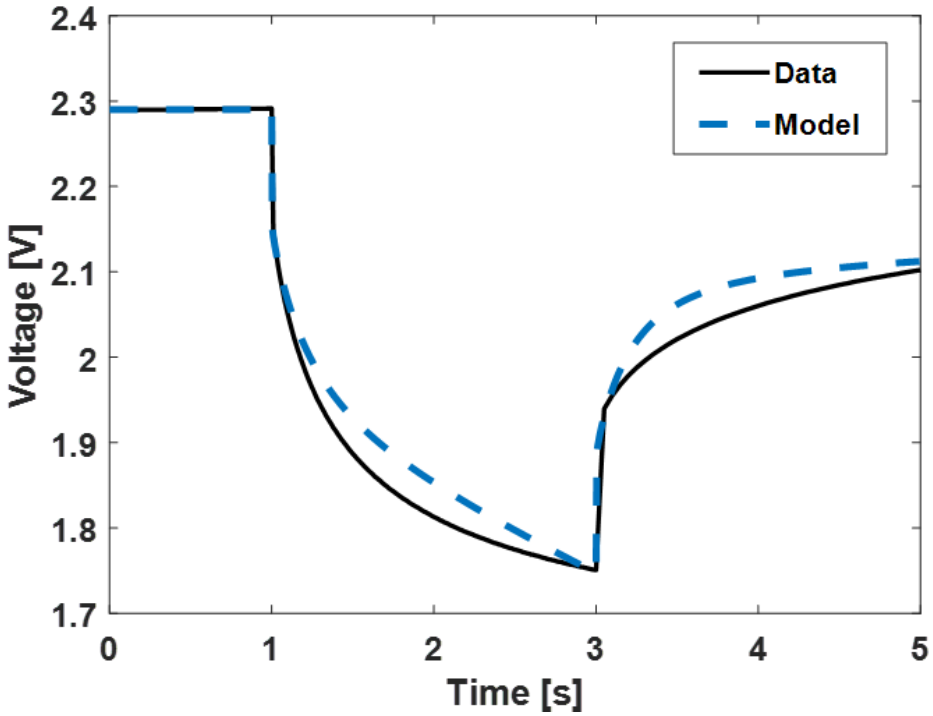

(b) Voltage response to pulse current between $1 < t < 3$ seconds.

Figure 5.27: Predicted and actual voltage response of a Li-S coin cell for step and pulse currents with $I = C/2$.

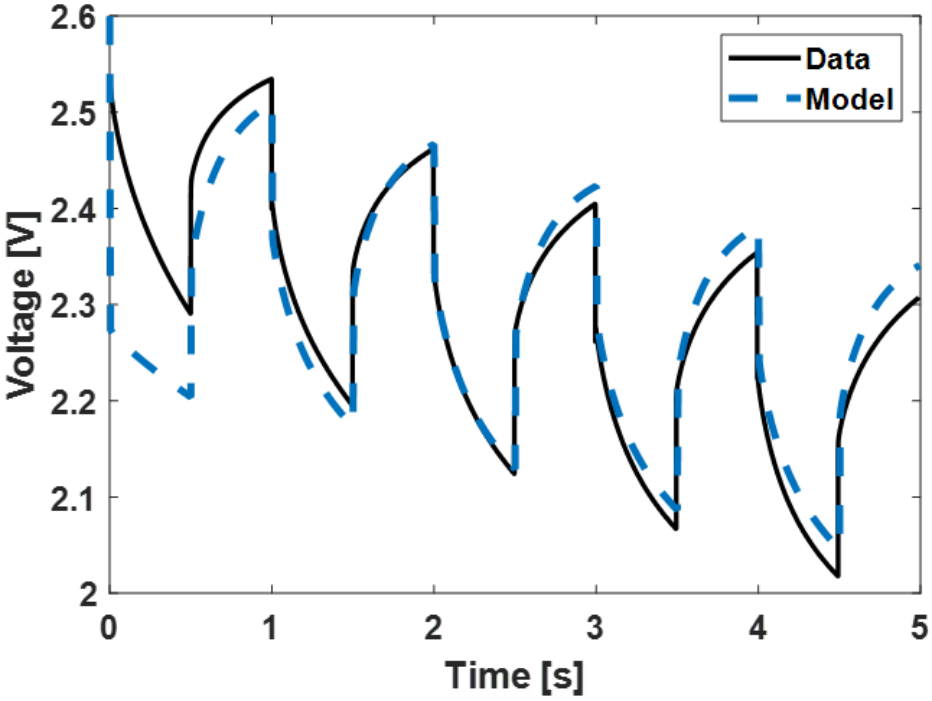

(a) Voltage response to 1Hz square current.

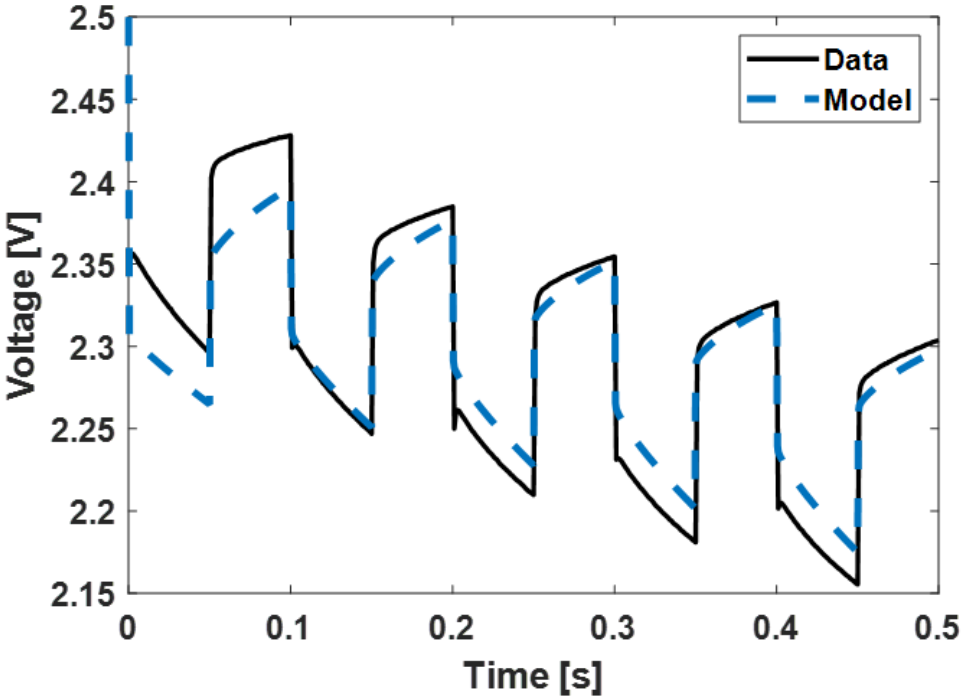

(b) Voltage response to 10Hz square current.

Figure 5.28: Predicted and actual voltage response of a Li-S coin cell for square currents of 1Hz and 10Hz frequency, $I = C/2$.

5.9 Summary

Transient data in the frequency and time domain were collected for Li-S and Li-ion cells. An ECM was developed and model parameters were extracted. The model was converted from the frequency domain into the time domain. Voltage responses to step and pulse currents were collected for Li-S and Li-ion cells, and model parameters were extracted for this time domain data.

1. Differences in behavior are explained by the internal nature of the cells. The Li-S cells exhibited an order of magnitude higher internal resistance. They also exhibited a marked Warburg-like behavior at the low frequencies of 1-100 Hz, a frequency range important in rotor response.

2. In general, a transient model of the type R-R//CPE-RW//CPE is adequate to capture the impedance behavior. There is significant variation from cycle to cycle, hence the transient time domain response is not always consistent with EIS.

3. The dynamic behavior of the cells is characterized generally by a first-order lag in cell voltage in response to changing current. The nature of the lag is difference between Li-ion and Li-S. The Li-ion is faster with a smaller time constant and is well represented by a resistor and a resistor-capacitor block. The Li-S is slower with a longer time constant and requires a non-ideal capacitor, i.e., a constant phase element, and for lower frequencies in the 1-100Hz range, the Warburg.

With transient testing of the Li-S and Li-ion cells completed, focus shifted to the impact of advanced Li-S batteries on eVTOL sizing and battery pack design.

Chapter 6: Impact of Advanced Batteries on Sizing

The impact of advanced batteries on eVTOL sizing is investigated. The benefits of using Li-S and Li-ion batteries in tandem are discussed and sizing results are shown for this scenario. The steps for designing and sizing a battery pack are described.

6.1 Impact on Range

A decrease in battery capacity has a drastic impact on the achievable range of a quadrotor. For Mission 2 (400 lbs payload, 5 minute hover time, 5 minute fuel cruise reserves), the effect of capacity decrease as mission number increases can be seen in Figure 6.1. Beginning with a fresh cell, the specific energy was set to 300 Wh/kg. After 200 missions, so 200 cycles for the battery, the capacity decreases by 20% and the range for a set GTOW decreases. Increasing the mission count to 800 decreases the capacity to half that of a fresh cell, and the range for a certain GTOW decreases by at least half.

6.2 Battery Sharing

The Ragone plot shown in Figure 4.16a determined that at C-Rates at and under 1C, Li-S surpasses Li-ion in specific power and energy. Above 1C, Li-S energy drastically decreases and Li-ion is preferred. The implications for eVTOL are that an all-electric quadrotor could carry both

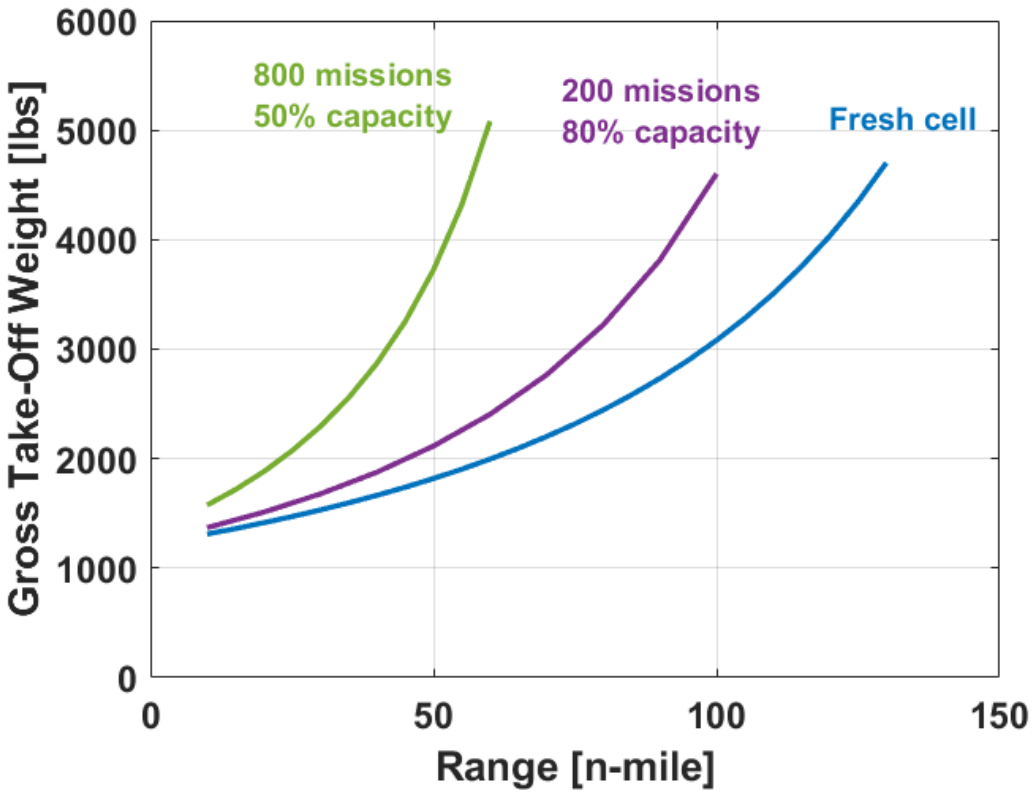

Figure 6.1: Effect of battery capacity decrease on quadrotor range.

a Li-S and a Li-ion battery, and switch between them based on the required power and C-Rate. For example, the Li-ion battery could be used in high power situations such as hovering, and the Li-S battery could be used while in cruise. Figure 6.2 shows the GTOW as range increases, when using Li-S batteries for cruise and Li-ion batteries for hover. The weights of the Li-S and Li-ion batteries as range increases are shown. As the Li-ion battery would be only used for hovering, the weight is constant as the hover time remains the same for all ranges. The weight of the Li-S battery increases with range, as the cruise time also increases and therefore more energy is required. The GTOW for the 50 n-mile range is 1,469 lbs. This is an improvement on the sizing GTOW results reported in Table 2.6.

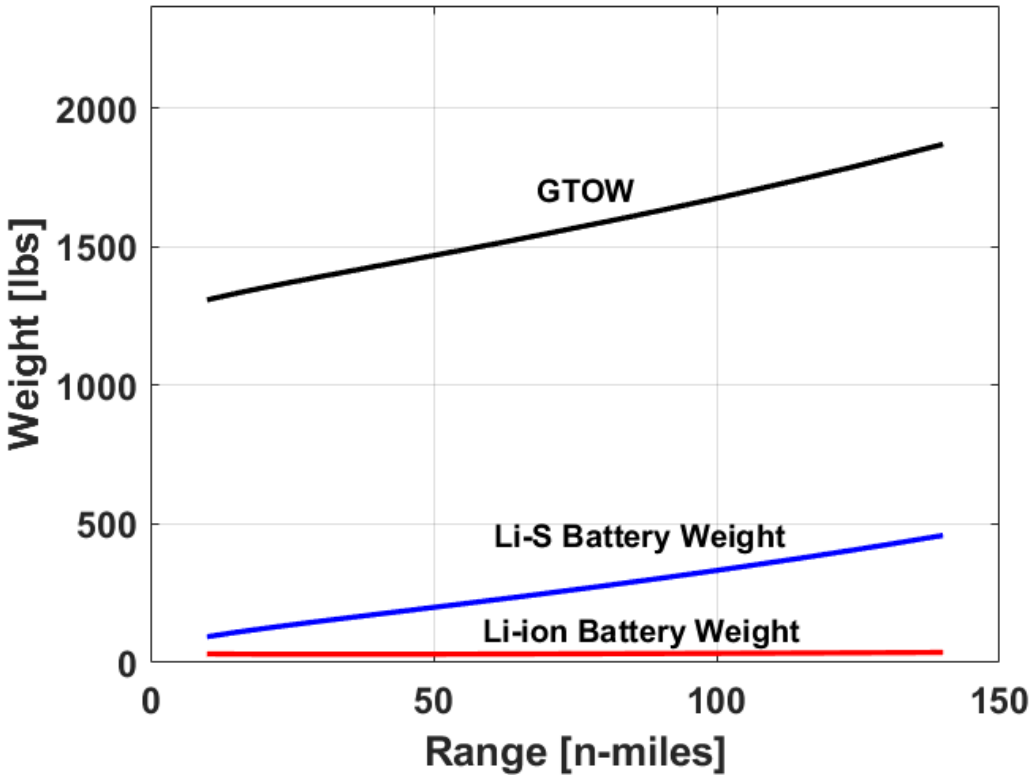

Figure 6.2: Effect of battery sharing on GTOW as range increases.

6.3 Battery Pack Sizing and Design

To precisely size a battery for an eVTOL flight, the power, current, and time for the flight are needed. Figure 6.3 shows an example mission with three segments of varying power required. The first segment requires the most power for the shortest amount of time. The second segment has the lowest power requirement for the longest amount of time. The third segment has a middling power requirement. The end of flight (EOF) occurs after the third segment.

To size the battery, the following steps are followed. First, the charge capacity for each segment must be calculated. Then, the C-Rate of each segment can be determined. Next a charge capacity margin is set. The energy for each segment can then be calculated, and then the weight

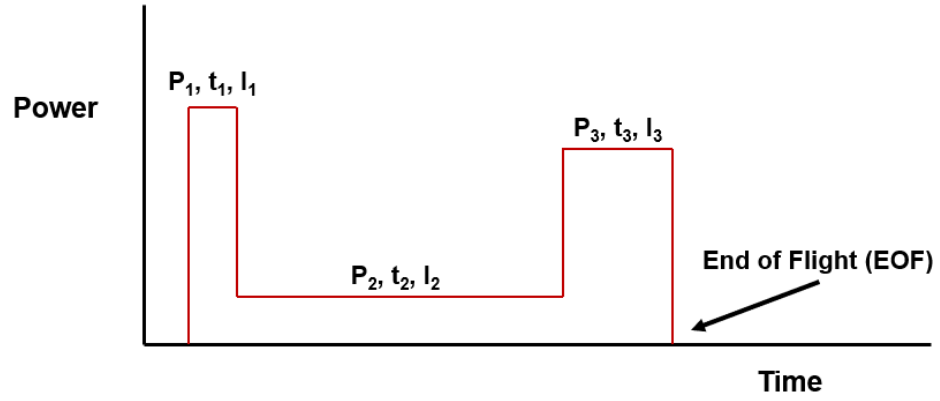

Figure 6.3: Example mission with three segments of known power, time, and current requirements.

of the battery can be determined. Next the number of cells in series and parallel are found, and the weight of each cell can be calculated. Finally, the method of in-flight battery analysis is determined.

Calculate charge capacities:

The charge capacities for each segment can easily be calculated as in Eq. (6.1), where Q_1 is the charge capacity for segment 1, Q_2 for segment 2, and Q_3 for segment 3. The charge capacity for the full flight is the summation of the charge capacity of each segment as in Eq. (6.2).

$$\begin{aligned} Q_1 &= I_1 t_1 \\ Q_2 &= I_2 t_2 \\ Q_3 &= I_3 t_3 \end{aligned} \tag{6.1}$$

$$Q = Q_1 + Q_2 + Q_3 \tag{6.2}$$

Calculate C-Rates:

Next, the C-Rates of each segment must be found. Take the maximum current, I_1.

$$C_1 = \frac{I_1}{Q} \tag{6.3}$$

If C_1 is greater than a specified maximum C-Rate, then the average charge capacity is as in Eq. (6.4). This would leave some excess charge capacity, found in Eq. (6.5).

$$Q_{ave} = \frac{I_1}{C_{max}} \tag{6.4}$$

$$Q_{extra} = Q_{ave} - Q = \frac{I_1}{C_{max}} - \frac{I_1}{C_1} \tag{6.5}$$

Otherwise, the average charge capacity is equal to Q as calculated in Eq. (6.2) and there is no Q_{extra}.

The total charge capacity is as calculated in Eq. (6.6), where ΔQ is an additional margin that is set if needed. The C-Rates of each segment are then determined using Eq. (6.7)

$$Q_{total} = Q_{ave} + \Delta Q \tag{6.6}$$

$$C_1 = \frac{I_1}{Q_{total}}$$
$$C_2 = \frac{I_2}{Q_{total}} \tag{6.7}$$
$$C_3 = \frac{I_3}{Q_{total}}$$

Set ΔQ Margin:

The ΔQ margin is now set. Ensure a certain cell voltage at EOF, v_{EOF}. From this specified v_{EOF}, find the depth of discharge at the end of flight, DOD_{EOF} (or $SOC_{EOF} = 1 - DOD_{EOF}$) from the discharge data for the C-Rate at the end of flight. Here, it is the C-Rate for segment three. Figure 6.4 shows an example of a voltage versus DOD discharge curve for a certain C-Rate. With v_{EOF} known, DOD_{EOF} can easily be determined. DOD_{EOF} can then be used to calculate ΔQ as in Eq. (6.8).

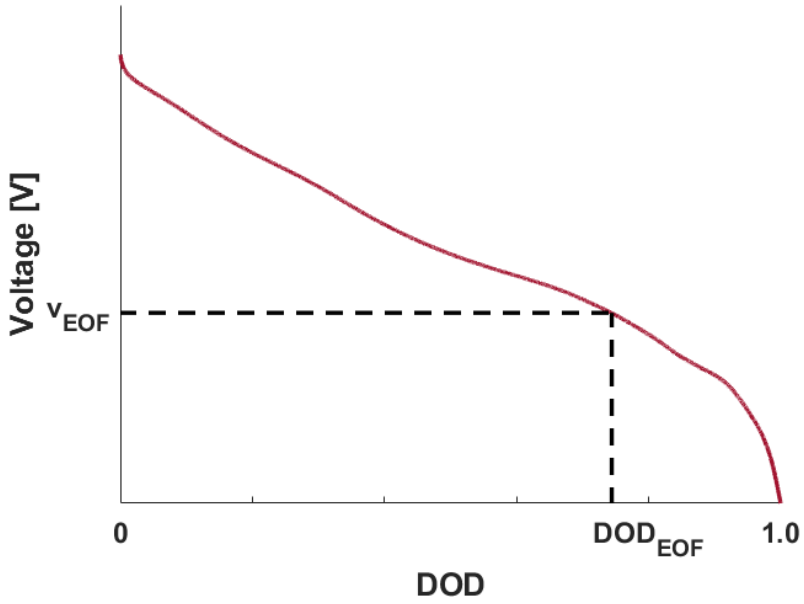

Figure 6.4: Example of Voltage vs DOD curve for a certain C-Rate. End of flight voltage and DOD are marked.

$$\begin{aligned} DOD_{EOF} = \quad & \frac{Q_{ave}}{Q_{total}} = \frac{Q_{ave}}{Q_{ave} + \Delta Q} \\ \Delta Q = \quad & \frac{Q_{ave}}{DOD_{EOF}} - Q_{ave} \end{aligned} \tag{6.8}$$

Calculate energies:

To calculate the energies, the voltages for each segment are needed. Let v_1, v_2, and v_3 be the average voltages over each segment as in Eq. (6.9), where v is the instantaneous voltage. The energy of each segment is then found using Eq. (6.10). As there is extra charge capacity, there will also be extra energy capacity. This extra energy capacity is calculated using Eq. (6.11), where the voltage used depends on where the extra energy will be spent - segment 1, 2, or 3. This is left up to the aircraft and battery designer to decide. Finally, the ΔE from the ΔQ margin is found by Eq. (6.12).

$$\begin{aligned} v_1 &= \frac{1}{t_1}\int_0^{t_1} v dt \\ v_2 &= \frac{1}{t_2}\int_0^{t_2} v dt \\ v_3 &= \frac{1}{t_3}\int_0^{t_3} v dt \end{aligned} \tag{6.9}$$

$$\begin{aligned} E_1 &= I_1 \int_0^{t_1} v dt = I_1 t_1 v_1 \\ E_2 &= I_2 \int_0^{t_2} v dt = I_2 t_2 v_2 \\ E_3 &= I_3 \int_0^{t_3} v dt = I_3 t_3 v_3 \end{aligned} \tag{6.10}$$

$$E_{extra} = (Q_{ave} - Q) v_{1,2, \text{ or } 3} = \left(\frac{I_1}{C_{max}} - \frac{I_1}{C_1}\right) v_{1,2, \text{ or } 3} \tag{6.11}$$

$$\Delta E = \Delta Q v_3 = \big(\frac{1}{DOD_3} - 1\big) Q_{ave} v_3 \tag{6.12}$$

Calculate weights:

To find the specific energy (SE) at each segment C-Rate (C_1, C_2, and C_3), use data from a Ragone plot such as the one shown in Figure 4.16a. Figure 6.5 shows the SE versus C-Rate data as points; the trend of these data, shown as a black dashed line, can determine the SE at various C-Rates. These SE values are then used in Eq. (6.13) to find the weight of the required battery.

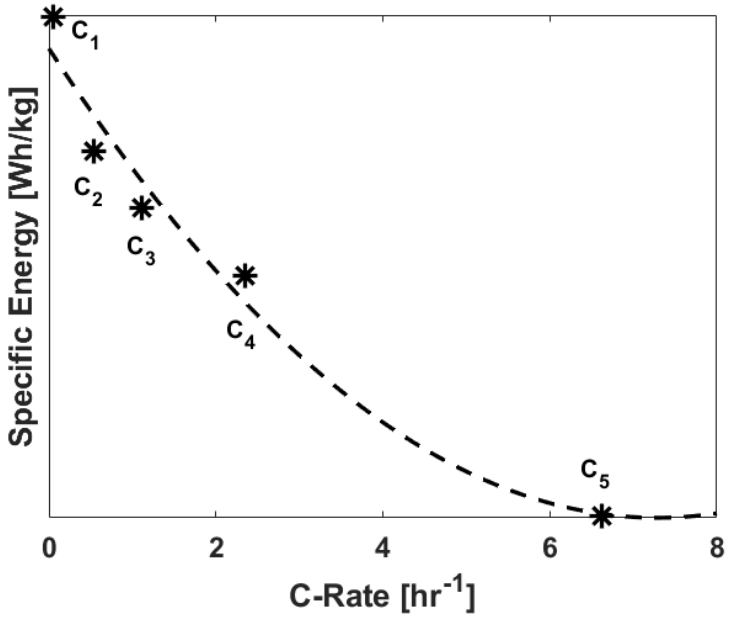

Figure 6.5: Specific energy vs C-Rate data and trendline.

$$W = \frac{E_1}{SE(C_1)} + \frac{E_2}{SE(C_2)} + \frac{E_3}{SE(C_3)} + \frac{E_{extra}}{SE(C_{1,2,\text{ or }3})} + \frac{\Delta E}{SE(C_3)} \tag{6.13}$$

Only power and energy:

Consider the situation where only power and energy are given. The battery sizing can still be determined, but only if the voltage is the same for all segments. This is because C-Rate is defined

by Eq. (6.14). Now, consider Eq. (6.15). So $C_1 = P_1/E_{total}$, only if $v_1 = v_2 = v_3$.

Normally, voltage is proportional to motor RPM. So this situation is acceptable for conventional helicopters with a constant RPM, as the voltage is constant ($v_1 = v_2 = v_3$). However for eVTOL, RPM varies with each segment. Therefore it is important to calculate C-Rate based on charge, as in Eq. (6.7), not based on energy.

$$C_1 = \frac{I_1}{Q_{total}} = \frac{I_1}{Q + Q_{extra} + \Delta Q} = \frac{I_1}{I_1 t_1 + I_2 t_2 + I_3 t_3 + \left(\frac{I_1}{C_{max}} - \frac{I_1}{C_1}\right) + \Delta Q} \tag{6.14}$$

$$\frac{P_1}{E_{total}} = \frac{I_1 v_1}{I_1 t_1 v_1 + I_2 t_2 v_2 + I_3 t_3 v_3 + \left(\frac{I_1}{C_{max}} - \frac{I_1}{C_1}\right) v_{1,2, \text{ or } 3} + \Delta Q v_{1,2, \text{ or } 3}} \tag{6.15}$$

Determine number of cells:

Cells connected in series increase the voltage of the system. Figure 6.6a shows an example of three cells connected in series. The voltage V supplied by this circuit can be calculated using Eq. (6.16), which comes out to be 6.0 V. The charge capacity does not add for series connections, so would be 10 Ah.

$$V = \sum_{i=1}^{n} V_i \tag{6.16}$$

Cells connected in parallel increase the charge capacity of the system. Figure 6.6b shows an example of three cells connected in parallel. The charge capacity Q supplied by this circuit can be calculated using Eq. (6.17), which comes out to be 30 Ah. The voltage does not add for

parallel connections, so would be 2.0 V.

$$Q = \sum_{i=1}^{m} Q_i \tag{6.17}$$

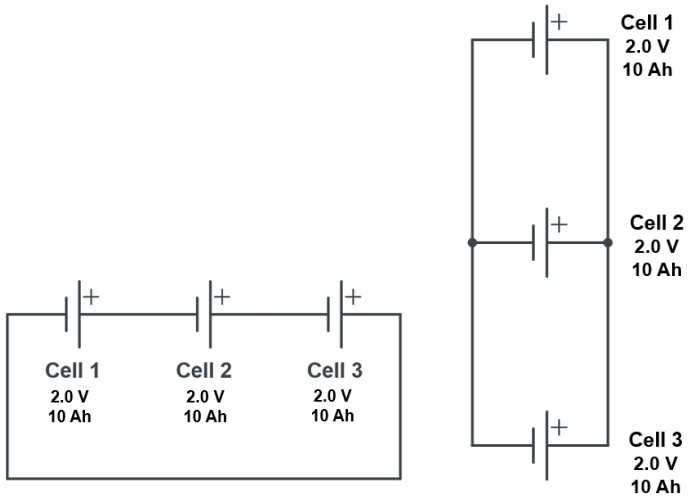

(a) (b)

Figure 6.6: 3-cell batteries connected in a) series, 6.0 V and 10 Ah, and b) parallel, 2.0 V and 30 Ah.

For the eVTOL flight shown in Figure 6.3, the number of cells required in series (N_S) for each segment can be determined using Eq. (6.18), where v_{cell} is known. Choose the largest of N_{S1}, N_{S2}, and N_{S3}, as that will cover all three segments. The number of cells required in parallel (N_P) can then be found using Eq. (6.19). The weight of each cell can then be found using Eq. (6.20), where W is the weight of the battery. Figure 6.7 shows an example of cells connected in series and parallel to power a load.

$$
\begin{aligned}
N_{S1} &= \frac{v_1}{v_{cell}(SOC_1)} \\
N_{S2} &= \frac{v_2}{v_{cell}(SOC_2)} \\
N_{S3} &= \frac{v_3}{v_{cell}(SOC_3)}
\end{aligned}
\tag{6.18}
$$

$$
\begin{aligned}
N_S N_P Q_{cell} &= Q_{total} \\
N_P &= \frac{Q_{total}}{N_S Q_{cell}}
\end{aligned}
\tag{6.19}
$$

$$
W_{cell} = \frac{W}{N_S N_P} \tag{6.20}
$$

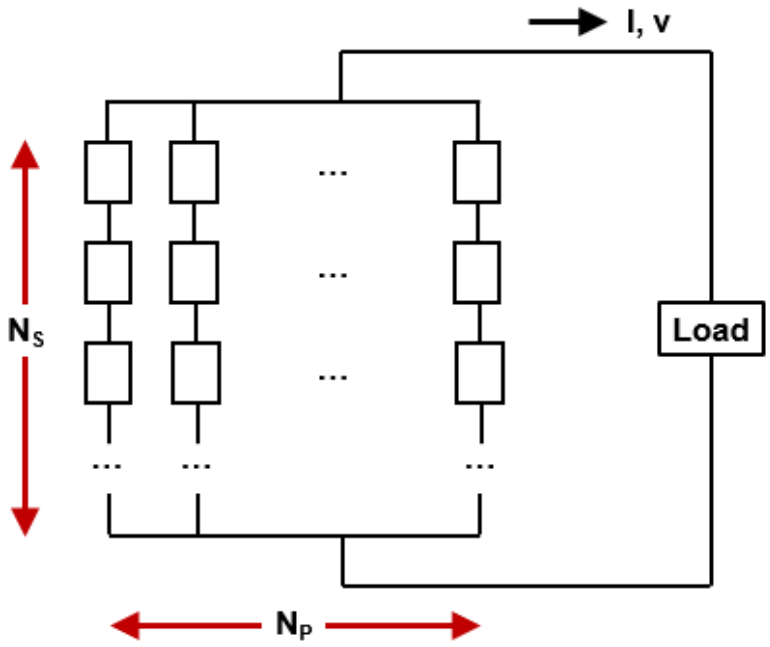

Figure 6.7: Example of number of cells in series and parallel, powering a load.

Consistency of charge and energy capacity:

Equation (6.13) can be rewritten in terms of specific charge capacity (SQ) as in Eq. (6.21). Dividing by the weight W gives a similar expression using the SOC as in Eq. (6.22). Starting at

the beginning of flight with $SOC = 1.0$, each segment changes the state of charge.

$$W = \frac{I_1 t_1}{SQ(C_1)} + \frac{I_2 t_2}{SQ(C_2)} + \frac{I_3 t_3}{SQ(C_3)} + \frac{Q_{extra}}{SQ(C_{1,2,\text{ or }3})} + \frac{\Delta Q}{SQ(C_3)} \tag{6.21}$$

$$\begin{aligned} 1 = & \frac{Q_1}{SQ(C_1)W} + \frac{Q_2}{SQ(C_2)W} + \frac{Q_3}{SQ(C_3)W} + \frac{Q_{extra}}{SQ(C_{1,2,\text{ or }3})W} + \frac{\Delta Q}{SQ(C_3)W} \\ 1 = & \quad SOC_1 \quad + \quad SOC_2 \quad + \quad SOC_3 \quad + \quad SOC_{extra} \quad + \quad \Delta SOC \end{aligned} \tag{6.22}$$

Similarly, it is possible to define the state of energy (SOE) as in Eq. (6.23). Starting at the beginning of flight with $SOE = 1.0$, each segment changes the state of energy. It follows that the loss of SOC and SOE for each segment are given by Eq. (6.24), where the subscript i denotes the segment and varies from 1 to number of segments.

$$\begin{aligned} 1 = & \frac{E_1}{SE(C_1)W} + \frac{E_2}{SE(C_2)W} + \frac{E_3}{SE(C_3)W} + \frac{E_{extra}}{SE(C_{1,2,\text{ or }3})W} + \frac{\Delta E}{SE(C_3)W} \\ 1 = & \quad SOE_1 \quad + \quad SOE_2 \quad + \quad SOE_3 \quad + \quad SOE_{extra} \quad + \quad \Delta SOE \end{aligned} \tag{6.23}$$

$$\begin{aligned} \text{loss of SOC} = & -\frac{I_i t_i}{SQ(C_i)W} \\ \text{loss of SOE} = & -\frac{I_i t_i v_i}{SE(C_i)W} \end{aligned} \tag{6.24}$$

Flight analysis:

During flight, no guaranteed design mission will be flown, and any current can be drawn. Starting from the start of flight where SOC $= 1$ and SOE $= 1$, the changes in SOC and SOE must be kept track of as in Eq. (6.25). However, the issue arises of how to determine the C-Rate at which to

find the specific charge capacity SQ and specific energy capacity SE. It is not simply as in Eq. (6.7), as Q_{total} is known only for the mission. For any other current, Q_{total} will change. Another data set is needed to carry out flight analysis.

$$\begin{aligned} dSOC &= -\frac{Idt}{SQ(C)W} \\ dSOE &= -\frac{Ivdt}{SE(C)W} \end{aligned} \tag{6.25}$$

The discharge data of voltage versus specific charge capacity can be seen in Figure 6.8. The various lines represent discharge at various currents, not related to the currents required by the mission. Based on the known discharge times, the C-Rates are also known. For any current drawn I, the specific current I/W can be found and the corresponding C-Rate determined using a trend as in Figure 6.9. The corresponding specific charge and energy capacities can then be found and the change in SOC and SOE can be calculated using Eq. (6.25).

Summary

To precisely size a battery for eVTOL, various data are needed. The aircraft design must supply the required power, current, and voltage over the time of flight. The battery data must include the cell voltage versus depth of discharge at various C-Rates, as well as the specific energy and charge capacity and specific current versus C-Rate.

To obtain this battery data, basic discharge data must be measured. The discharge curves of voltage versus time, charge capacity, energy capacity, and depth of discharge, all performed at various C-Rates, must be measured. These discharge curves were shown and discussed in detail in Chapter 4.

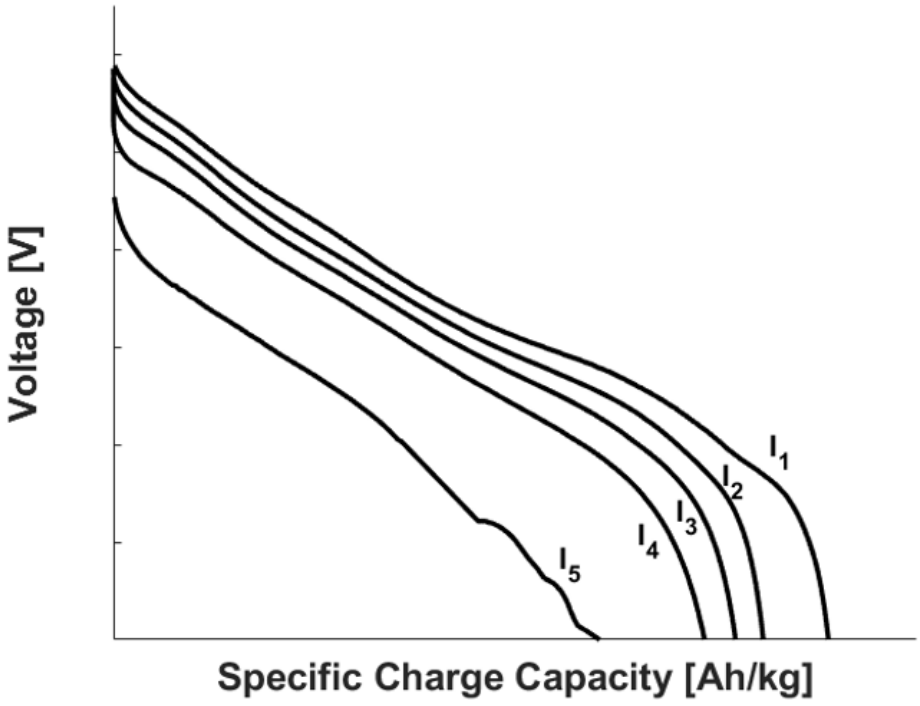

Figure 6.8: Voltage versus specific charge capacity for various currents.

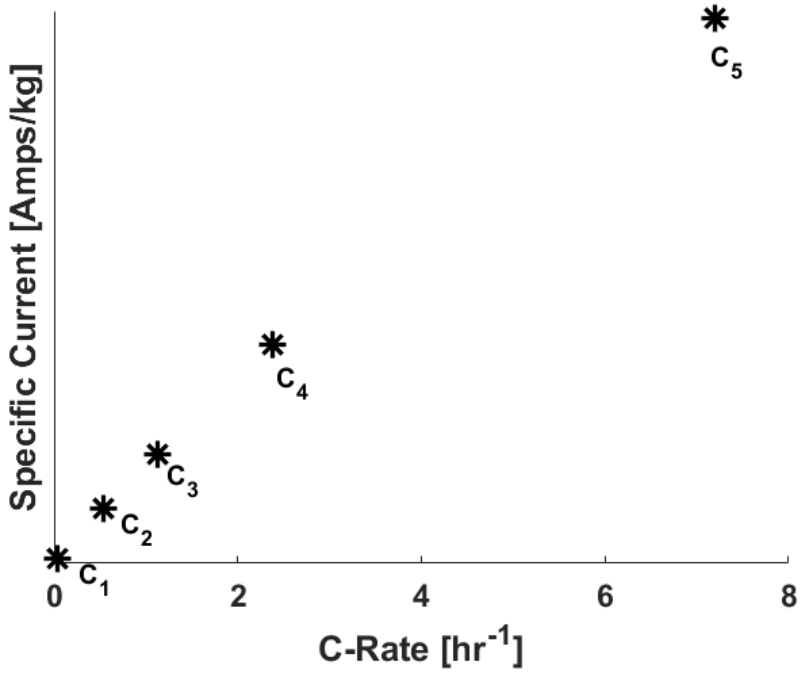

Figure 6.9: Specific current versus C-Rate for various currents.

6.4 Summary

The impact of capacity loss on aircraft range was discussed. The possibility of sharing power and energy responsibilities between Li-S and Li-ion batteries on an aircraft was investigated and sizing results for this scenario were shown. A conceptual battery pack was designed step by step.

1. Capacity decrease as cycle number increases has an impact on the range achievable by an eVTOL aircraft. A 50% decrease in capacity decreases the range by at least half.

2. eVTOL aircraft could use both Li-S and Li-ion batteries during flight, with the Li-S used for low power operations and Li-ion used for high power maneuvers. Sizing results for this scenario show a lower GTOW at 50 n-miles compared to the sizing results in Chapter 2.

3. To precisely size a battery for eVTOL, various data are needed. The aircraft design must supply the required power, current, and voltage over the time of flight. The battery data must include the cell voltage versus depth of discharge at various C-Rates, as well as the specific energy and charge capacity and specific current versus C-Rate. If an eVTOL aircraft is carrying two types of batteries, the sizing procedure does not change. Simply break up the mission and apply the method to each mission.

Chapter 7: Summary and Conclusions

This dissertation is an attempt to integrate electrochemistry and aeronautics, particularly rotary-wing aeronautics, where integration of power and platform is vital for the development of a viable aircraft. The principal barriers of electric-VTOL aircraft, energy and power, were addressed. The promising alternative of Li-S was investigated thoroughly in the context of eVTOL.

Findings presented in this dissertation showed that Li-S can be a promising and feasible alternative to Li-ion at a basic electrochemical level with the potential to double the range or payload of eVTOL aircraft. The realization of that potential will require careful scale-up with thermal, mechanical, and electrical considerations, and use in tandem with high C-Rate alternatives for hover and maneuvers.

A conceptual sizing method was developed and verified with results from researchers at NASA Ames. A mission was evaluated, with a range of 50 n-miles and payload of 2-3 people. Various battery specific energies were evaluated, and the results demonstrate the need for a high specific energy battery. Key battery performance targets for eVTOL were determined.

Li-S and Li-ion coin cells were fabricated with identical overhead, allowing for a clear and consistent comparison. The Li-S cells were free of the polysulfide shuttle effect, as the PANS cathode does not allow the formation of polysulfides. The Li-ion cells used a typical, modern

NCA cathode. Sulfur content in the Li-S cells was maximized as much as possible. Li-S and Li-ion theoretical charge capacities were calculated based on the cell designs.

Steady state testing and analysis was performed on the Li-S and Li-ion coin cells. Testing began with discharge of the cells at a very low current - a C-Rate of C/25. The data from the slow discharge allowed for a comparison of the measured charge capacity to the theoretical. The discharge characteristics were then collected for higher C-Rates, which allowed for the construction of a Ragone Plot of specific power versus specific energy. The cycle life of the Li-S and Li-ion cells was investigated, and the impact of half cycles on the cycle life was determined. Modeling of the steady state behavior was performed using the Shepherd model.

Transient data was collected for the Li-S and Li-ion cells. First, electrochemical impedance data was collected and analyzed. An ECM was developed based on the impedance data, and model parameters were extracted. The model was converted from the frequency domain to the time domain. Voltage responses of Li-S and Li-ion cells to step and pulse currents were collected, and the model in the time domain was applied to the data.

Finally, the impact of advanced batteries on eVTOL sizing was investigated. The impact of capacity loss on aircraft range was discussed. The possibility of sharing power and energy responsibilities between Li-S and Li-ion batteries on an aircraft was investigated. A conceptual battery pack was designed step by step.

Based on this work, the following key conclusions can be made, listed in order they were presented in the dissertation.

7.1 Key Conclusions

1. Sizing analysis found that there is a diminishing return when increasing the specific energy, as the increase from 150 Wh/kg to 300 Wh/kg causes dramatic improvements in all areas. However, increasing the specific energy further to 400 Wh/kg only slightly improves aircraft parameters.

2. Key battery performance targets were determined for eVTOL: a specific energy of 300 Wh/kg and a C-Rate of 1-2C.

3. Theoretical specific charge capacity of the Li-ion cells was calculated to be 141 Ah/kg and that of the Li-S cells to be 605 Ah/kg. The charge capacity was normalized by the weight of the electrodes, including the added carbon and binder. This is the proper normalization, as the cathodes must have the carbon and binder to operate.

4. Measured specific charge capacity of the Li-ion cells was 127 Ah/kg and remained steady with cycles. Li-S cells was 401 Ah/kg at a current of 1C. The measured charge capacity of the fabricated cells match well with the theoretical prediction.

5. The measured specific energy capacity of the Li-ion cells was 460 Wh/kg, and that of the Li-S cells was 533 Wh/kg at a current of 1C.

6. For C-Rates up to C/2, Li-S has twice the specific energy of Li-ion. Around 1C they crossover but thereafter Li-S drops rapidly. By 4C, the specific energy for LiS almost vanishes. These numbers upon scale-up have a dramatic impact on eVTOL and infrastructure. It favors a dramatic expansion of range of eVTOL over a reduction in gross weight.

7. The cycle life of Li-S is poor, but only when it is fully discharged. If only half cycles are allowed, the loss in capacity is almost eliminated. Operating at half cycles results in higher Li-S energy output compared to that of Li-ion, and more importantly stabilizes the Li-S cells where there is no decrease in specific energy capacity at least for the first 100 cycles.

8. Differences in behavior are explained by the internal nature of the cells. The Li-S cells exhibited an order of magnitude higher internal resistance. They also exhibited a marked Warburg-like behavior at the low frequencies of 1-100 Hz, a frequency range important in rotor response.

9. The dynamic behavior of the cells is characterized generally by a first-order lag in cell voltage in response to changing current. The nature of the lag is different between Li-ion and Li-S. The Li-ion is faster with a smaller time constant and is well represented by a resistor and a resistor-capacitor block. The Li-S is slower with a longer time constant and requires a non-ideal capacitor, i.e., a constant phase element, and for lower frequencies in the 1-100Hz range, the Warburg element.

10. eVTOL aircraft could use both Li-S and Li-ion batteries during flight, with the Li-S used for low power operations and Li-ion used for high power maneuvers. This would help minimize GTOW and optimize aircraft parameters.

11. To precisely size a battery for eVTOL, various data are needed. The aircraft design must supply the required power, current, and voltage over the time of flight. The battery data must include the cell voltage versus depth of discharge at various C-Rates, as well as the specific energy and charge capacity and specific current versus C-Rate. If an eVTOL

aircraft is carrying two types of batteries, the sizing procedure does not change.

7.2 Contributions

This work has three major contributions.

1. The developed sizing analysis established battery performance targets: a specific energy of 300 Wh/kg and a C-Rate of 2C. A diminishing return was observed when increasing the specific energy past 300 Wh/kg. These targets are essential to guide battery research specific to aviation.

2. A consistent comparison of Li-S and Li-ion cells with identical overhead. The Ragone plot showed the decrease of Li-S specific energy when discharging at C-Rates above 1C. An aircraft could carry both Li-S and Li-ion battery packs, and use Li-S at low power settings then switch to Li-ion when requiring high power, such as in hover or maneuvers.

3. Characterization showed feasibility of Li-S for eVTOL, especially when operating using half cycles. Half cycles stabilized the Li-S cells and no loss in energy was observed for at least 100 cycles. This stability gain would have a significant effect on eVTOL design, as missions can be controlled to operate at half cycles and the battery can recharge often.

7.3 Future Work

There are many factors that go into battery design for eVTOL. This work focused on fundamental understanding and characterization of state-of-the-art Li-S technology, but on a small scale. Based on the completed tasks in this dissertation, the following tasks are recommended

for future work.

1. The Li-S batteries discussed in this work must be scaled up. The small scale coin cells analyzed in this work have demonstrated the benefits on Li-S in the context of eVTOL. The process of scaling up the cells to larger, more powerful cells will bring to light any thermal, mechanical, or electrical issues in fabricating larger cells.

2. The larger, more powerful Li-S batteries must be integrated with an in-house 20 lbs aircraft for flight testing. Data collected from flight testing can validate the models of steady state and transient behavior shown in this dissertation. Flight test data can also validate the specific power and energy supplied during varying maneuvers.

3. Combination of Li-S and Li-ion should be explored where Li-S is used for cruise power and Li-ion for peak power boost in hover and maneuvers. There should be two packs, one for high energy and one for high power, connected in parallel.

4. The fundamental reasons for cycle life extension with half cycles should be explored in further depth. Scanning Electron Microscopy should be used to study the surface topology of the solid electrolyte interface. Energy Dispersive Spectroscopy should be used to study any evolution of chemical composition.

5. The fractional derivatives in the CPE and Warburg require very small time steps and information from all previous steps which is very intensive. A recursive formulation should be found instead which, even if approximate, would be more efficient and effective for real time SOC calculation.

6. The impact of temperature should be assessed between -40^{o}C to +40^{o}C and corresponding

models developed.

Bibliography

[1] Chretien, P. From Concept to Prototype in 180 Days. Vertiflite, April/May 2012.

[2] Treeck, H. Manned First Flight Writes Aviation History. https://www.volocopter.com/newsroom/manned-first-flight-writes-aviation-history/, October 2011.

[3] Ng, W and Datta, A. Hydrogen Fuel Cells and Batteries for Electric-Vertical Takeoff and Landing Aircraft. *Journal of Aircraft*, 56(5):1765–1782, 2019.

[4] Vertical Flight Society. VFS World eVTOL Directory. https://www.evtol.news/aircraft.

[5] Datta, A. and Johnson, W. Power Plant Design and Performance Analysis of a Manned All-Electric Helicopter. *Journal of Propulsion and Power*, 30(2):490–505, March 2014.

[6] Johnson. W, Silva. C, and Solis. E. Concept Vehicles for VTOL Air Taxi Operations. *Proceedings of the AHS Technical Conference on Aeromechanics Design for Transformative Vertical Flight*, January 2018.

[7] Hess, R and Stewart, J. and Britt, J. and Niedzwiecki, M. Use of a High Energy Dense Li Anode Cell for an eVTOL Application. In *Proceedings of the VFS Seventy-Sixth Annual Forum & Technology Display, Virtual*, October 2020.

[8] Johnson. W and Silva. C. Observations from Exploration of VTOL Urban Air Mobility Designs. *Proceedings of the 7th Asian/Australian Rotorcraft Forum, Korea*, October 2018.

[9] Bills, A and Sripad, S and Fredericks, W and Guttenberg, M and Charles, D and Frank, E and Viswanathan, V. Universal Battery Performance and Degradation Model for Electric Aircraft, July 2020.

[10] Yang X-G. and Liu T. and Ge S. and Rountree E. and Wang C-Y. Challenges and Key Requirements of Batteries for Electric Vertical Takeoff and Landing Aircraft. *Joule*, 5:1644–1659, 2021.

[11] Mizushima, K., Jones, P.C., Wiseman, P.J. and Goodenough, J.B. LixCoO2 (0¡x¡-1): A new cathode material for batteries of high energy density. *Materials Research Bulletin*, 5, June 1980.

[12] Muller-Warmuth, W and Schollhorn, R. *Physics and Chemistry of Materials with Low-Dimensional Structures*, chapter Progress in Intercalation Research. Springer, 1994.

[13] Reimers, J and Dahn, JR. Electrochemical and In Situ X-Ray Diffraction Studies of Lithium Intercalation in LixCoO2. *Journal of the Electrochemical Society*, 139(8), 1992.

[14] Shedd, K. US Geological Survey, Mineral Commodity Summaries: Cobalt, January 2021.

[15] MTI Corporation. Lithium Safety Data Sheet, March 2018.

[16] Sigma-Aldrich. Sulfur Safety Data Sheet, January 2021.

[17] Apodaca, L. US Geological Survey, Mineral Commodity Summaries: Sulfur, January 2021.

[18] Jaskula, B. US Geological Survey, Mineral Commodity Summaries: Lithium, January 2021.

[19] Barchasz. C., Molton. F., Duboc. C., Lepretre. J-C., Patoux. S, and Alloin. F. Lithium Sulfur Cell Discharge Mechanism: An Original Approach for Intermediate Species Identification. *Analytical Chemistry*, 84(9):3973–3980, April 2012.

[20] Manthiram. A, Fu. Y, Chung. S, Zu. C, and Su. Y. Rechargeable Lithium Sulfur Batteries. *Chemical Reviews*, 114(23):11751–11787, July 2014.

[21] Wang, J and Yang, J and Xie, J and Xu, N. A Novel Conductive Polymer-Sulfur Composite Cathode Material for Rechargeable Lithium Batteries. *Advanced Materials*, 14(13-14), July 2002.

[22] Wang, J and Yang, J and Wan, C and Du, K and Xie, J and Xu, N. Sulfur Composite Cathode Materials for Rechargeable Lithium Batteries. *Advanced Functional Materials*, 13(6), June 2003.

[23] Wei. S, Ma. L, Hendrickson. K, Tu. Z, and Archer. L. Metal-Sulfur Battery Cathodes Based on PAN-Sulfur Composites. *Journal of the American Chemical Society*, 137(37):12143–12152, September 2015.

[24] Danuta. H and Juliusz. U. Electric Dry Cells and Storage Batteries, 1962. Patent No. US3043896A.

[25] Rao. M.L.B. Organic Electrolyte Cells, 1966. Patent No. US3413154A.

[26] Nole, D and Moss, V. Battery Employing Lithium-Sulphur Electrodes with Non-Aqueous Electrolyte, 1968. Patent No. US3532543A.

[27] Linden, D. and McDonald, B. The Lithium-Sulfur Dioxide Primary Battery - its Characteristics, Performance and Applications. *Journal of Power Sources*, 5(1):35–55, 1980.

[28] Pitre, L J. Discharge Characteristics of Lithium/Sulfur Dioxide “a” Cells - Honeywell Inc., No. g-3029a3. Technical report, US Department of Energy, 1991.

[29] Levy, S. and Bro, .P. *Lithium/Sulfur Dioxide Batteries*, pages 233–247. Springer US, Boston, MA, 1994.

[30] Ratnakumar. B.V. and Smart. M.C. and Ewell. R.C. and Whitcanack. L. D. and Kindler. A. and Narayanan. S.R. and Surampudi. S. Potentiostatic Depassivation of Lithium-Sulfur Dioxide Batteries on Mars Exploration Rovers. *Journal of The Electrochemical Society*, 154(7):A715, 2007.

[31] Ma, Y and Zhang, H and Wu, B and Wang, M and Zhang, H. Lithium Sulfur Primary Battery with Super High Energy Density: Based on the Cauliflower-like Structured C/S Cathode. *Scientific Reports*, 5(14949), 2015.

[32] Fotouhi. A, Auger. D, O’Neill. L, Cleaver. T, and Walus. S. Lithium Sulfur Battery Technology Readiness and Applications: A Review. *Energies*, 10(12), 2017.

[33] Kumar, R., Liu, J., Hwang, J., and Sun, Y. Recent Research Trends in LiS Batteries. *Journal of Materials Chemistry A*, 6(25):11582–11605, 2018.

[34] Chen. L, and Shaw. L. Recent Advances in Lithium Sulfur Batteries. *Journal of Power Sources*, 267:770–783, December 2014.

[35] Shim, J and Striebel, K and Cairns, E. The Lithium/Sulfur Rechargeable Cell : Effects of Electrode Composition and Solvent on Cell Performance. *Journal of the Electrochemical Society*, 149(A1321), August 2002.

[36] Mikhaylik, Y and Akridge, J. Polysulfide Shuttle Study in the Li/S Battery System. *Journal of the Electrochemical Society*, 151(A1969), October 2004.

[37] Yu. X and Xie. J and Li. Y and Huang. H and Lai. C and Wang. K. Stable-Cycle and High-Capacity Conductive Sulfur-Containing Cathode Materials for Rechargeable Lithium Batteries. *Journal of Power Sources*, 146(1):335–339, 2005.

[38] Pu. W., He. X., Wang. L. Sulfur Composite Cathode Materials: Comparative Characterization of Polyacrylonitrile Precursor. *Ionics*, 13:273–276, 2007.

[39] He. X., Ren. J., Wang. L. Electrochemical Characteristics of Sulfur Composite Cathode for Reversible Lithium Storage. *Ionics*, 15:477–481, 2009.

[40] Scheers. J, Fantini. S and Johansson. P. A Review of Electrolytes for Lithium Sulphur Batteries. *Journal of Power Sources*, 255:204–218, June 2014.

[41] Mikhaylik, Y. Electrolytes for Lithium Sulfur Ccells., 2008. Patent No. US7354680B2.

[42] Harris, F. D. *Introduction to Autogyros, Helicopters, and Other V/STOL Aircraft, Volume II: Helicopters*. NASA Ames Research Center, 2012. NASA/SP-2012-215959.

[43] W. Johnson. Nasa design and analysis of rotorcraft. *Technical Report 2009-215402, NASA*, December 2009.

[44] Shepherd, C.M. Design of Primary and Secondary Cells ii. An Equation Describing Battery Discharge. *Journal of The Electrochemical Society*, 112:657–664, July 1965.

[45] Nobel Prize Outreach AB. Otto Warburg – Biographical. `https://www.nobelprize.org/prizes/medicine/1931/warburg/biographical`, 2022.

[46] Miller, K. S. and Ross, B. *An Introduction to the Fractional Calculus and Fractional Differential Equations*. John Wiley & Sons, Inc., 1993.

[47] Oldham, K. B. and Spanier, J. *The Fractional Calculus*. Academic Press, Inc., 1974. See republished edition by Dover Publications, Inc., Mineola, New York, 2006.

[48] Locorondo. E, Pugi. L, Berzi. L, Scavuzzo. S, Ferraris. A, Airale. A G, Carello. M. Modeling and Simulation of Constant Phase Element for Battery Electrochemical Impedance Spectroscopy. *IEEE 5th International Forum on Research and Technology for Society and Industry, Florence, Italy*, September 2019.